Multiple Beams Interferometry for Array Illuminator and its Applications

by
Ardhendu Sekhar Patra

Department of Physics
Indian Institute of Technology Guwahati,
Guwahati – 781039, India.
June, 2005.

Multiple Beams Interferometry for Array Illuminator and its Applications

A Thesis Submitted

in Partial Fulfillment of the Requirements

for the Award of the Degree of

DOCTOR OF PHILOSOPHY

by

Ardhendu Sekhar Patra

To the

Department of Physics

Indian Institute of Technology Guwahati,

Guwahati – 781039, India.

June, 2005.

Dedicated to My Uncle

Acknowledgement

Firstly, I would like to express my sincere gratitude to my thesis supervisor Dr. Alika Khare for her invaluable guidance, support, and suggestions. The thesis work has been a very good learning experience for me, and the credit for this definitely goes to Dr. Khare. Without her guidance, my thesis would not have taken its present shape.

I am grateful to Prof. Prabin Bora, Dr. C.Y. Kadolkar, Dr. Pratima Agarwal and Dr. P. Senthilkumaran for their critical suggestions.

I would like to thank Mr. Sidananda Sarma, Mr. Chandan Borgohain, Mr. Lokesh Chakraborty, Mr. Atul Deka, Mr. Madan Deka, for their invaluable assistance during the course of the Ph.D. work.

I am thankful to Department of Mechanical Engineering, IIT Guwahati for providing micrograph facility and to all the members of mechanical workshop for their help during designing and fabrication of components for experimental setup.

I would like to pay my special thanks to Mr. Kamlesh M. Alti, Mr. Susanta Das, Miss Monisha Sharma, Miss Tina D. Phukan, Mr. Vinod P., Mr. Purnananda Nandi, Mr. Gautam Sharma, Mr. Santanu Sinha, Dr. Akhyaya Pattanaik, Dr. Manoranjan Kar and Dr. Abhijit Borah, for their help and making my stay enjoyable at IIT.

My special thanks are to Dhruba Saikia and his mother for providing me a homely atmosphere during my stay at IIT.

I would also like to acknowledge all my friends and well wishers, who have given me encouragement and helpful criticisms.

Last, but not least of all, I am indebted to my parents, uncle, sister, nephew and brother-in-law for all their love and affection without which I may not have reached this stage.

Abstract

The present work is aimed towards generation and characterization of the arrays using various interferometric configurations. Heterodyne interferometric configurations using polarized lights was developed and studied. The expressions for the intensity distribution for the all configurations presented in the thesis were worked out and compared with the experimental observations. The applications of these optical arrays as a single step microlithography technique was proposed and demonstrated. Line integrated electron density in a pulsed spark gap was recorded using interferometric setup.

Two interferometers in tandem were assembled for the generation of square and rectangular arrays of tiny light spots. The hexagonal arrays were produced using interference of eight beams. Eight coherent beams were generated using one Mach-Zehnder and two Michelson interferometers in tandem. The beating phenomenon was observed due to little mismatch in spatial frequencies of the individual interferograms in eight-beam interference pattern. The geometry and size of these arrays can be controlled by the mirror's tilts online. The array patterns and beating phenomenon were recorded onto CCD and analyzed. The array patterns were compressed with the help of a lens and maximum spot density around 1000 spots/mm^2 was recorded.

To improve upon the light efficiency of above system, we have proposed and developed the heterodyne interferometers for two and four beams using polarized light. The Experimental setups are similar to Michelson interferometers in tandem using polarizing components. The output of such interferometers results into orthogonally polarized multiple beams. The interference patterns of these beams are non-observable.

The fringes were recorded with the help of a quarter wave plate and a polarizer. The fringe patterns were studied as a function of azimuth of polarizing components.

The interference patterns from all the interferometric configurations were observed to be highly delocalized along the longitudinal direction of beams.

A new single shot lithography technique using multiple beam interferometers was developed. Using this technique the periodic structures down to periodicity ~1 micron were obtained in a single step without using any mask. With the two beams, large number of parallel thin lines and with the four beams, large number of holes in the square matrix format were imprinted on the Indium thin film.

Line integrated electron density profile of pulsed plasma was measured using two beam interferometric setup, illuminated by randomly polarized He-Ne laser.

Contents

List of Figures

Chapter 1

Introduction

The array illuminator (AIL) is an important optical circuit capable of converting a uniform beam of light into a one dimensional or two dimensional arrays of equal intensity tiny light spots. These array illuminators have a widespread application in optical logic gates or bistable elements[1], data storage[2,3], digital parallel processing[4], optical computing[5-11], optical interconnections[12-14], optical switching[15-17], image processing[18], optical signal processing[19], pattern recognition[20], fiber couplers[21], photonic delayline[22], holographic data storage[23], atom lithography[24,25], fabrication of two dimensional photonic crystals[26] and online optical testing[27, 28], etc.

System architectures and design techniques for digital optical circuits for optical system and for optical logic gates was reported by N. Streibl and M.E.Prise[1]. A random access optical memory (optical data storage) with storage capacity of $6.5X10^7$ bits for write-read-write operation was proposed by B. Hill[2] et. al. They have used 8X8 arrays generated by splitting the single beam with the help of three calcite prisms. Don A Gregory and H. K. Liu[3] have presented the analysis and experimental results of a large memory real-time multichannel multiplexed pattern recognition system using 5X5 arrays generated by holographic lens. The bistable optical logic gate array which can be generated from lenslet arrays or interferometers, can be applied to the all-optical digital parallel processing[4]. With the development of arrays of all-optical binary logic gates, it

is possible to combine the advantages of optical communication with that of the accuracy of digital techniques, resulting in the creation of ultra-powerful computation devices. Such optical logic arrays have been used in digital optical computing[5] with symbolic substitution. Brenner[6] presented a programmable optical processor based on symbolic substitution logic. Yatagai[7] proposed two optical implementations of cellular logic computers, in which the functions are programmable. By using optical techniques of parallel logic, interconnections and feedback, an optical Minnick's cellular logic is implemented in which cellular logic was performed using a matched filter array[7] with the help of multiple imaging and microlens array. The general characteristics and advantages of 2-D optical cellular processors have been discussed by J. Taboury et al[8]. A space invariant optical logic-gate array based on encoding and superposition of a decoding mask with the coded input patterns was proposed by T. Yatagai[9]. Murdocca[10] et al. presented a technique for designing digital logic circuits for regularly interconnected arrays of optical logic gates. One dimensional and two dimensional binary logic operation was suggested by O. Guyot and H. Hamam[11] using fractional Talbot effect. Urquhart[12] et al. have used two dimensional diffractive arrays for free space optical interconnections. Free space optical interconnection technology can be applied to neural network[13]. Integrated-optic array illuminator for guided wave optical interconnections was reported by T.D.Liao and Stephen Sheard[14]. Optical interconnections, generally binary phase grating, having 64X32 array of spots, were used for free space optical switching network[15-16] and crossbar switches[17]. An optical parallel architecture was suggested and verified experimentally to implement a basic programmable cellular logic array[18] for image processing. Agu et al. reported a parallel processing optical-digital recognition system[20]. Mortimore and Arkwright[21] proposed

monolithic wavelength flattened 1X7 single-mode fused fiber couplers. A 7-bit multichannel photonic delayline for phased-array antenna control is demonstrated[22]. Yang and Wang[23] proposed focal depth enhanced phase mask for the improvement of holographic data storage. The fabrication of one and two-dimensional nano structures was discussed by V. Sandoghdar[24] et al. using nano-lens arrays. A two dimensional photonic crystal was fabricated by electrodeposition and interference lithography[26]. The Talbot array illuminators were used to measure the thresholds of thin film coatings[27] and temperature in axisymmetric gaseous flames[28]. There are many more applications of various array illuminators in different fields.

1.1. Review of array illuminators

Wide spectrum applications in modern optical technologies have been demanding the array illuminators with specific configurations. For example, hexagonal geometries required in cellular logic[7, 18] and photonic band gap materials[26], where as the square and rectangular geometry is preferred in optical computers[6,8] and data storage devices[2]. The arrays of equal illuminating light spots can be generated by various schemes. Every illuminator has its own advantages and disadvantages over each other, and a proper choice depends on the user's requirements. The optical array illuminator can be divided into three basic techniques; i.e, diffraction[29-65] , interference[76-86] and waveguide[87-89].

1.1.1. Diffraction techniques

The diffraction techniques for array illuminator are very well documented in literature. In diffraction technique, the array illuminators are usually realized by specially designed arrays of pinholes[49], lenslets[29], phase contrast grating[32], grating couplers[78], point holograms[52], Talbot effect[39-40], Dammann grating[58-63], etc.

a. Image plane array illuminators

Image plane array illuminators are realized by placing special components in an image plane as shown in Fig.1.1.

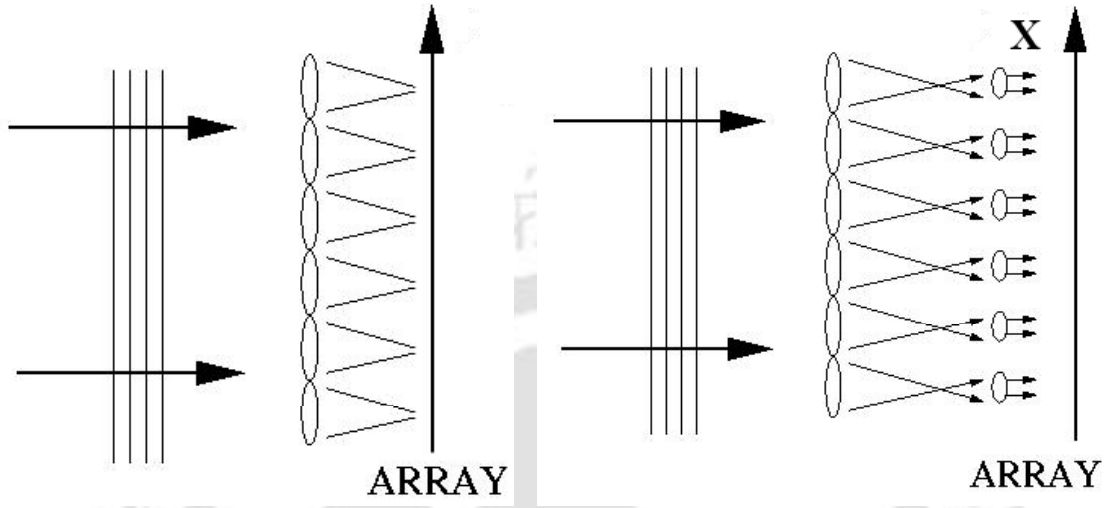

(a) (b)

Fig.1.1. Image plane array generators (a) lenslet array (b) telescope array.

In its simplest form, an expanded beam falls onto a lenslet array[29] of Fresnel zone plate or holographic lenses[30] such that different parts of the input beam focus directly onto different devices as shown in fig.1.1a. Large no. of arrays of microlenses required for the image plane illuminator can be fabricated by photolytic technique[34], monolithic[35] or thin film deposition[36] technique. In order to reduce the cross talks between the light channels of arrays (because of diffraction at the edges of lenslet) and to scale the size and spacing between the channels independently, telescopic arrays were proposed. The Kepler and Galilean type telescopic arrays as shown in fig.1.1b consist of pair of lenslet arrays with coincident focal point[30]. The compression ratio of these telescopic arrays depends on the ratio of focal lengths of two lenses. Telescopic arrays may be fabricated as ordinary (refractive) optical elements or as holographic (diffractive) optical

elements. Holographic telescope arrays are useful tools for illuminating arrays of small optical or electrooptical components.

Array illuminator based on phase contrast[31-33] is another way of image plane array illuminators. The object consists of a two-step phase grating which is illuminated with a plane wavefront as shown in fig.1.2. The phase contrast platelet at the center of the filter plane (FILT) shifts the phase of the zero-zero diffraction order. The spot array is produced in the form of phase mask first. By a phase contrast imaging step, this is converted into an intensity distribution of spots. The optical properties of sampling filter was described by Kolodziejczyk[37].

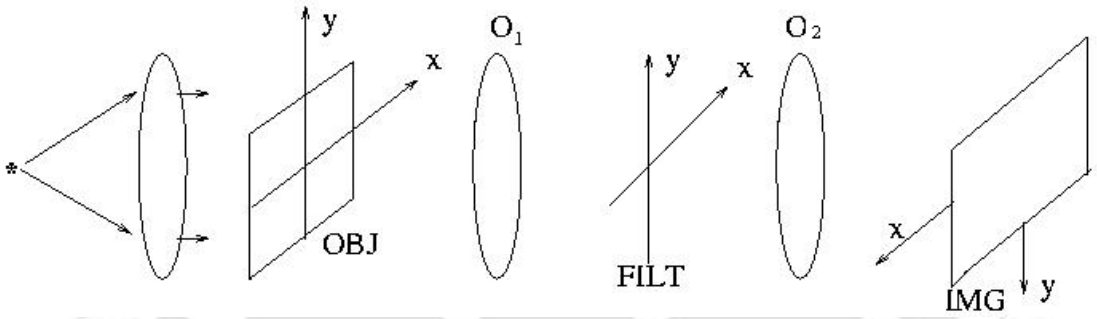

Fig.1.2. Scheme of phase contrast array illuminator

b. Talbot array illuminator

Talbot effect is a very well known and has a long history and numerous applications. It is also well known that at the fractional Talbot distances, there are interesting grating imaging phenomenon. Lohmann[38] was the first to make array illuminator using pure phase distribution at the fractional Talbot distance. These phenomenons are based on Fresnel diffraction on a phase grating as shown in fig.1.3. There have been few reports[39-41] for the general mapping in the image plane (for array illuminator) using optical transformation for Fresnel diffractions. These array illuminators can also be called as Fresnel plane array illuminator. When a grating at Z = 0 in fig.1.3 is

illuminated by a plane wave, the amplitude immediately behind the grating will depend upon the shape of the grooves of the grating.

.

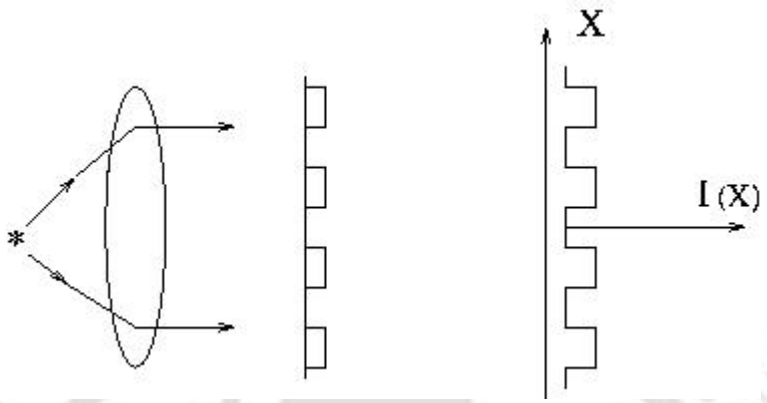

Fig.1.3. Fresnel diffraction on phase grating

In general, under coherent plane wave illumination, the normal Talbot effect[42] yields exact copies of the periodic input pattern in the planes $Z = N.Z_T$, where N is an integer and Z_T is called as Talbot length given by $Z_T = 2d^2/\lambda$, d = grating period, λ = wavelength of the incident wave.

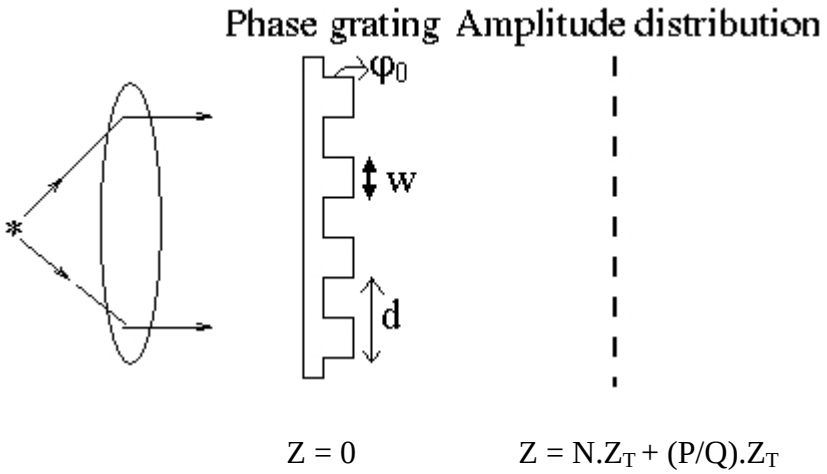

Fig.1.4. General principle of Talbot AIL.

Using a phase diagram approach A.W. Lohmann[43] described two configurations of binary phase grating which produced high contrast images at the fractional Talbot distances $Z = N.Z_T + (P/Q).Z_T$ (where P< Q, P & Q are positive integers). These two configurations are (i) a Ronchi ruled grating w/d = ½ with phase step $\varphi_0 = \pi/2$ as shown in fig.1.4 and primary imaging distance $Z = (¼)\ Z_T$ (ii) a Ronchi ruled grating w/d = 1/3 with phase step $\varphi_0 = 2\pi/3$ and primary imaging distance $Z = (1/3)\ Z_T$. There have been few more experimental reports[44-51] on the formation of AIL based on fractional Talbot effect using binary phase grating of variable fill factors. Hamam[52] proposed a general analytical form for conventional Talbot AIL for every fractional Talbot AIL in both one dimensional and two dimensional cases. He also proposed useful techniques[53, 54] to design Talbot AIL's.

c. Fourier Plane array illuminators

Fourier plane array illuminators are based on Fraunhofer diffraction or Fourier transformation of special components. Fig.1.5 shows the basic principle of Fourier plane array illuminators. These AIL's have been used widely in the context of multiple imaging[55-63]. There are several methods to make multiple images using array of pinhole lenses, an array of lenses, a hologram of an array of pinholes, various types of simple phase gratings, lensless Fourier holograms, diffraction technique, spatial frequency sampling, and phase gratings, etc. Dammann[68] described a method, combining the Fourier holography and grating methods to form a large number of images in one imaging step. Dammann et al.[69] put forward the original binary phase (0,π) grating structure for multiple image copying in parallel, in which both the magnitude and the phase of the spot array in Fourier transforming plane are specified. An improved

Dammann grating structure in which only the intensities of the spot array are specified, have been developed by Killat[70] et al.

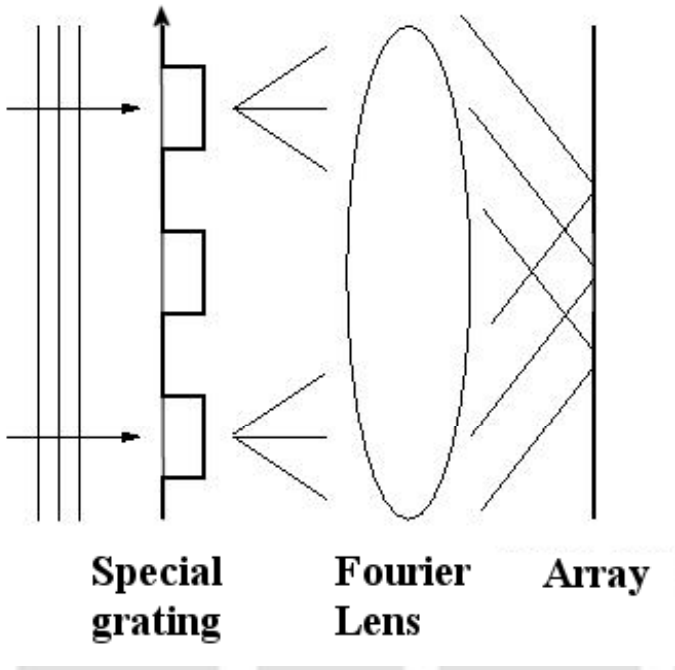

Fig.1.5. Basic principle of Fourier plane array illuminators

Krackhardt and Streibl[71] have given the outline of the design procedure for Dammann gratings. They have also given a comparison of different designs in terms of their relevant parameters such as the efficiency, the feature size and the error sensitivity. Mait[72] has experimentally shown that it is possible to design and fabricate phase gratings for two-dimensional nonseparable, noncentrosymmetric responses. Stripe geometry for two-dimensional Dammann grating have been proposed by J. Turunen et al.[73] to generate 2D pattern of discrete light spots with low reconstruction error and high diffraction efficiency. The holographic gratings were optimized to feature a negligible reconstruction error and these could be fabricated easily using common

microlithographic techniques. Dammann grating was modified to a four level phase representation to increase the diffraction efficiency[74]. In the designing of grating, symmetries[75] play a key role to reduce the design complexity. A translational symmetry leads to the highly desired result of even-numbered spot arrays.

1.1.2. Interference Techniques

There have been reports[76-86] on generation of AIL using interferometric techniques. Unlike diffraction technique, the interference techniques are relatively simple and do not require elaborate designing of the appropriate optical components.

a. Wedge plate interferometer

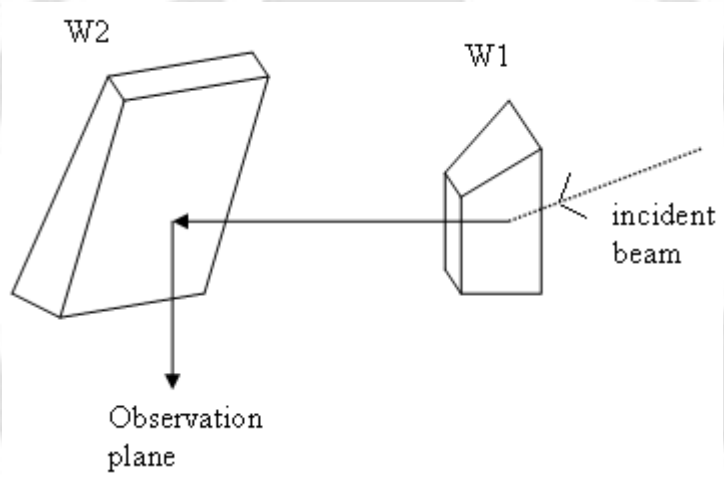

Fig.1.6. Experimental setup for array generation using wedge plate interferometer

An interferometric method for the generation of square and rectangular arrays with a combination of the two wedge plate orientations that yields an array of equal intensity light spots was reported by P. Senthilkumaran et. al[76]. The combination of wedge plates is shown in fig.1.6. The incident wavefront splits into four wavefronts at the observation plane due to the reflections from the front and back surfaces of both the wedge plates W1 and W2. The spatial frequency of the arrays can be controlled in real time by adjusting the orientations of the plates. The only limitation of the setup is poor light efficiency.

b. Interferometers in tandem

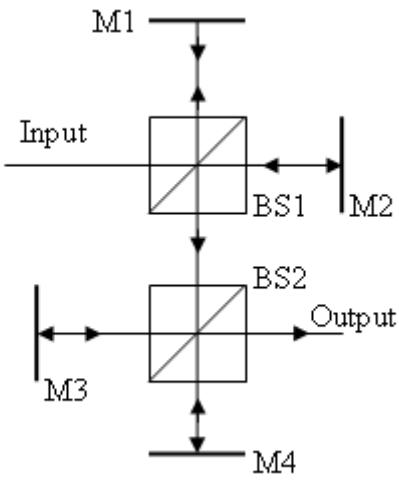

Fig.1.7. Experimental setup for array generation using Michelson interferometers in tandem

Two Michelson interferometers in tandem for the generation of square and rectangular arrays were reported by P. Senthilkumaran and R.S.Sirohi[77]. The schematic of the experimental setup is shown in fig 1.7. A collimated beam is launched into first Michelson interferometer followed by another Michelson interferometer. There are four interfering beams at the output plane. By adjusting the tilts of the mirrors the arrays can be generated with desired spatial frequencies. Shanti Bhattacharya et al.[78] and Darlin et al.[79] have reported holographic recording of the above arrays as a phase hologram which also serves as an array generator. This configuration utilizes five beams. One reference beam is derived by placing an additional beam splitter before launching the input beam to interferometer and other four beams were taken from the output of 2nd stage of Michelson interferometer. A hologram (phase element) is recorded by these cross patterns on the holographic films. The zeroth order reconstruction of the array pattern is obtained by illuminating this phase element with collimated beams at normal

incidences. An interferometric setup with polarizing elements was also theoretically proposed by P. Senthilkumaran[80] to increase the efficiency of the arrays.

c. Three waves interference

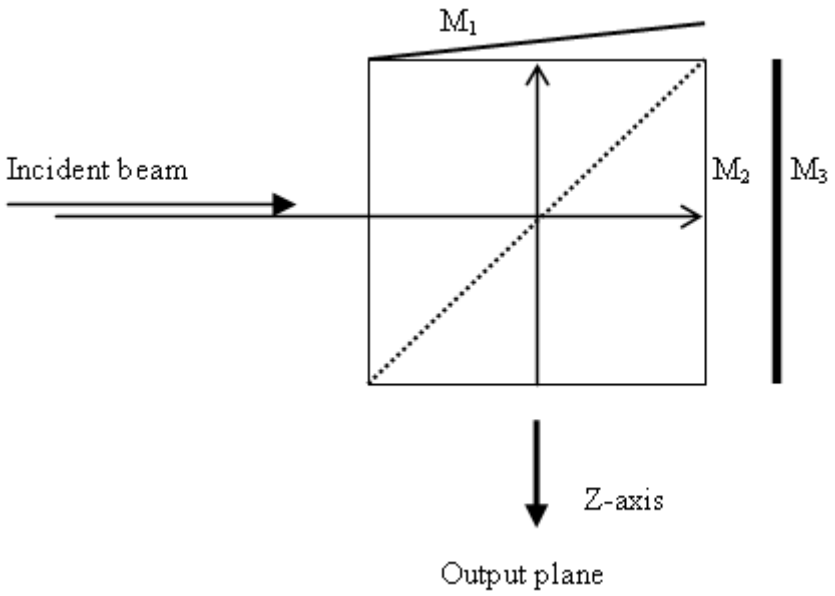

Fig.1.8. Experimental setup for array generation by three wave lateral shearing interferometer

The hexagonal array patterns can be generated with the interference of three beams. A prototype three-wave lateral-shearing interferometer was described by J. Primot[81, 82]. The schematic of the experimental arrangement used by them for the production of arrays in hexagonal geometry is shown in fig.1.8. It consists of a specially designed cube beam splitter with partially reflecting surface at two adjacent sides M_1 and M_2 as shown in the figure. This generates the two beams at the output plane. The third beam is generated by reflection from the mirror M_3. The three beams on recombining in the output results in the hexagonal geometry. The only limitation of this setup is that there is not much online control onto the spatial frequency. Three plane waves interference was studied theoretically as well as experimentally by J. Masajada[83]. An holographic

approach for 2-D arrays using additive source interference from multiple slab reflections was proposed by J. Canning[84]. Interference of three noncoplanar beams were analyzed theoretically by L.Z.Cai et al[85, 86]. The schematic of interference of three noncoplanar beams at mutual 120° angles is shown in fig.1.9. The two mirrors M_1 and M_2 are placed at 60°. The input beam1, the beam 2 reflected by M_1 and beam 3 reflected by M_2 results into the interference pattern in localized hexagonal arrays. Sandoghdar et al.[24] have used this configuration for producing the arrays of light beam in hexagonal geometry for the atom lithography via dipole force.

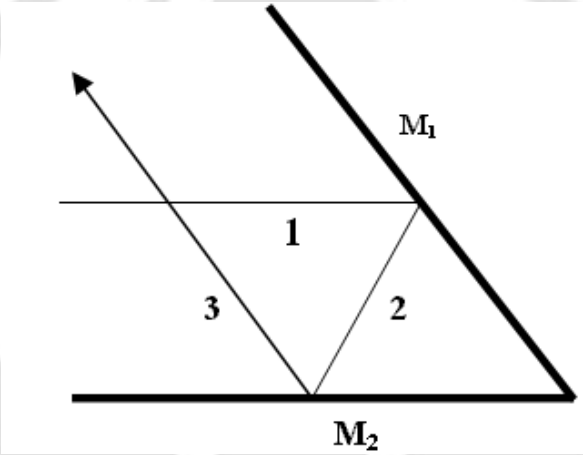

Fig.1.9. Experimental setup for array generation by three waves 120^0 each other

1.1.3. Waveguide Techniques

Waveguide techniques are upcoming techniques for the generation of equal illumination light arrays in various configurations.

a. Fiber grating

Fiber grating is used as diffractive element for the generation of large no. of equal illuminating light spots[87]. Fiber grating consists of large no. of optical fibers arrayed in the form of a monolayer sheet. The cladless type fibers of appropriate lengths were arrayed on a plastic holder. When a coherent plane wave is projected perpendicularly on such fiber sheet, each fiber acts as a cylindrical lens and focuses the incident wave

just behind the grating. Each focal point emits coherent cylindrical waves over a wide angle of uniform intensity. A 2-D array of diffraction spots can be obtained with two fiber gratings placed perpendicular onto each other as shown in fig.1.10. A sphere like lens is formed at the intersections of two fiber grating. Just behind the fiber grating a pinhole matrix is formed and the fourier transform array is a 2-D spot array. The use of fiber grating for the production of AIL and multiple imaging were proposed by H. Machida[87] et.al.

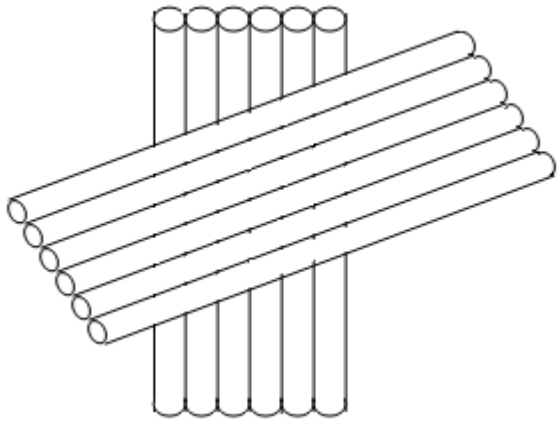

Fig.1.10. Crossed fiber grating to produce a 2-D spot array.

b. Grating Couplers

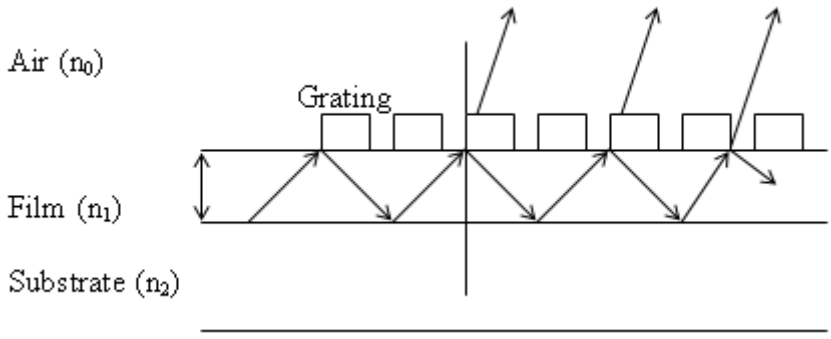

Fig.1.11. Geometrical configuration of grating coupler

A grating coupler is a compact device for the generation of arrays. A film of refractive index n_1 is sandwiched between air and a substrate of low refractive index n_2 ($n_1 > n_2$)

as shown in fig.1.11. A phase grating is fabricated on the top surface of the film, so that the evanescent waves are coupled with this grating. Takeda et.al[88] has reported such two-dimensional array illuminator. There is no online control on the array geometry in grating coupler. But it is well suited for the integrated optics.

c. Graded index rods

The graded index rods can be arranged like arrays in 2-D[89] and retroreflection from these arrays of rod results into the equal illuminating light spots in the form of array.

1.2. Summary of work

The diffraction based techniques to generate the arrays of tiny light spots are very well documented in the literature. In these techniques the special diffractive apertures are to be designed for specific configuration of arrays of equal illuminating spots. Moreover, the array pattern is localized in the longitudinal direction for most of the cases. The interference techniques for the generation of arrays are normally less complicated and conceptually simple. The arrays can be generated with the commercially available beam splitters and mirrors. In most of the interferometric configurations, array patterns are highly delocalized in the longitudinal direction and hence the compression ratio can be varied with a lens. However interference techniques are not reported well. Therefore, present work is aimed towards generation of arrays of tiny light spots using interference of multiple beams and their characterizations and applications towards the single shot lithography.

In chapter 2, various interferometric configurations developed in the present work for the generation of square, rectangular and hexagonal arrays are described. The experimental setup developed using randomly polarized as well as polarized beams are discussed. The selective ablation setup designed for the single shot writing of large no.

of array is also discussed. The measurement of electron density profile in a spark plasma using interferometric techniques is also included as another application of interference phenomenon.

In chapter 3, the expressions for the electric fields of multiple interfering beams in terms of spatial frequency (and hence angular separation) are worked out for all the configuration developed in the present work. The resultant intensity distributions in the output plane for the polarized as well as randomly polarized setup described in chapter 2 are derived. The expression for electron density is deduced in terms of fringe shift for the measurement of space resolved electron density profile in the spark plasma.

In chapter 4, the results of square, rectangular and hexagonal arrays generated by four beam and eight beam interferometric setups in the present work are presented using randomly polarized lights. The detail analysis in terms of intensity distribution, fringe visibility, compression factor and delocalization of the array patterns are discussed. The experimental results are compared with the computed results.

In chapter 5, the arrays generated in the square geometry using polarized beams are described with the detailed studies on fringe shift and fringe visibility as a function of orientations of the polarized components. Computed results are compared with the experimental observations.

In chapter 6, the applications of arrays of equal illuminating tiny spots are discussed. The results of single shot lithography technique developed for writing the large no. of lines and spots in micron and sub-micron range using high power laser interferometers is presented. The measurement of electron density profile in a spark gap using interferometric technique is also presented. Some of the possible applications of

the interferometric arrays for the polarization of photonic band gap materials, periodic microstructures and atom lithography are also proposed.

Chapter 7 summarizing the results of present work.

Chapter 2

Experimental Setup

Various experimental schemes for the generation of arrays of tiny light spots have been described in chapter 1. We have developed various interferometric configurations for array illuminator having square, rectangular and hexagonal geometry. The multiple beam interferometers were developed using randomly polarized as well as polarized light. The interferometric setups have advantages of having online control on the geometry of the arrays and array patterns being delocalized over large longitudinal distances compared to the other techniques.

2.1. Generation of Collimated Beam

One of the basic requirements for the interferometer is the highly collimated beam. Setup used for the collimation of the beam is shown in fig.2.1.

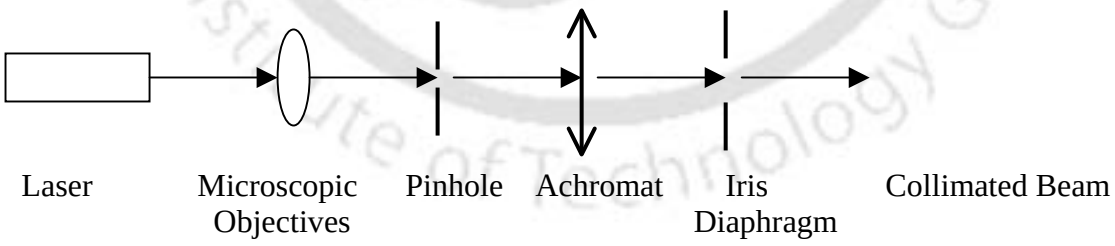

Fig.2.1. Beam collimation setup

A 30mW He-Ne laser (05-LHP-827, Melles Griot) was launched into a microscopic objective (Oriel) of focal length 0.17mm. A pinhole of 25 μm was placed on the focus of the objective to cut down the spatial frequencies. The beam was collimated with the help of an achromat of focal length 25 cm. An iris diaphragm was placed in the path of

the collimated beam to take only the central maxima of the diffraction pattern of the pinhole. The beam collimation was tested with the collimation tester (model no 09SPM001, Melles Griot). This beam was used to illuminate all the interferometric configurations developed with He-Ne laser for randomly polarized light. For the polarized setup 30mW He-Ne laser was replaced by 10mW laser. The beam was recorded directly onto CCD (PCO- Pixelfly-imaging-SVGA) and the intensity profile was scanned and fitted to Gaussian distribution as shown in fig.2.2. Though the experimental plot shows the nearly flat-top profile compared to Gaussian distribution but for the simplicity, this Gaussian fit was incorporated in all the calculations described in chapter 3.

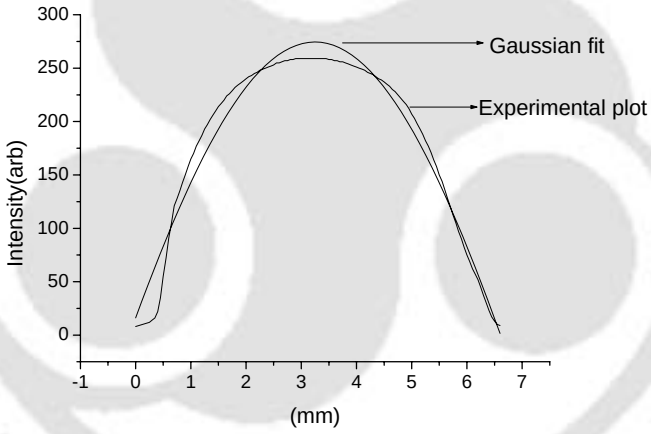

Fig.2.2. Intensity profile of the beam

2.2. Randomly Polarized Interferometric Setup

2.2.1. Four Beams Interferometric Setup

The collimated beam from the setup of fig.2.1 was launched in a Mach Zehnder interferometer (first stage) comprising of two cube beam-splitters (BS1 & BS2, Melles Griot - 03BSC015) and two mirrors (M1 &M2, Newport - 10D10ER.1). Mirror M1 was adjusted for 45°. Mirror M2 was tilted in such a way that output of the first stage

coming out from BS2, resulted into straight horizontal fringes. One set of the output beams from first stage entered into a Michelson interferometer (second stage) consisting of cube beam splitter BS3 and mirrors M3 and M4. BS3 splits each beam into two parts. So in the output plane from BS3 four beams came out. Orientation of the fringes for the second interferometer with respect to that of first interferogram is adjusted by tilting mirror M4 w.r.t. M3 (kept for normal incidence). Mirror M4 was given a tilt to form the straight vertical fringes which were perpendicular to the fringes of first interferograms. The square and rectangular arrays were produced by adjusting the tilt of mirrors M2 and M4 and hence the angular separations of the beams. The resultant interference pattern was imaged directly onto CCD. Michelson interferometer can also be used in the first stage of fig.2.3 in place of Mach Zehnder interferometer. But we have observed that Mach Zehnder interferometer has the advantage of less multiple reflections compare to the Michelson geometry and hence the contrast of the array patterns is better. However if the anti-reflected coated beam splitters are used then the performance with both the configurations will be same. In most of the experiments unless other wise mentioned we have used the beam splitters without having anti reflection coating.

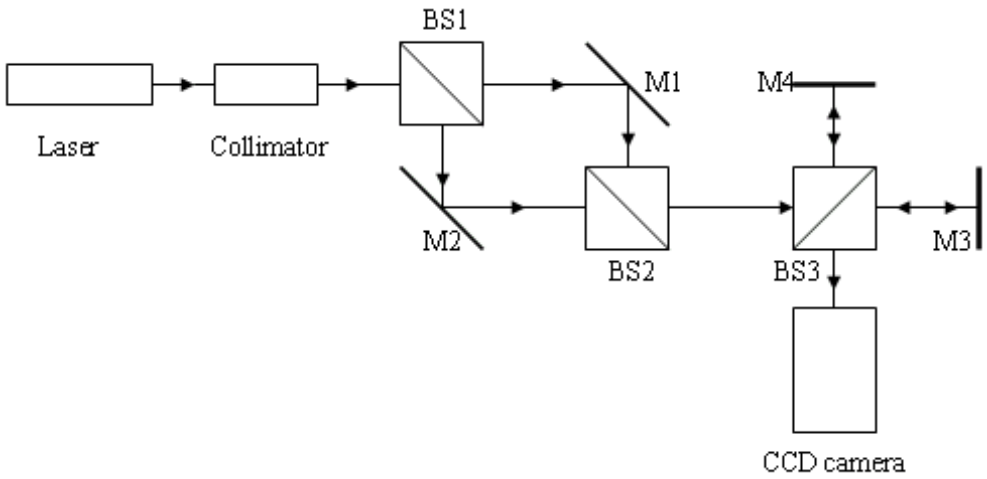

Fig.2.3. Four beam interferometric setup

2.2.2. Eight beams interferometric setup

The eight beam interferometric setup developed for the generation of array illuminator in hexagonal geometry is shown in fig.2.4 where three interferometers in tandem were

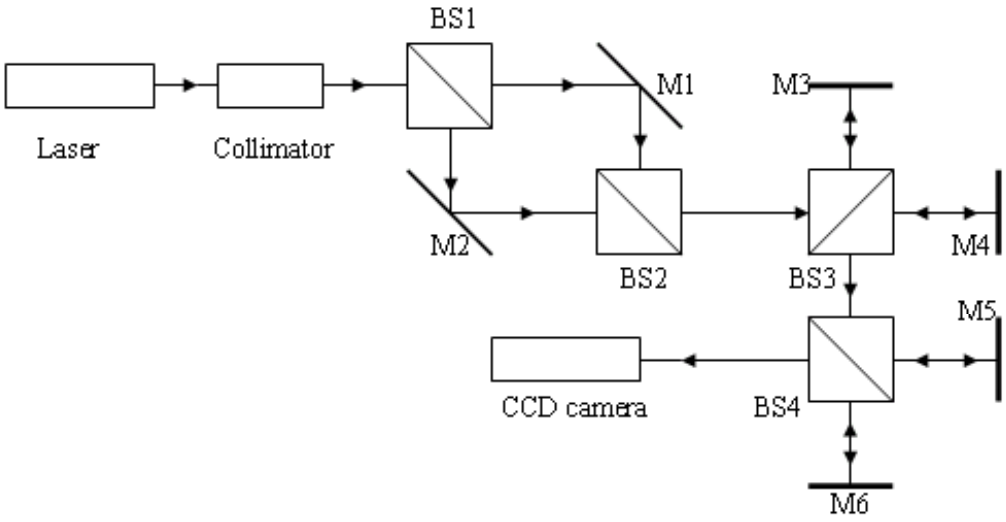

(a)

(b)

Fig.2.4.a. Experimental set up for generation of hexagonal arrays of light spots, BS1 to BS3 cube beam splitter, M1 to M6 Mirrors, b. Photograph of setup

used. The first two stages of interferometers are similar to the four beam interferometric setup of fig.2.3. The output of the four beam interferometric setup (output of BS3), illuminated the second Michelson interferometer (third stage) consisting of beam splitter BS4 and mirrors M5 and M6. At BS4 each beam was further divided into two,

giving rise to total of eight beams at the output plane. Mirror M5 was kept for normal incidence and mirror M6 was adjusted by giving tilt for the interference pattern from third stage.

To generate the regular hexagonal pattern mirror M2, M4 and M6 were given the tilt such that the interferograms from each stage are oriented 60^0 with each other and have same spatial frequencies. The beating phenomenon was observed due to little mismatch of the spatial frequencies of the interferograms. Final interference patterns of eight beams for hexagonal arrays and beating phenomenon were recorded directly onto the CCD and on the photographic films.

Far field patterns for square, rectangular, hexagonal arrays and beating phenomenon were also recorded. The arrays were compressed by using an achromat (f = 25cm.) at the output plane and recorded by CCD.

To measure the angular separations between the interfering beams, an iris diaphragm with a very small hole was placed after the collimator and the position of all beams was recorded in the transverse plane at a distance of 300 cm from the set-up (from BS4).

General expressions for the intensity distributions in the output plane of fig.2.3 and 2.4 are worked out in terms of angular separations (spatial frequencies) and locations of the beams in chapter 3 and the computed results are compared with the experimental results in chapter 4. Recorded array patterns of all the geometries were scanned for intensity distribution. The fringe visibility curves were also plotted.

2.3. Polarized setup

One of the limitations of the randomly polarized setup explained above is its poor light efficiency as the 50% light gets lost after the beam comes back at any beam splitter

from the mirrors. In order to improve the light efficiency we have developed the heterodyne interferometer using polarized light. The formation of the interference patterns and hence the arrays shows the dependence on the orientations of the polarized components.

2.3.1. Two beam interferometric setup

The experimental setup used to study the interference of two orthogonally polarized beams as a function of orientation of polarizing components is shown in fig.2.5. We have used a laser of 10mW (05-LHR-991, Melles Griot) in this setup. A collimated beam was launched into a polarizer P_1. The polarizer P_1 (03FPG003 – Melles Griot) was aligned at 45^0 to ensure 50-50 splitting of light from polarizing cube beam splitter (PBS, 03PBB005- Melles Griot). The reflected beam from PBS (only s-polarized light) was passed through Quarter Wave Plate (QWP, 02WRM015- Melles Griot) Q_1, and converted into left circularly polarized light (l.c.p.) for Q_1 oriented at 45^0 (fixed throughout the experiment) with the polarization plane of incident beam on to it. The l.c.p. beam was reflected from mirror M_1 and changed into right circularly polarized (r.c.p.) and again passed through Q_1. It was turned into p-polarized light and completely transmitted through PBS in the output. The transmitted beam (only p-polarized light) from PBS was passed through Quarter Wave Plate (QWP) Q_2 and changed into right elliptically polarized (r.e.p.) light depending on the orientation of Q_2 with respect to the polarization plane of the incident beam on Q_2. The r.e.p. beam was reflected from mirror M_2 and converted into left elliptically polarized (l.e.p.) and again passed through Q_2. It turned into linear polarized light and only the vertical polarization (s-polarization) reflected from PBS. Thus the two orthogonally linear polarized beams come out from the interferometer. These above two orthogonally polarized beams after passing

through the QWP Q_3 becomes circularly or elliptically polarized light depending upon the orientation of Q_3 and produce non-observable fringes. The fringes were observed using a polarizer P_2 at the output plane.

Using this setup the interferograms were recorded and studied for the different orientations of Q_2, Q_3 and P_2.

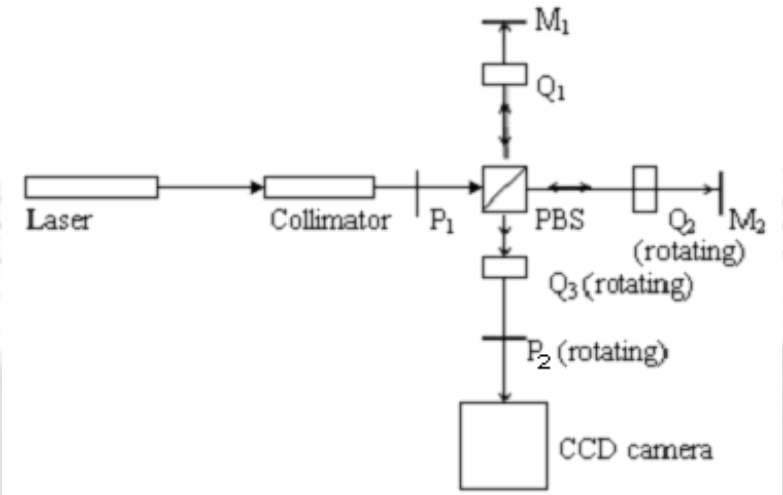

Fig.2.5. Experimental setup for interference of two orthogonally polarized light: Q_1 -Q_3 quarter wave plates, M_1, M_2 mirrors, P_1, P_2 polarizers, PBS polarizing beam splitter.

2.3.2. Polarized four beam interferometric setup

The experimental setup developed for the generation of two dimensional arrays of light spot with the polarized beams is shown in fig.2.6. The light coupling efficiency of this setup is more than that of the randomly polarized setup of fig.2.3. A collimated beam was passed through a polarizer and launched into an interferometric setup consists of two interferometers similar to two beam polarized setups in tandem as shown in fig.2.6. The first stage of the interferometer is same as the two beam interferometric setup of fig.2.5 so the output of PBS1 resulted into two orthogonal plane polarized light. These two beams were passed through a quarter wave plate Q_3 and subjected into another similar interferometric setup comprising of one polarizing beam splitter (PBS2), two

quarter wave plates (Q_4 and Q_5) and two mirrors (M_3 and M_4). Thus the output consists of four beams. The $Q_1 - Q_4$ quarter wave plates were oriented in such a way that the optic axis of the each plate makes 45^0 with respect to the polarization

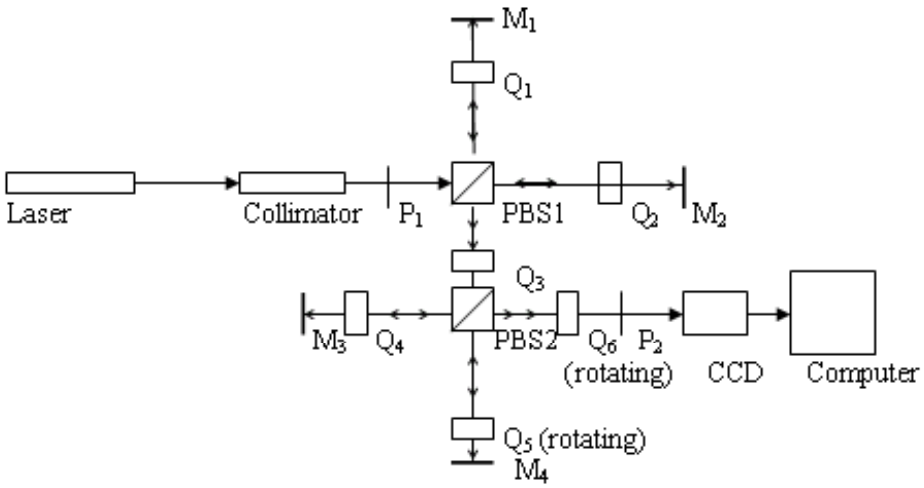

- (a)

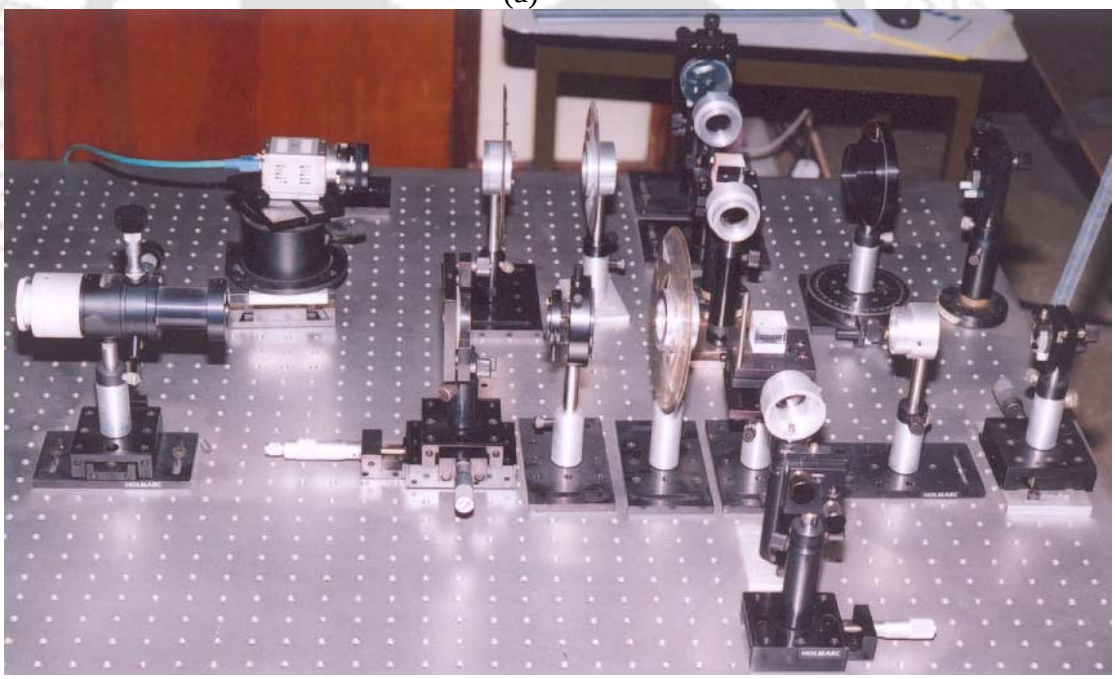

- (b)

Fig.2.6.a. Experimental setup for the generation of square arrays with the polarized beams. $P_{1,}$ P_2 : Polarizers; PBS: Polarizing Beam Splitter; $Q_{1\text{-}6}$: Quarter Wave Plates; $M_{1\text{-}4}$: Mirrors, b. Photograph of the experimental setup

plane of the light incident onto it. The output beams were passed through finally QWP Q_6 and results into non observable fringes. The fringes can be observed with the help of

2^{nd} polarizer P_2. It's orientation was maintained at 45^0 with the horizontal polarization. Mirrors M_1 and M_3 were aligned for the normal incidences and mirrors M_2 and M_4 were given tilts so that at the observation plane, square arrays were formed. The final output was recorded onto CCD as a function of azimuth of Q_5 (ρ_1) and Q_6 (ρ_2).

2.4. Measurement of the coupling efficiency

The efficiency of the interferometric configurations developed was estimated by comparing the output power at the plane of observation and the input power of the interferometers (before the first beam splitter of each setup). To measure input power, the power meter (Thorlabs - S110 2.1) was placed before BS1 in the fig.2.3 and 2.4, and before PBS1 in the fig.2.6. For the output power, the power meter was placed at the output of beam splitter BS3 in the fig.2.3, at the output of beam splitter BS4 in the fig.2.4 for randomly polarized setup, at the output plane after polarizer P_2 in the fig.2.6 for the polarized setup.

2.5. Applications of the interferometric setup

After successfully developing and analyzing the various interferometric configurations for array illuminator, the setups were tested for their applications towards a) lithography for the formation of periodic structures via selective laser ablation in a single shot and b) diagnostic for pulsed plasma system.

2.5.1. Laser ablation setup

For the selective laser ablation, two beam and four beam interferometers were assembled using the 2^{nd} harmonic of Q switched Nd:YAG laser (HYL101-Quanta System, 400 mJ in fundamental). The thin films of Indium were illuminated by the

interference patterns. The region of the thin film receiving the bright spots was ablated leaving behind the region of dark fringe unaffected.

a. Experimental setup for writing the grating

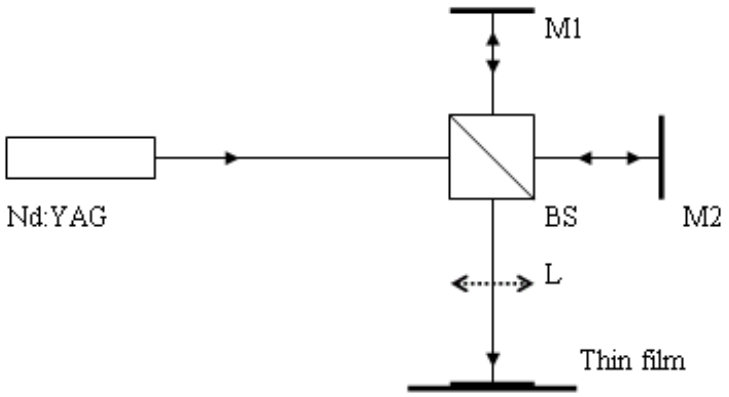

Fig.2.7 Experimental setup for lines

The 2nd harmonic of Nd:YAG laser beam was launched into a Michelson interferometer setup as shown in fig.2.7 using anti-reflected coated high damage threshold beam splitter (03BSC009-Melles Griot) and mirrors M1 and M2. The mirror M2 was adjusted for the parallel straight line fringes. An achromat of focal length 10 cm. was placed at the output to compress the fringes. The interference fringes were allowed to fall on the Indium thin film at a distance of 13cm. from the lens L. This exposed thin film was scanned with the micrograph (Zeiss Axiotech 100HD) for measurement of the periodic line structures formed as a result of selective ablation of the film in the regions of bright fringes. The complete writing was performed in a single shot of the laser.

b. Lithographic setup for two dimensional arrays

The Nd:YAG laser beam was launched in a four beam interferometric setup (two Michelson interferometers in tandem) as shown in fig.2.8 using high damage threshold optical components. The interferometric setup was aligned for the square arrays of light spots by giving appropriate tilts in the mirrors M2 and M4. These arrays illuminated the Indium thin film through an achromat. The selectively ablated region of the thin film

was scanned by micrograph. This resulted into drilling a series of tiny holes onto the thin films in square geometry in a single shot.

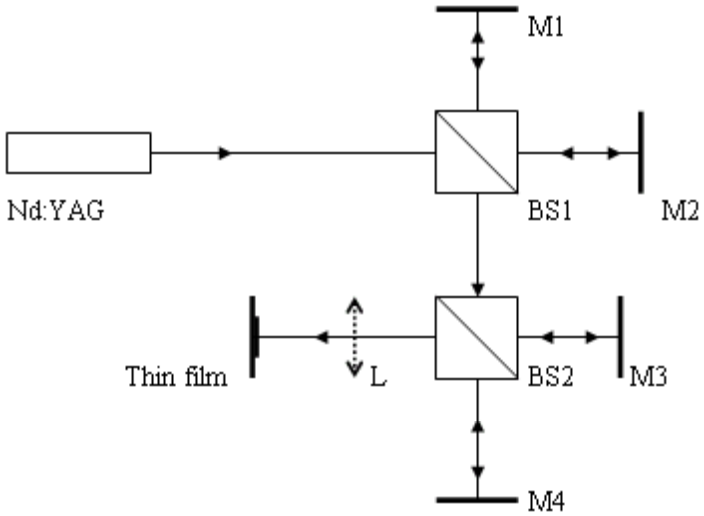

Fig.2.8 Experimental setup for arrays

2.5.2 Plasma diagnostic setup

Two beam interferometric setup using He-Ne laser was used to measure the electron density profile in a single shot in air breakdown.

a. High voltage air breakdown circuit

The pulsed plasma in air was produced by applying the pulsed high voltage (of the order of few kV) across needle shaped electrodes kept around 7mm apart as shown in fig.2.9. A small resistance (~0.324Ω), having very low inductance (~ 1.8 μH) over a wide frequency range (>200kHz), was connected towards the grounded electrode as shown. The small resistance consists of a carbon rod taken out from a cell of 1.5 volt. The resistance and inductance was measured with a bridge circuit (HIOKI 3532, LCR Hi tester) With the appropriate voltage divider network, the voltage drop across this low resistance was recorded on to the 200MHz DSO (Tektronix, TDS 360, two channel, 200 MHz, 1 Gs/s) for the measurement of the current (Plasma current) through the

spark gap. A high voltage probe (Tektronix – P6015A) along with DSO was used to measure the voltage across the spark gap.

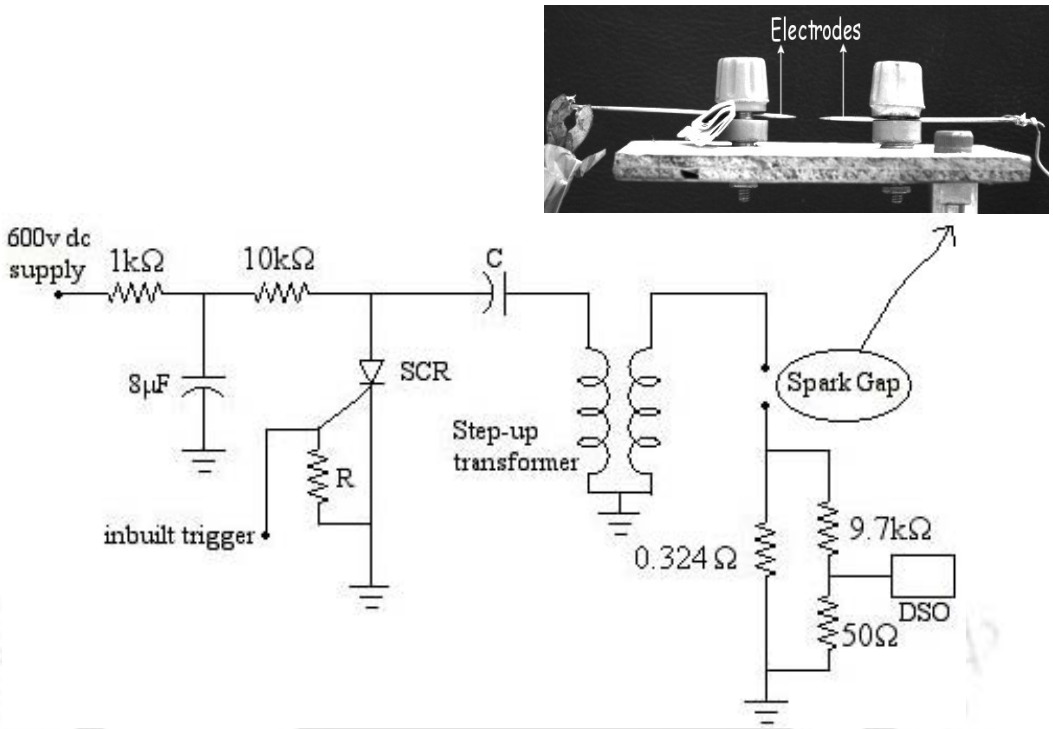

Fig.2.9. Spark Gap Circuit

b. Electron density profile measurement setup

The schematic of the experimental set-up used for recording the line integrated plasma density profile in a single shot is shown in fig.2.10. The electrodes were placed in one of the arm of the Michelson interferometer as shown in the figure. The interferometer was illuminated with a collimated He- Ne laser beam (10mW) and adjusted for the straight parallel fringes. The direction of propagation of laser beam is along z-axis as given in fig.2.11. Whenever, a pulsed high voltage is applied across the spark gap, the pulsed plasma formation results into introducing an additional path difference in the interfering beams. This additional path difference modifies the interference pattern in the region of the plasma. The modified interferogram was recorded directly on to CCD. From the measurement of the fringe shift, density of plasma was estimated. The plasma

width, required for the calculation of line integrated density, was measured by imaging the plasma in the right perspective with one is to one correspondence on to the CCD. The derivation of line integrated refractive index and hence the electron density in the spark gap in terms of fringe shift is described in chapter 3.

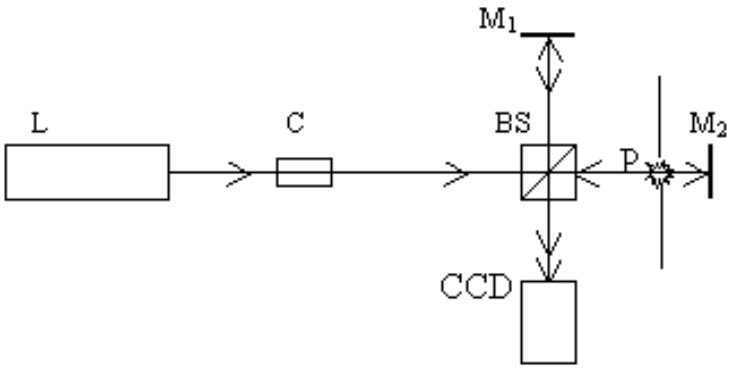

Fig.2.10. Interferometric set-up to measure the plasma density profile, L; He-Ne laser, C; collimator, BS beam splitter, M_1, M_2 mirrors, P pulsed plasma.

c. Beam deflection setup

Plasma duration was measured using the beam deflection set-up as shown in fig.2.12. A He-Ne laser beam (10mW, uncollimated) was allowed to pass through the spacing in between the two electrodes of spark gap and then on to the high speed photodiode (model 13DSH001, 0.04mm^2, Melles Griot) as shown in fig.2.12. The photodiode output is displayed on to a DSO with a 50Ω terminator as shown. In the path of the beam a neutral-density filter was placed to reduce the intensity of laser to prevent the saturation of the photodiode. The duration of the deviation of the beam is recorded by observing duration of the dip into the photodiode signal.

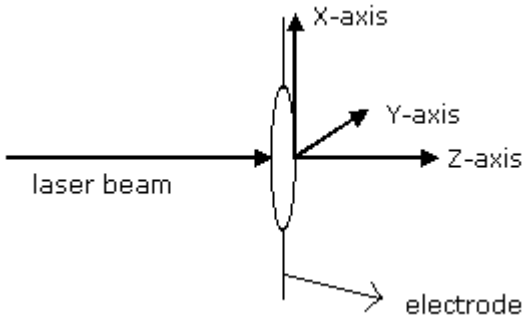

Fig. 2.11. Axis diagram with respect to electrodes and beam

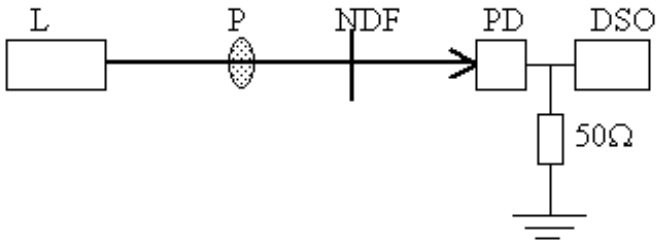

Fig.2.12. Beam deflection setup for measuring the duration of plasma, L He-Ne laser, P plasma, NDF neutral density filter, PD Photodiode, DSO digital storage oscilloscope

To conclude, in this chapter, the various interferometric configurations developed for the generation of one and two dimensional periodic arrays of light are described in details. The high power laser interferometers developed for the single step microlithography technique is also presented. Two beam interferometer is also described in this chapter for the measurement of electron density profile in spark plasma.

Chapter 3

Theoretical deduction

3.1. Theoretical Background

3.1.1. Interference

When two or more coherent light beams are superposed, the distribution of intensity cannot be described in a simple manner. If a light beam from a source is divided by suitable apparatus into two parts which are then superposed, the intensity in the region of superposition is found to vary periodically from point to point between maximum and minimum intensity. This phenomenon is called interference.

3.1.2. Superposition of two waves

Let us consider two coherent monochromatic waves having electric field E_1 and E_2 of equal amplitude A and frequency ω and both the waves are propagating in the same direction[90].

$$E_1 = A \exp[i(\omega t - \delta_1)]$$

$$E_2 = A \exp[i(\omega t - \delta_2)]$$

Where, δ_1, δ_2 are the phase of the waves.

The resultant electric field $E = E_1 + E_2$

And the intensity at any point P is $I = \langle E_1^2 \rangle + \langle E_2^2 \rangle + 2\langle E_1.E_2 \rangle \cos\delta$

Phase difference between the two waves is $\delta = \delta_1 - \delta_2 = (2\pi/\lambda)\,\Delta$

Where, Δ is the path difference between the two waves.

If the phase difference (or path difference) is varying in the transverse plane then the resultant interference pattern will show alternate bright and dark fringes.

The maxima of intensity for bright fringes are $I_{max} = I_1+I_2+2(I_1.I_2)^{1/2}$; $\delta= 2m\pi$, m= 0, 1, 2...

The minima of intensity for dark fringes are $I_{min} = I_1 + I_2 - 2(I_1.I_2)^{1/2}$; $\delta= (2m+1)\pi$, m= 0, 1, 2...

3.1.3. Michelson and Mach Zehnder interferometer

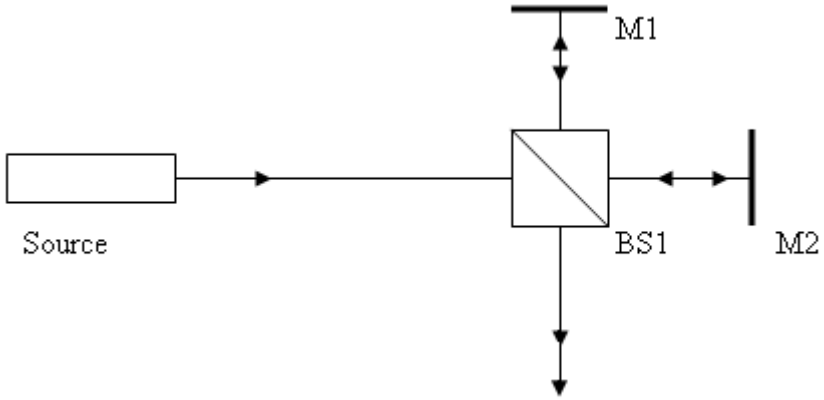

Fig.3.1. Schematic of Michelson interferometer

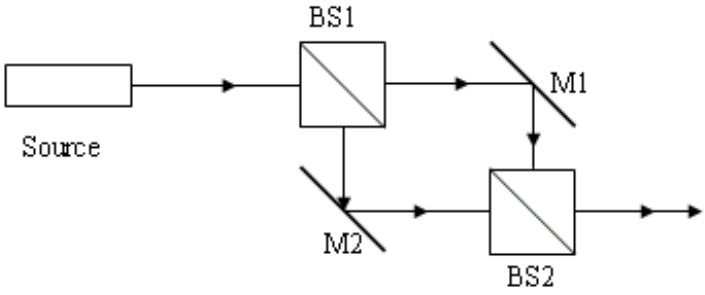

Fig.3.2. Schematic of Mach Zehnder interferometer

Michelson and Mach Zehnder interferometric configurations[90] are commonly used in interferometric setups. In the Michelson interferometer, fig.3.1 when both the mirrors are kept for normal incidences and the interferometer is illuminated with a point source, then the interference pattern is that of fringes of equal inclination, in the form of alternate dark and bright concentric fringes. When the interferometer is illuminated

with a collimated beam, and one of the mirrors is slightly tilted for non normal incidences, then the system is equivalent to that of an air wedge and the fringes of equal thickness are obtained. In this case one gets the straight parallel fringes. The path differences between the two beams (and hence the spatial frequency) will depend on the angular separation between them. In the Mach Zehnder interferometer, fig.3.2, straight parallel fringes of equal thickness can be obtained by deviating one of the mirrors little away from 45° angle of incidences.

3.1.4. Spatial frequency

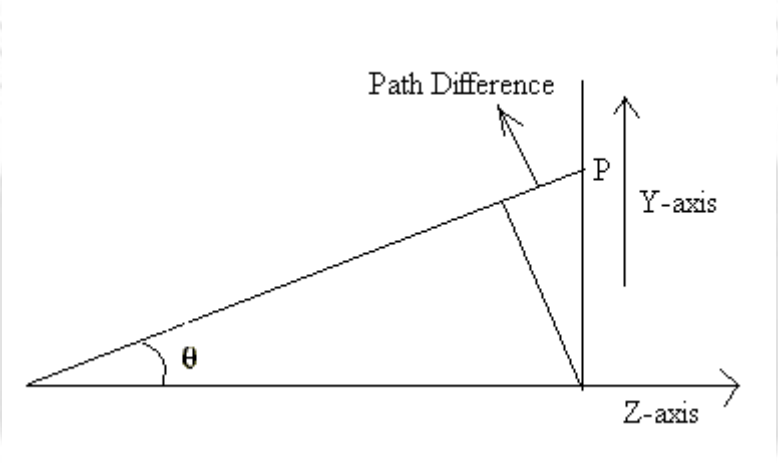

Fig.3.3. Schematic for the path difference of two interfering beams

In the present work, all the interferometric configurations were assembled for the fringes of equal thickness. The one of the beam of individual interferometric stages is always kept normal incidences and the other goes at a small angular separation as shown in fig.3.3. Beam 1 in fig.3.3 is normal beam and beam 2 goes at an angular separation of θ. On the screen, at any point P, along the y direction the phase differences between these two beam is $\delta = (2\pi/\lambda)\, y \sin\theta = \mu y$

where, μ is the spatial frequency along y direction given by $\mu = (2\pi/\lambda) \sin\theta$. In this case the fringes will be parallel to the x-axis. If the tilt is given to obtain the fringes parallel to y axis then $\delta = (2\pi/\lambda) \times \sin\theta = \nu x$

where, ν is the spatial frequency along x direction.

If the fringes are inclined at certain angle w.r.t. x-axis other than the normal, then the phase difference $\delta = \pm \mu y \pm \nu x$

3.2. Electric field for the four beams in randomly polarized setup

Four beam interferometric setup is shown in fig.2.3. The path of all four beams are given below

Beam1: BS1 $\rightarrow$ M_1 $\rightarrow$ BS2 $\rightarrow$ BS3 $\rightarrow$ M_3 $\rightarrow$ BS3 $\rightarrow$ O/P

Beam2: BS1 $\rightarrow$ M_2 $\rightarrow$ BS2 $\rightarrow$ BS3 $\rightarrow$ M_3 $\rightarrow$ BS3 $\rightarrow$ O/P

Beam3: BS1 $\rightarrow$ M_1 $\rightarrow$ BS2 $\rightarrow$ BS3 $\rightarrow$ M_4 $\rightarrow$ BS3 $\rightarrow$ O/P

Beam4: BS1 $\rightarrow$ M_2 $\rightarrow$ BS2 $\rightarrow$ BS3 $\rightarrow$ M_4 $\rightarrow$ BS3 $\rightarrow$ O/P

M_1 kept for 45° and M_3 for normal incidences and therefore the beam1 will come out at normal incidences from BS3 and it is called normal beam. Beam 1 and 2 corresponds to the interference of first stage of interferometer and M_2 is tilted to produce the horizontal fringes, parallel to x-axis. Beam 3 and 4 gives the interference of second stage and mirror M_4 is tilted for the vertical fringes parallel to y-axis. Assuming the input beam having Gaussian distribution, fig.2.2 and the direction of propagation or the longitudinal axis as z-axis, the electric field distribution u_1 to u_4 (correspond to beam 1 to beam 4 respectively) of all the four beam in the transverse plane can be written now in terms of x and y spatial frequencies.

The electric field for the four beams at the output plane of the fig.2.3 is given below

$$u_1 = \left[\frac{a}{16}\exp\left\{-\frac{(x)^2+(y)^2}{2w^2}\right\}\right] \quad (1)$$

$$u_2 = \left[\frac{a}{16}\exp\left\{-\frac{(x-x_2)^2+(y-y_2)^2}{2w^2}\right\}\right]\exp\{(-i\mu y)\} \quad (2)$$

$$u_3 = \left[\frac{a}{16}\exp\left\{-\frac{(x-x_3)^2+(y-y_3)^2}{2w^2}\right\}\right]\exp\{-i(\nu x)\} \quad (3)$$

$$u_4 = \left[\frac{a}{16}\exp\left\{-\frac{(x-x_4)^2+(y-y_4)^2}{2w^2}\right\}\right]\exp\{-i(\mu y+\nu x)\} \quad (4)$$

Where, $\mu = \frac{2\pi Sin(\theta_1)}{\lambda}$; $\nu = \frac{2\pi Sin\theta_2}{\lambda}$; a^2 is the intensity of the incident beam, θ_i (i=1,2) is angle between the two beams of i^{th} stage interferometer, 2w is the beam radius.

x_i (i=2 to 4),y_i (i= 2 to 4) are the transverse co-ordinates of center of beams 2 to 4 (corresponding Eq. 2 to 4) with respect to the normal beam 1 represented by Eq. 1. When μ = ν then the centre of all the four beams are situated at the corner of a square with beam 1 as at origin as shown in fig. 3.4 and the resultant pattern will be of square arrays. When μ ≠ ν then the centre of all the four beams will be situated at the corner of a rectangle and the interference pattern will be array of rectangular geometry.

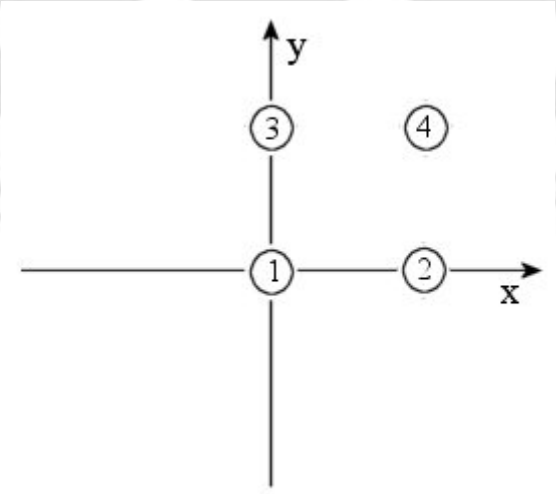

Fig.3.4. Location of centers of all the four beams on the transverse plane.

The resultant intensity $I = \left| \sum_{i=1}^{4} u_i \right|^2$ (5)

The Eq. (5) is computed for the measured values of θ_i and the results are discussed in chapter 4.

3.3. Electric field for the Eight beam Setup

The eight beam interferometric setup is shown in fig.2.4. First two stage of this configuration are same as that of the four beam setup. The output of four beam setup entered into another Michelson interferometer; third stage. In this case first stage is aligned for horizontal fringes, 2nd for 60° w.r.t. x-axis and 3rd stage is 120° w.r.t. x-axis. Accordingly the complex field distribution of the entire set of eight beams at the output plane of the fig.2.4 is given by

$$u_1 = \left[\frac{a}{64} \exp\left\{ -\frac{(x)^2 + (y)^2}{2w^2} \right\} \right] \quad (6)$$

$$u_2 = \left[\frac{a}{64} \exp\left\{ -\frac{(x-x_2)^2 + (y-y_2)^2}{2w^2} \right\} \right] \exp\{(-i\mu_1 y)\} \quad (7)$$

$$u_3 = \left[\frac{a}{64} \exp\left\{ -\frac{(x-x_3)^2 + (y-y_3)^2}{2w^2} \right\} \right] \exp\{-i(\nu_2 x - \mu_2 y)\} \quad (8)$$

$$u_4 = \left[\frac{a}{64} \exp\left\{ -\frac{(x-x_4)^2 + (y-y_4)^2}{2w^2} \right\} \right] \exp\{-i(\mu_1 y + \nu_2 x - \mu_2 y)\} \quad (9)$$

$$u_5 = \left[\frac{a}{64} \exp\left\{ -\frac{(x-x_5)^2 + (y-y_5)^2}{2w^2} \right\} \right] \exp\{-i(-\nu_3 x - \mu_3 y)\} \quad (10)$$

$$u_6 = \left[\frac{a}{64} \exp\left\{ -\frac{(x-x_6)^2 + (y-y_6)^2}{2w^2} \right\} \right] \exp\{-i(\mu_1 y - \nu_3 x - \mu_3 y)\} \quad (11)$$

$$u_7 = \left[\frac{a}{64} \exp\left\{ -\frac{(x-x_7)^2 + (y-y_7)^2}{2w^2} \right\} \right] \exp\{-i(\nu_2 x - \mu_2 y - \nu_3 x - \mu_3 y)\} \quad (12)$$

$$u_8 = \left[\frac{a}{64}\exp\left\{-\frac{(x-x_8)^2+(y-y_8)^2}{2w^2}\right\}\right]\exp\{-i(\mu_1 y+\nu_2 x-\mu_2 y-\nu_3 x-\mu_3 y)\} \qquad (13)$$

Where, $\mu_1 = \frac{2\pi Sin(\theta_1)}{\lambda}$; $\mu_2 = \frac{2\pi Sin(\theta_2 Cos\phi_2)}{\lambda}$; $\mu_3 = \frac{2\pi Sin(\theta_3 Cos\phi_3)}{\lambda}$,

$\nu_2 = \frac{2\pi Sin(\theta_2 Sin\phi_2)}{\lambda}$; $\nu_3 = \frac{2\pi Sin(\theta_3 Sin\phi_3)}{\lambda}$, a^2 is the intensity of the incident beam.

θ_i (i=1,2,3) is angle between the two beams of i^{th} stage interferometer.

ϕ_i (i=2,3) is the angle between y-axis and the line joining the two beams of i^{th} stage as shown in Fig.3.5, 2w is the beam radius.

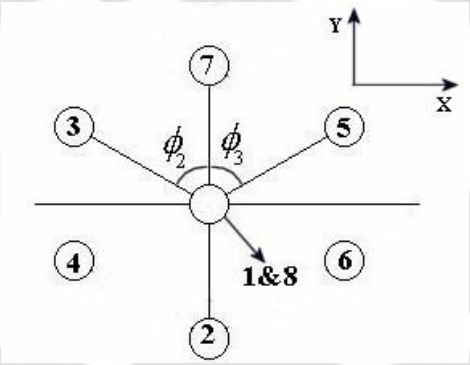

Fig.3.5. Location of centers of all the eight beams on the transverse plane.

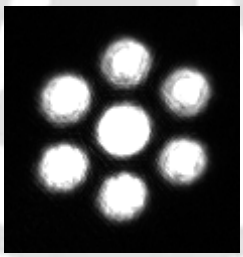

Fig.3.6. Recorded the focused hexagonal pattern

x_i (i=2to 8),y_i (i=2to 8) are the transverse co-ordinates of center of beams 2 to 8 (corresponding Eq. 6 to 13) with respect to the normal beam 1 represented by Eq. (6). as shown in Fig. 3.5. When $\mu_1 = \mu_2 = \mu_3 = \nu_2 = \nu_3$, then beam 2 to beam 7 will be situated at the corners of a regular hexagonal geometry and the beam 1 & 8 will be overlapped at the centre of the hexagon. Fig.3.6 is the focused pattern for hexagonal

array confirms the regular hexagonal geometry. Path of all eight beams have been shown in Fig.3.7.Beams 1, 2… 8 correspond to the Eq. 6, 7,… 13 respectively. For the simplicity only θ_1 has been marked in the figure.

The resultant intensity of the eight beams is given by

$$I = \left| \sum_{i=1}^{8} u_i \right|^2 \tag{14}$$

From equation (14) it is clear that the geometry and size of the arrays can be easily controlled by relative orientations of the mirrors.

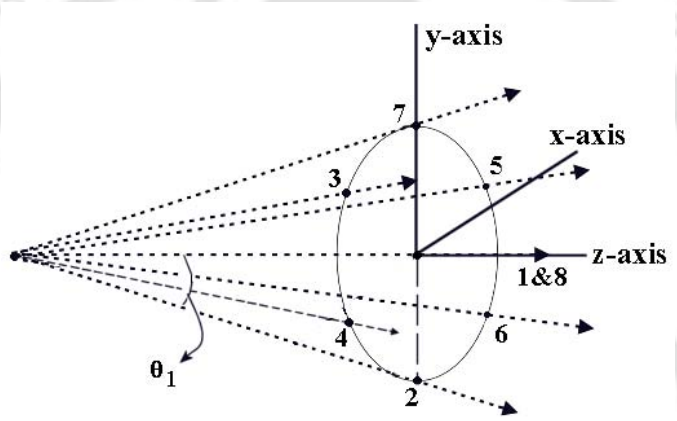

Fig.3.7. Schematic of the path of all eight beams

3.4. Interference of two polarized beams

The experimental setup for the interference of the orthogonally polarized beam is shown in fig.2.5. For the derivation of expressions for the electric field, in transverse plane, we have used Jones calculus in most of the cases. Only for the 2nd beam inside the arm of the interferometer, Mueller matrix calculations are used as the calculations are simpler for this case. Rest of the places Jones matrices are used for phase term. The polarizer P_1 of fig.2.5 was aligned at 45^0. For simplicity, using the Jones vectors[91] the electric field of the beam after P_1 is defined as $\frac{a}{2}\begin{bmatrix}1\\1\end{bmatrix}$.

The reflected beam from polarizing beam splitter (PBS) $\frac{a}{2}\begin{bmatrix}0\\1\end{bmatrix}$ (only s-polarized light) was passed through Q_1, and converted into $\frac{a}{2\sqrt{2}}\begin{bmatrix}i\\1\end{bmatrix}$ (l.c.p.) for Q_1 oriented at 45^0. The l.c.p. beam was reflected from mirror M_1 and changed into $\frac{a}{2\sqrt{2}}\begin{bmatrix}1\\i\end{bmatrix}$ (r.c.p.) and again passed through Q_1. It was turned into $\frac{a}{2}\begin{bmatrix}1\\0\end{bmatrix}$ (p-polarized light) and completely transmitted through PBS in the output.

The transmitted beam $\frac{a}{2}\begin{bmatrix}1\\0\end{bmatrix}$ (only p-polarized light) from PBS was passed through Q_2.

This beam can be represent by Mueller matrix[91] as {1,1,0,0}. After passing through Q_2 the beam is converted into right elliptical polarized light as given below

$$\frac{a^2}{4}\begin{bmatrix}1 & 0 & 0 & 0\\ 0 & Cos^2 2\rho & Sin2\rho Cos2\rho & -Sin2\rho\\ 0 & Sin2\rho Cos2\rho & Sin^2 2\rho & Cos2\rho\\ 0 & Sin2\rho & -Cos2\rho & 0\end{bmatrix}\begin{bmatrix}1\\1\\0\\0\end{bmatrix} = \frac{a^2}{4}\begin{bmatrix}1\\ Cos^2 2\rho\\ Sin2\rho Cos2\rho\\ Sin2\rho\end{bmatrix}$$

Where, ρ is the azimuth angle of the quarter wave plate Q_2.

After reflection from mirror the beam is converted into left elliptical polarized light as

$$\frac{a^2}{4}\begin{bmatrix}1\\ Cos^2 2\rho\\ -Sin2\rho Cos2\rho\\ -Sin2\rho\end{bmatrix}$$

When the l.e.p. falls back onto the Q_2 the beam is changed into plane polarized light (in the transformation matrix ρ changes to –ρ for QWP).

$$\frac{a^2}{4}\begin{bmatrix}1 & 0 & 0 & 0\\ 0 & Cos^2 2\rho & -Sin2\rho Cos2\rho & Sin2\rho\\ 0 & -Sin2\rho Cos2\rho & Sin^2 2\rho & Cos2\rho\\ 0 & -Sin2\rho & -Cos2\rho & 0\end{bmatrix}\begin{bmatrix}1\\ Cos^2 2\rho\\ -Sin2\rho Cos2\rho\\ -Sin2\rho\end{bmatrix} = \frac{a^2}{4}\begin{bmatrix}1\\ Cos4\rho\\ -Sin4\rho\\ 0\end{bmatrix} \quad (15)$$

The Stokes vector of Eq. (15) is equivalent to the Jones vector $\frac{a}{2}\begin{bmatrix} Cos2\rho \\ Sin2\rho \end{bmatrix}$. Due the polarizing property of PBS, after the reflection from PBS the 2nd beam at the output plane is converted into $\frac{a}{2}\begin{bmatrix} 0 \\ Sin2\rho \end{bmatrix}$. If the mirror M_2 is given a tilt for the horizontal fringes then this beam is $\frac{a}{2}\begin{bmatrix} 0 \\ Sin2\rho \end{bmatrix}e^{-i\mu y}$. where, spatial frequency $\mu = \frac{2\pi Sin\theta_1}{\lambda}$; θ_1 is the angular separation between the two interfering beams. Thus at the output of PBS two beams are $\frac{a}{2}\begin{bmatrix} 1 \\ 0 \end{bmatrix}$ and $\frac{a}{2}Sin2\rho\begin{bmatrix} 0 \\ 1 \end{bmatrix}e^{-i\mu y}$ respectively.

After Q_3 (where, ρ_2 is the azimuth angle of the quarter wave plate Q_3) the first beam

$$u_1 = \begin{bmatrix} e^{i\pi/4}Cos^2\rho_2 + e^{-i\pi/4}Sin^2\rho_2 & \sqrt{2}iCos\rho_2 Sin\rho_2 \\ \sqrt{2}iCos\rho_2 Sin\rho_2 & e^{-i\pi/4}Cos^2\rho_2 + e^{i\pi/4}Sin^2\rho_2 \end{bmatrix}\frac{a}{2}\begin{bmatrix} 1 \\ 0 \end{bmatrix}$$

$$= \frac{a}{2}\begin{bmatrix} e^{i\pi/4}Cos^2\rho_2 + e^{-i\pi/4}Sin^2\rho_2 \\ \sqrt{2}iCos\rho_2 Sin\rho_2 \end{bmatrix} \quad (16)$$

And the second beam

$$u_2 = \begin{bmatrix} e^{i\pi/4}Cos^2\rho_2 + e^{-i\pi/4}Sin^2\rho_2 & \sqrt{2}iCos\rho_2 Sin\rho_2 \\ \sqrt{2}iCos\rho_2 Sin\rho_2 & e^{-i\pi/4}Cos^2\rho_2 + e^{i\pi/4}Sin^2\rho_2 \end{bmatrix}\frac{a}{2}Sin2\rho\begin{bmatrix} 0 \\ 1 \end{bmatrix}$$

$$= \frac{a}{2}Sin2\rho\begin{bmatrix} \sqrt{2}iCos\rho_2 Sin\rho_2 \\ e^{-i\pi/4}Cos^2\rho_2 + e^{i\pi/4}Sin^2\rho_2 \end{bmatrix}e^{-i\mu y} \quad (17)$$

These two elliptically polarized beams, represented by Eq. (16) and (17), after passing through P_2 oriented at an azimuth θ, the beam 1 is

$$u_1 = \frac{a}{2}\begin{bmatrix} Cos^2\theta & Sin\theta Cos\theta \\ Sin\theta Cos\theta & Sin^2\theta \end{bmatrix}\begin{bmatrix} e^{i\pi/4}Cos^2\rho_2 + e^{-i\pi/4}Sin^2\rho_2 \\ \sqrt{2}iCos\rho_2 Sin\rho_2 \end{bmatrix}$$

$$= \frac{a}{2}\left[(e^{i\pi/4}Cos^2\rho_2 + e^{-i\pi/4}Sin^2\rho_2)Cos\theta + \sqrt{2}iSin\rho_2 Cos\rho_2 Sin\theta\right]\begin{bmatrix} Cos\theta \\ Sin\theta \end{bmatrix} \quad (18)$$

and beam 2 after P_2 (θ)

$$u_2 = \frac{a}{2} Sin2\rho \begin{bmatrix} Cos^2\theta & Sin\theta Cos\theta \\ Sin\theta Cos\theta & Sin^2\theta \end{bmatrix} \begin{bmatrix} \sqrt{2}iCos\rho_2 Sin\rho_2 \\ e^{-i\pi/4}Cos^2\rho_2 + e^{i\pi/4}Sin^2\rho_2 \end{bmatrix} e^{-i\mu y}$$

$$= \frac{a}{2} Sin2\rho \left[(e^{-i\pi/4}Cos^2\rho_2 + e^{i\pi/4}Sin^2\rho_2)Sin\theta + \sqrt{2}iCos\rho_2 Sin\rho_2 Cos\theta \right] \begin{bmatrix} Cos\theta \\ Sin\theta \end{bmatrix} e^{-i\mu y} \quad (19)$$

These are general expressions for the two interfering beams at the output plane given by Eq. (18) and (19). The effects of individual polarized components are discussed below.

3.4.1. Phase shift due to the rotation of Analyzer (θ)

For analyzing the effect of the only azimuth angle of polarizer and hence the phase shift due to the polarizer onto the interferogram Q_2 and Q_3 were aligned at 45° with respect to polarization plane of the incident beam on the respective QWP and P_2 was rotated.

From Eq. (18), (19) the two beams are $\frac{a}{2\sqrt{2}} e^{i\theta} \begin{bmatrix} Cos\theta \\ Sin\theta \end{bmatrix}$ and $\frac{a}{2\sqrt{2}} e^{i(\pi/2-\theta-\mu y)} \begin{bmatrix} Cos\theta \\ Sin\theta \end{bmatrix}$

The resultant intensity

$$I = |uu^*| = \left[u_1 e^{i(\omega t+\phi_1)} + u_2 e^{i(\omega t+\phi_2)} \right] \left[u_1 e^{-i(\omega t+\phi_1)} + u_2 e^{-i(\omega t+\phi_2)} \right]$$

$$= \frac{a^2}{4} \left[1 + Sin(2\theta + \mu y) \right] \quad (20)$$

This shows clearly that if analyzer is rotated at any angle θ, an additional phase difference of 2θ is introduced between the two interfering beams and there will be corresponding fringe shift. This fringe shift can be recorded as a function of θ onto CCD. From the Eq. (20) the condition for minima for the nth order fringe is $2\theta + \mu y = (2n - ½)\pi$. Since spatial frequency μ is constant for the given setup and so the location of fringe for any particular order will change linearly with respect to the azimuthal angle θ.

3.4.2. Rotation of quarter wave plate Q_2 of one of the arm (ρ)

If Q_3 and P_2 were aligned at 45^0 and Q_2 was rotated, the field distribution at the output plane for the two interfering beams from Eq. (18) and (19) are

$$u_1 = \frac{a(1+i)}{4\sqrt{2}}\begin{bmatrix}1\\1\end{bmatrix} \tag{21}$$

$$u_2 = \frac{a(1+i)}{4\sqrt{2}}\begin{bmatrix}1\\1\end{bmatrix} Sin2\rho e^{-i\mu y} \tag{22}$$

ρ is the azimuth angle of Q_2.

The resultant intensity distribution in the output plane is $I = \left|\sum_{i=1}^{2} u_i\right|^2$ (23)

The intensity of the 2nd beam (Eq.24) depends on ρ. Hence fringe contrast will depend onto the orientation ρ.

3.4.3. Rotation of quarter wave plate Q_3 at the output (ρ_2)

To check the relative ellipticity of the two beams on the interference pattern, Q_2 and P_2 were aligned at 45^0 and Q_3 was rotated, the field distribution at the output plane of the two interfering beams from Eq. (18) and (19) are

$$u_1 = \frac{a}{4}\left[e^{i\pi/4}Cos^2\rho_2 + e^{-i\pi/4}Sin^2\rho_2 + \sqrt{2}iCos\rho_2 Sin\rho_2\right]\begin{bmatrix}1\\1\end{bmatrix} \tag{24}$$

$$u_2 = \frac{a}{4}\left[e^{-i\pi/4}Cos^2\rho_2 + e^{i\pi/4}Sin^2\rho_2 + \sqrt{2}iCos\rho_2 Sin\rho_2\right]\begin{bmatrix}1\\1\end{bmatrix} e^{-i\mu y} \tag{25}$$

3.5. Polarized four beam setup

The experimental setup used for the generation of square arrays from the orthogonally polarized light is shown in fig.2.6.

It is a two stage polarized interferometer. Both the stages are similar to the one described in section 3.4. Therefore the Jones vector for the two orthogonally polarized beams after PBS1 in the output of the first stage with Q_1 and Q_2 at 45° are $\frac{a}{2}\begin{bmatrix}1\\0\end{bmatrix}$ and $\frac{a}{2}\begin{bmatrix}0\\1\end{bmatrix}e^{-i\mu y}$ respectively. Then the two beams passes through Q_3 at 45° and converted

into two orthogonally circularly polarized lights given by $\frac{a}{2\sqrt{2}}\begin{bmatrix}1\\ i\end{bmatrix}$ and $\frac{a}{2\sqrt{2}}\begin{bmatrix}i\\ 1\end{bmatrix}e^{-i\mu y}$ respectively.

After passing through the 2nd stage, at the output plane of PBS2, before Q_6 all the four beams are

$$\frac{a}{2\sqrt{2}}\begin{bmatrix}1\\ 0\end{bmatrix},\ \frac{a}{2\sqrt{2}}\begin{bmatrix}1\\ 0\end{bmatrix}e^{-i\mu y},\ \frac{a}{2\sqrt{2}}Sin2\rho_1\begin{bmatrix}0\\ 1\end{bmatrix}e^{-i\nu x},\ \text{and}\ \frac{a}{2\sqrt{2}}Sin2\rho_1\begin{bmatrix}0\\ 1\end{bmatrix}e^{-i(\mu y+\nu x)}$$

Where, $\mu=\frac{2\pi Sin(\theta_1)}{\lambda}$; $\nu=\frac{2\pi Sin\theta_2}{\lambda}$; ρ_1 and ρ_2 are the azimuth of Q_5 and Q_6 respectively.

Thus in the output we have two pairs of orthogonally polarized light and the interference of these four beam is fringe free field. After passing through the QWP Q_6 the beams are converted into circular or elliptical polarized lights depending on the orientation of Q_6 (ρ_2).

$$u_1=\frac{a}{2\sqrt{2}}\begin{bmatrix}e^{i\pi/4}Cos^2\rho_2+e^{-i\pi/4}Sin^2\rho_2\\ \sqrt{2}iSin\rho_2Cos\rho_2\end{bmatrix}$$

$$u_2=\frac{a}{2\sqrt{2}}\begin{bmatrix}e^{i\pi/4}Cos^2\rho_2+e^{-i\pi/4}Sin^2\rho_2\\ \sqrt{2}iSin\rho_2Cos\rho_2\end{bmatrix}e^{-i\mu y}$$

$$u_3=\frac{a}{2\sqrt{2}}Sin2\rho_1\begin{bmatrix}\sqrt{2}iCos\rho_2Sin\rho_2\\ e^{-i\pi/4}Cos^2\rho_2+e^{i\pi/4}Sin^2\rho_2\end{bmatrix}e^{-i\nu x}$$

$$u_4=\frac{a}{2\sqrt{2}}Sin2\rho_1\begin{bmatrix}\sqrt{2}iCos\rho_2Sin\rho_2\\ e^{-i\pi/4}Cos^2\rho_2+e^{i\pi/4}Sin^2\rho_2\end{bmatrix}e^{-i(\mu y+\nu x)}$$

If the output polarizer P_2 is kept at 45°, the complex field distribution of the entire set of four beams at the output plane is given by

$$u_1=\frac{a}{4\sqrt{2}}\left[e^{i\pi/4}Cos^2\rho_2+e^{-i\pi/4}Sin^2\rho_2+\sqrt{2}iCos\rho_2Sin\rho_2\right]\begin{bmatrix}1\\ 1\end{bmatrix} \quad (26)$$

$$u_2=\frac{a}{4\sqrt{2}}\left[e^{i\pi/4}Cos^2\rho_2+e^{-i\pi/4}Sin^2\rho_2+\sqrt{2}iCos\rho_2Sin\rho_2\right]\begin{bmatrix}1\\ 1\end{bmatrix}e^{-i\mu y} \quad (27)$$

$$u_3 = \frac{a}{4\sqrt{2}} Sin2\rho_1 \left[\sqrt{2}iCos\rho_2 Sin\rho_2 + e^{-i\pi/4} Cos^2\rho_2 + e^{i\pi/4} Sin^2\rho_2 \right] \begin{bmatrix} 1 \\ 1 \end{bmatrix} e^{-i\nu x} \quad (28)$$

$$u_4 = \frac{a}{4\sqrt{2}} Sin2\rho_1 \left[\sqrt{2}iCos\rho_2 Sin\rho_2 + e^{-i\pi/4} Cos^2\rho_2 + e^{i\pi/4} Sin^2\rho_2 \right] \begin{bmatrix} 1 \\ 1 \end{bmatrix} e^{-i(\mu y + \nu x)} \quad (29)$$

The resultant intensity at the output $I = |uu^*|$ (30)

where, $u = \sum_{i=1}^{4} u_i$

Eq. 26 to 29 shows that the contrast of the interference patterns will depend upon ρ_1 and ρ_2.

3.5.1. Array generation

For generation of the arrays having maximum contrast, $\theta = \rho_1 = \rho_2 = 45°$, then the expressions for the electric field for the four beams at the output plane from Eq. 26 - 29 are

$$u_1 = \frac{a}{8}[1+i] \begin{bmatrix} 1 \\ 1 \end{bmatrix} \quad (31)$$

$$u_2 = \frac{a}{8}[1+i] \begin{bmatrix} 1 \\ 1 \end{bmatrix} e^{-i\mu y} \quad (32)$$

$$u_3 = \frac{a}{8}[1+i] \begin{bmatrix} 1 \\ 1 \end{bmatrix} e^{-i\nu x} \quad (33)$$

$$u_4 = \frac{a}{8}[1+i] \begin{bmatrix} 1 \\ 1 \end{bmatrix} e^{-i(\mu y + \nu x)} \quad (34)$$

3.5.2. QWP rotation of Q_5 (ρ_1) of the 2nd stage interferometer

If Q_6 and P_2 were aligned at 45^0 and Q_5 was rotated, the field distribution at the output plane for the four interfering beams (from Eq. 26 - 29)

$$u_1 = \frac{a}{8}[1+i] \begin{bmatrix} 1 \\ 1 \end{bmatrix} \quad (35)$$

$$u_2 = \frac{a}{8}[1+i] \begin{bmatrix} 1 \\ 1 \end{bmatrix} e^{-i\mu y} \quad (36)$$

$$u_3 = \frac{a}{8} Sin2\rho_1 [1+i] \begin{bmatrix} 1 \\ 1 \end{bmatrix} e^{-i\nu x} \tag{37}$$

$$u_4 = \frac{a}{8} Sin2\rho_1 [1+i] \begin{bmatrix} 1 \\ 1 \end{bmatrix} e^{-i(\mu y+\nu x)} \tag{38}$$

The resultant intensity distribution in the output plane is $I = \left| \sum_{i=1}^{4} u_i \right|^2$ (39)

3.5.3 QWP Q_6 (ρ_2) rotation at the output plane

If Q_5 and P_2 were aligned at 45^0 and Q_6 was rotated, the field distribution at the output plane of the two interfering beams

$$u_1 = \frac{a}{4\sqrt{2}} \left[e^{i\pi/4} Cos^2\rho_2 + e^{-i\pi/4} Sin^2\rho_2 + \sqrt{2}iCos\rho_2 Sin\rho_2 \right] \begin{bmatrix} 1 \\ 1 \end{bmatrix} \tag{40}$$

$$u_2 = \frac{a}{4\sqrt{2}} \left[e^{i\pi/4} Cos^2\rho_2 + e^{-i\pi/4} Sin^2\rho_2 + \sqrt{2}iCos\rho_2 Sin\rho_2 \right] \begin{bmatrix} 1 \\ 1 \end{bmatrix} e^{-i\mu y} \tag{41}$$

$$u_3 = \frac{a}{4\sqrt{2}} \left[\sqrt{2}iCos\rho_2 Sin\rho_2 + e^{-i\pi/4} Cos^2\rho_2 + e^{i\pi/4} Sin^2\rho_2 \right] \begin{bmatrix} 1 \\ 1 \end{bmatrix} e^{-i\nu x} \tag{42}$$

$$u_4 = \frac{a}{4\sqrt{2}} \left[\sqrt{2}iCos\rho_2 Sin\rho_2 + e^{-i\pi/4} Cos^2\rho_2 + e^{i\pi/4} Sin^2\rho_2 \right] \begin{bmatrix} 1 \\ 1 \end{bmatrix} e^{-i(\mu y+\nu x)} \tag{43}$$

The resultant intensity distribution in the output plane is $I = \left| \sum_{i=1}^{4} u_i \right|^2$ (44)

3.6. Fringe Visibility

Quality of interference pattern depends on the fringe contrast which is measured as fringe visibility = $(I_{max}-I_{min})/ (I_{max}+I_{min})$. From the recorded interference patterns of all the configurations, the fringe visibility was measured and computed from Eq. (5), (14), (23) and (44). These results are given in chapter 4 and 5.

3.7. Plasma Diagnostics

The Michelson interferometer was used to measure the electron density in a spark plasma. The presence of plasma in one arm of the interferometer modifies the

interference pattern which is observed as a fringe shift. By measuring the fringe shift electron density in the plasma can be calculated.

3.7.1. Relation between plasma density and fringe shift

In the absence of plasma, suppose that the fringe separation is d. If the shift in the fringe is δd in the presence of plasma, then corresponding phase difference is,

$$\delta\phi = (2\pi/d)\,\delta d \tag{45}$$

If δn is the change in refractive index averaged over the z-axis in presence of plasma then the corresponding phase shift

$$\delta\phi = (2\pi/\lambda)\,2\,\delta n\, l \tag{46}$$

Where l is travel length in plasma, assuming a cylindrical shaped plasma of diameter l having the axis along the line of joining the electrodes (as shown in fig.3.8) and λ is the wavelength of laser. In Eq. (46), the actual optical path difference is $\int_0^l \delta n(z)\partial z$, which was approximated as δn l, where δn is the average refractive index along the z-axis over the travel length (l) of laser in the plasma. The factor of 2 on the R.H.S. of Eq. (46) is due to the fact that beam travels through the plasma twice in a Michelson interferometer as shown in fig.2.10.

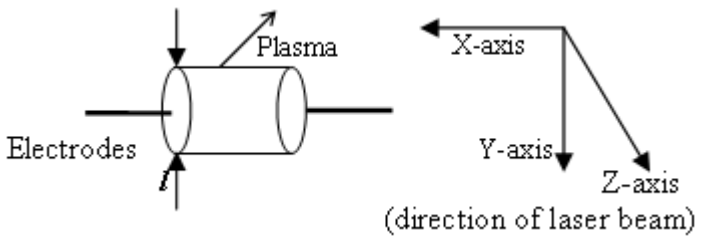

Fig. 3.8. Axis diagram with respect to electrodes and beam, l is the plasma width

From (45) and (46)

$$\delta n = \lambda\,\delta d / (2\,d\,l) \tag{47}$$

Now plasma frequency ω_p can be expressed in terms of δn as[115],

$$\omega_p = \omega \sqrt{\{2\delta n - \delta n^2\}} \quad (48)$$

where, ω is the frequency of the laser.

In terms of plasma frequency, the average electron density along the z-axis is given by

$$n_e = (\omega_p / q)^2 \, m \, \varepsilon_0 \quad (49)$$

where, m is the mass of electron, q is the electronic charge, ε_0 is the permittivity of free space.

Since the density of plasma in the spark gap is not uniform hence the electron density expressed as above is the line integrated electron density.

Chapter 4

Square, rectangular and hexagonal arrays by randomly polarized light

4.1. Introduction

The use of two Michelson interferometers in tandem for the generation of arrays of light spots in square geometry was reported for the first time[77] in 1994. The formation of hexagonal arrays via interferometers using three beams[24] (120° with each other) and three non coplanar waves[85] was reported in 1997 and in 2001 respectively. The delocalized hexagonal arrays using three nearly collimated beams was reported[81] in 1993 but this configurations has the limitations of no online control on spatial frequency.

In the present work, we have used four and eight beam interference for the generation and characterizations of square, rectangular and hexagonal patterns with randomly polarized light. For four beam interference, two interferometers in tandem and for eight beam, three interferometers in tandem were used as shown in fig.2.3 and fig.2.4 respectively. These configurations have the advantage of online control on the geometry and the spatial frequencies of arrays and also being delocalized along large longitudinal distances. The near field and far field pattern were recorded onto the CCD

and analyzed for the fringe visibilities. The recorded patterns were compared with the theoretical expressions worked in chapter 3.

4.2. Square and rectangular arrays of tiny light spots

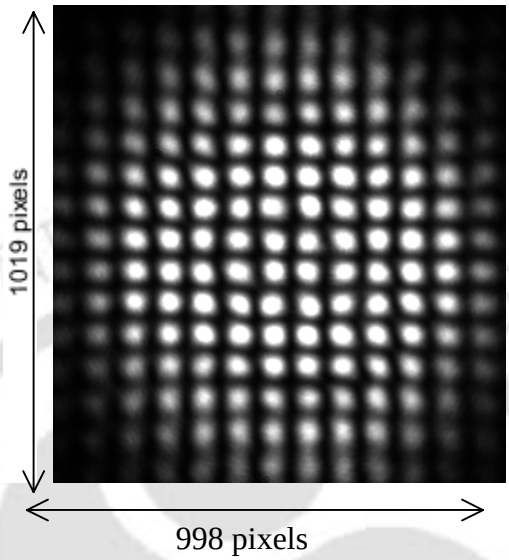

Fig.4.1. Near field square array pattern recorded onto CCD

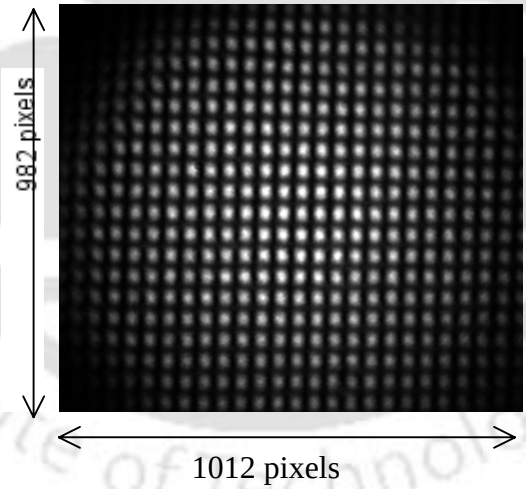

Fig.4.2. Near field rectangular array pattern recorded onto CCD

The near field square and rectangular array patterns recorded onto CCD by using the setup of fig.2.3 is shown in fig.4.1 and 4.2 respectively. For these arrays, the interference patterns from the individual interferometric stages are oriented perpendicular to each other. For the square pattern the spatial frequencies of both the

stages were same (μ = ν). The measured values of θ's for the pattern of fig.4.1 is $\theta_1 = \theta_2 = 1.23$ mrad.

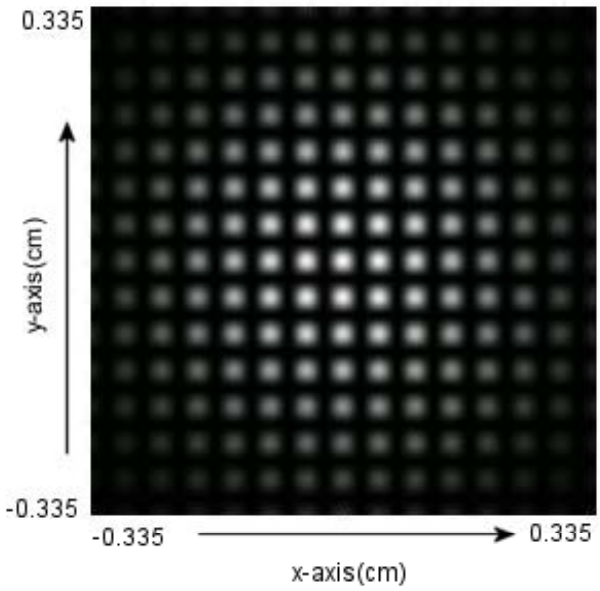

Fig.4.3. Computed pattern for near field square array

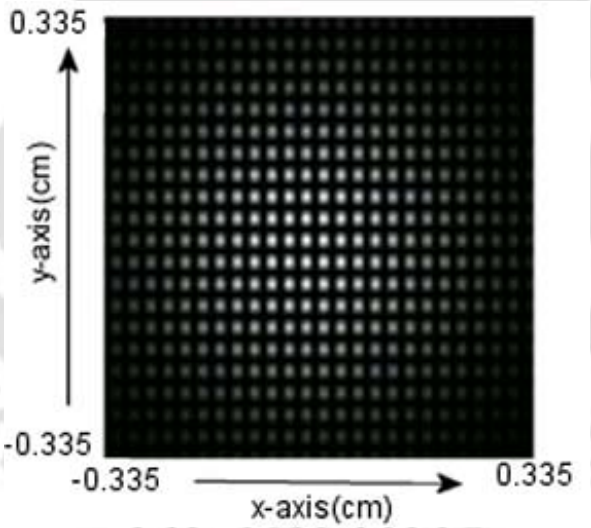

Fig.4.4. Computed pattern for near field rectangular array

The rectangular patterns were obtained for the mismatch of spatial frequencies (μ ≠ ν) of the two stages. The recorded rectangular array is shown in Fig.4.2. The corresponding measured values of θ_1 and θ_2 were 2.33 mrad and 1.87 mrad respectively. The Eq. (5) was computed for the above observed values of θ's for both,

square and rectangular arrays and computed patterns are shown in fig.4.3 and fig.4.4 respectively.

The intensity distribution curves along the x-axis are plotted in the fig.4.5 and fig.4.6 for the square and rectangular arrays of fig.4.1 and fig.4.2 respectively.

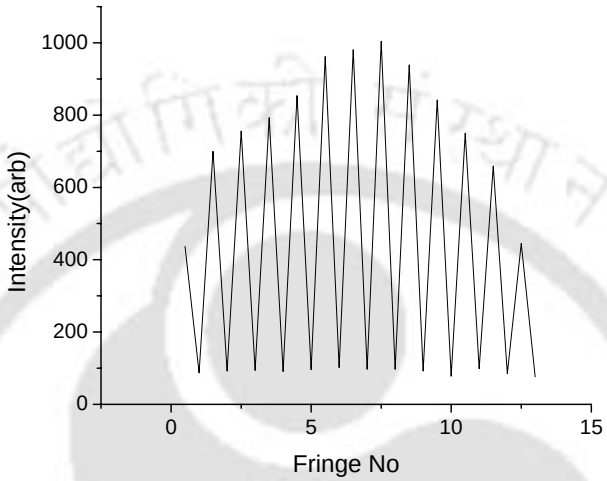

Fig.4.5. Intensity distribution along x-axis for square array

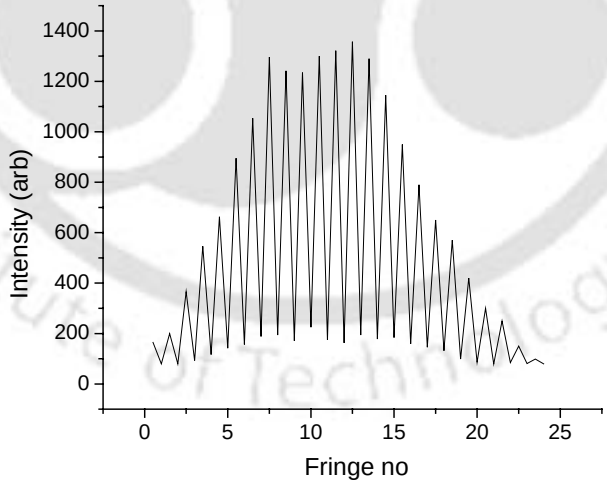

Fig.4.6. Intensity distribution along x-axis for rectangular array

The fringe visibility was calculated from the intensity distribution and plotted in the fg.4.7 and 4.8 for the square and rectangular array geometry respectively. From the

fringe visibility curve it is clear that one can generate the matrix of large number of tiny spots with a very good contrast in the regular geometry.

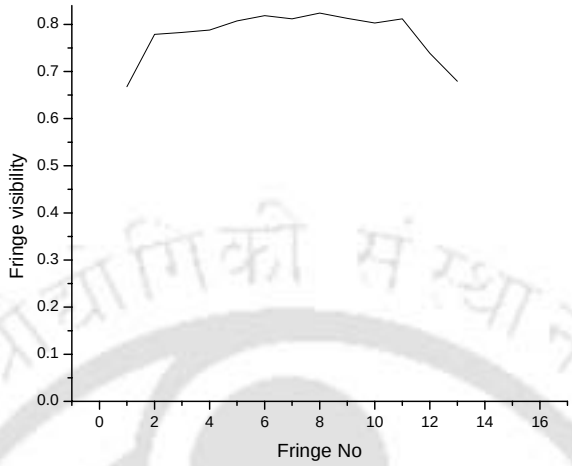

Fig.4.7. Fringe visibility curve along x-axis for square array

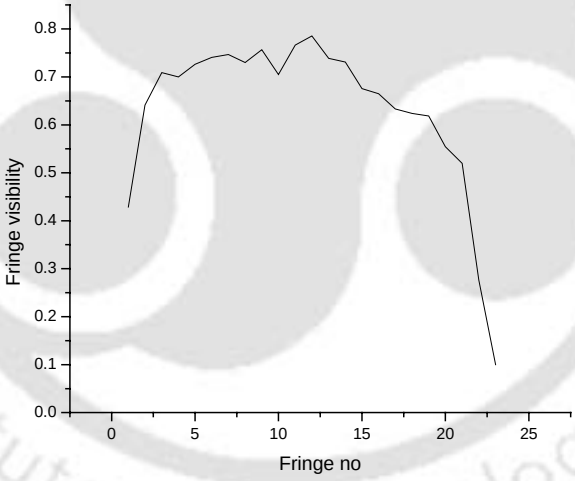

Fig.4.8. Fringe visibility curve along x-axis for rectangular array

Use of collimated beams ensures that the spatial frequencies of the interferograms do not change along the z-axis and hence the size and configuration of the resultant arrays remain unaffected to the plane of observation along the longitudinal direction. The intensity distribution along the transverse plane has a z-dependency in terms of

location of individual beams in the Gaussian distributions. For a beam having beam radius 2w the pattern can be observed up to a longitudinal distance of $2w/\tan\theta$. Beyond

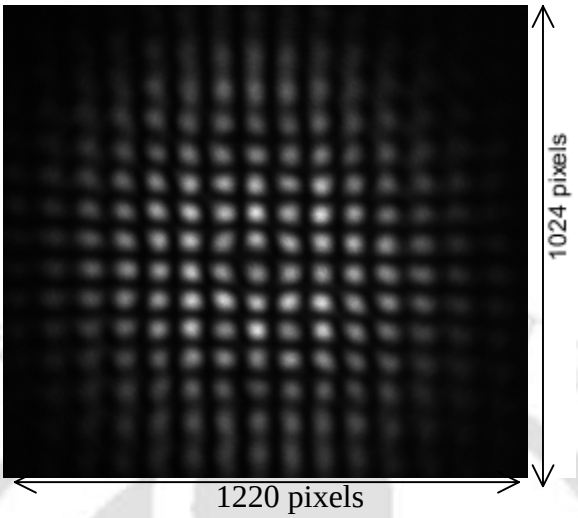

Fig.4.9. Far field pattern of square array recorded onto CCD at a distance of 2.5m

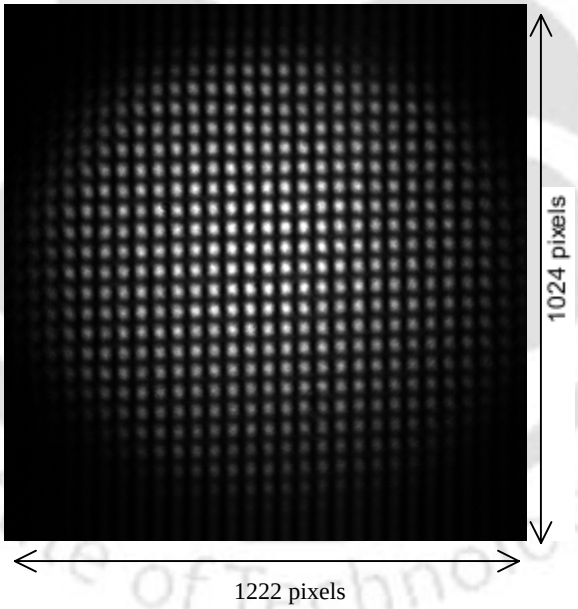

Fig.4.10. Far field pattern of rectangular array recorded onto CCD at a distance of 2.5m.

that gradually the overlap region among the beams will start reducing and hence the size of the pattern and finally all the beams will go apart without any overlap. Interference pattern were scanned upto a distances of 2.5 m without any significant distortion and loss of contrast. Moreover, no. of spots were also same as that of

observed in the near field pattern of fig.4.1 and fig.4.2. The recorded far field pattern at a distance of 2.5 m is shown in fig.4.9 and fig.4.10 respectively for the square and rectangular array geometry. The corresponding far field computed patterns are shown in fig.4.11 and fig.4.12 respectively.

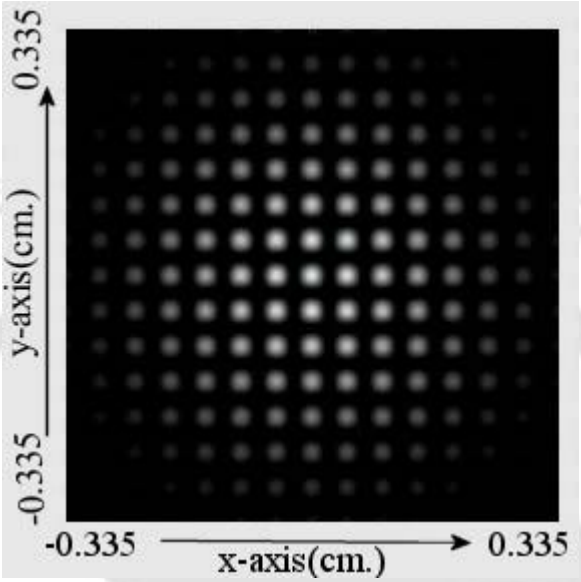

Fig.4.11. Computed far field pattern for square array

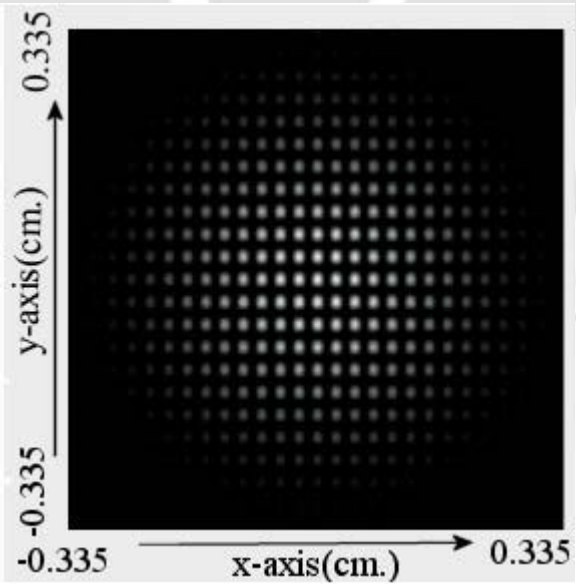

Fig.4.12. Computed far field pattern for rectangular array

As the beams are propagating at small angular separation so the arrays can be compressed using an achromat at the output plane. A lens of focal length 25 cm was placed in the path of output beams to record the compressed pattern. The CCD was

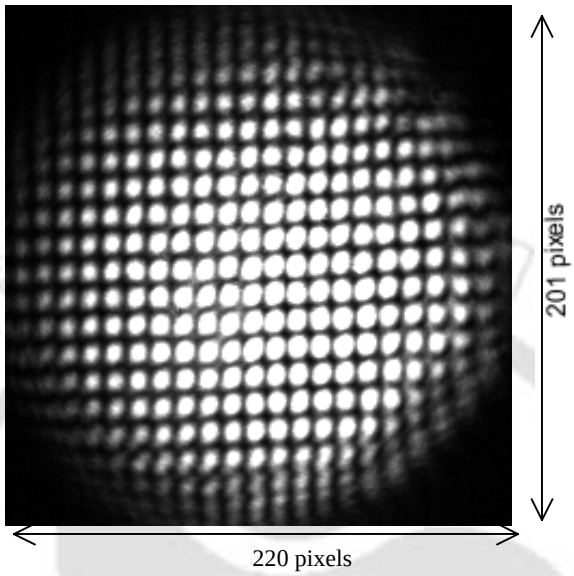

Fig.4.13. Compressed Pattern for square arrays.

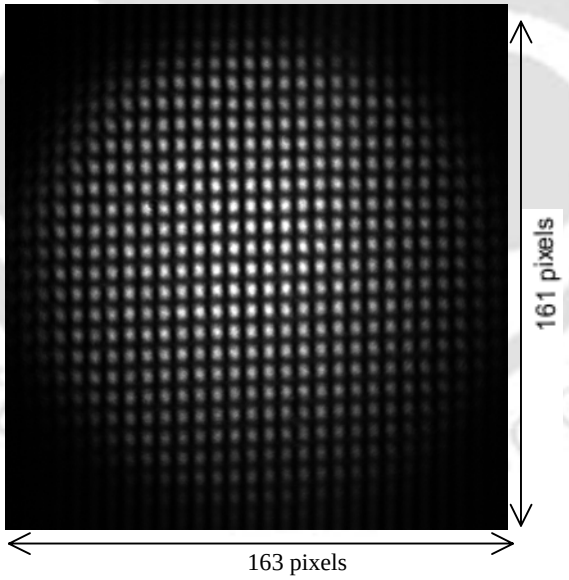

Fig.4.14. Compressed Pattern for rectangular arrays.

placed at a distance of 34.5cm away from the lens. At the focal plane all four beams will be focused at four different positions in the transverse plane in a square or rectangular geometry depending on θ_i's. The recorded compressed patterns are shown in fig.4.13 and fig.4.14. The compression factors in these patterns are 5 & 7

respectively. No of spots can be further increased than what is observed above by increasing θ_i's but the distances up to which the pattern can be observed will reduce. One such recorded rectangular pattern is shown in fig.4.15, corresponding to θ_1 = 3.3mrad and θ_2=2.9mrad. This pattern could be further compressed using a lens. The recorded compressed pattern is shown in fig.4.16 containing more than 900spots/mm^2 having more than 2500 tiny spots of light.

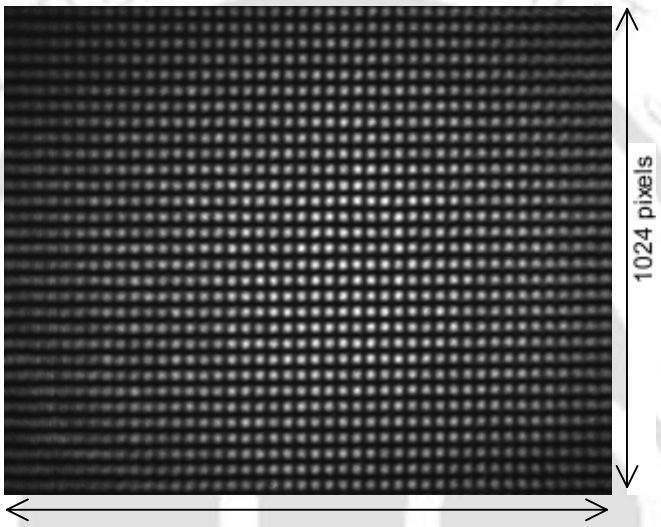

Fig.4.15. Uncompressed pattern rectangular array pattern of θ_1=3.3 and θ_2 = 2.9 mrad.

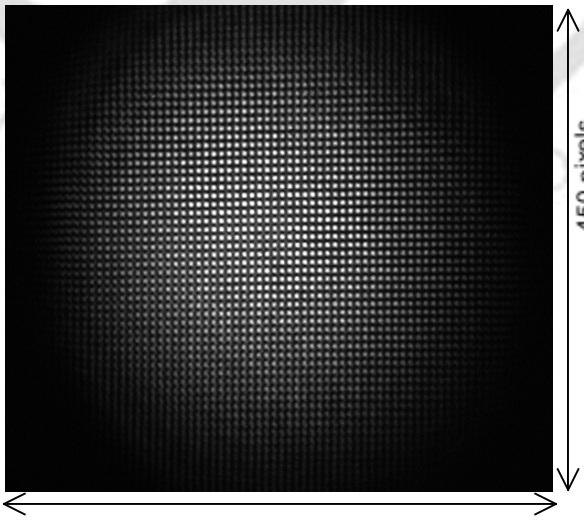

Fig.4.16. Compressed pattern for the above with large spot density (around 900 /mm^2).

4.3. Hexagonal arrays of light spots

Three interferometers in tandem, as shown in fig.2.4 were used for generating eight interfering beams. When the patterns from all the individual three stages of fig.2.4 were oriented at 60° with respect to each other and were of exactly same spatial frequency, then the resultant interference pattern from eight beams was of regular hexagonal geometry. The near field hexagonal pattern of regular geometry recorded onto photographic film is shown in the fig.4.17. The measured values for angle (θ_i) between the beams were $\theta_1 = \theta_2 = \theta_3 =$ 1.33 mrad and angle between y-axis and the line joining the two beams (ϕ_i), fig.3.6, were $\phi_2 = \phi_3 = 60^0$. The corresponding near field computed patterns is shown in fig.4.18. For the near field interference pattern, there was almost complete overlap of all the eight beams, therefore Gaussian beam distribution was not incorporated in the expressions for the electric fields (Eq. 6-13) of each beam for computation.

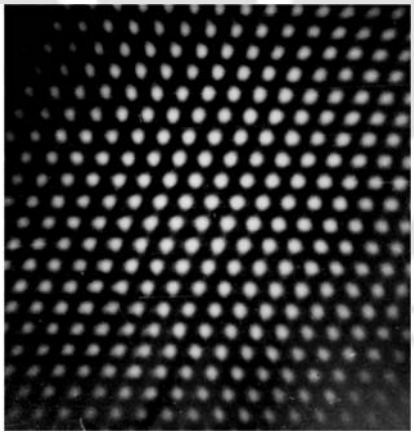

Fig.4.17. Recorded near field hexagonal array pattern on photographic film

The intensity distribution curve along the x-axis was plotted in fig.4.19 for the array pattern of hexagonal geometry. The fringe visibility curve of the same is shown in the fig.4.20. This curve confirms the generation of large no. of tiny light spots in hexagonal geometry with good contrast.

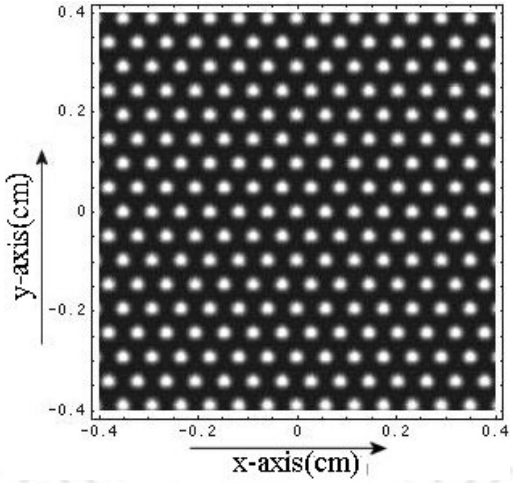

Fig.4.18. Computed near field hexagonal array pattern

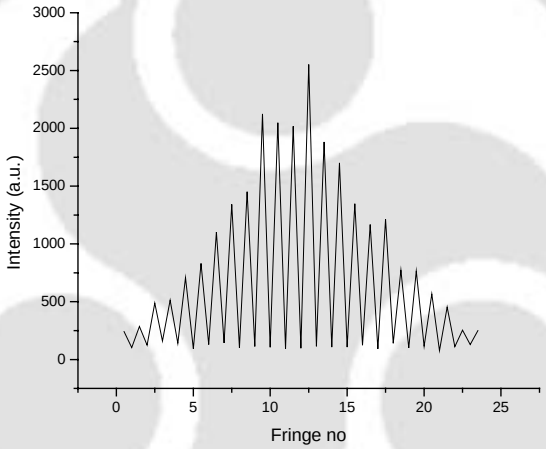

Fig.4.19. Intensity curve along x-axis for hexagonal array.

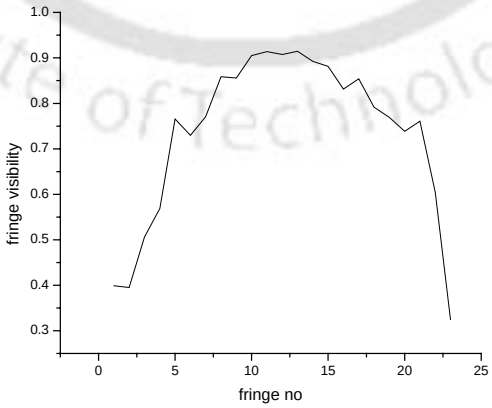

Fig.4.20. Fringe visibility curve along x-axis for hexagonal array.

The hexagonal array was also scanned upto a distance of 2.5 meter without observing any significant distortion and loss of contrast. The far field pattern imaged onto photographic film is shown in fig.4.21. The corresponding computed pattern from Eq.(14), including the Gaussian distribution as expressed in Eq.(6)-(13) is shown in fig.4.22.

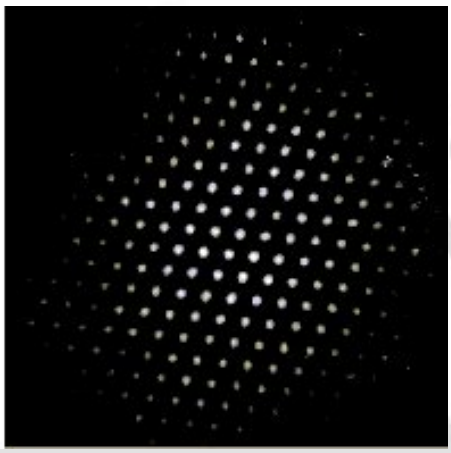

Fig.4.21. Far field pattern at a distance of 2.5m hexagonal recorded on photographic film

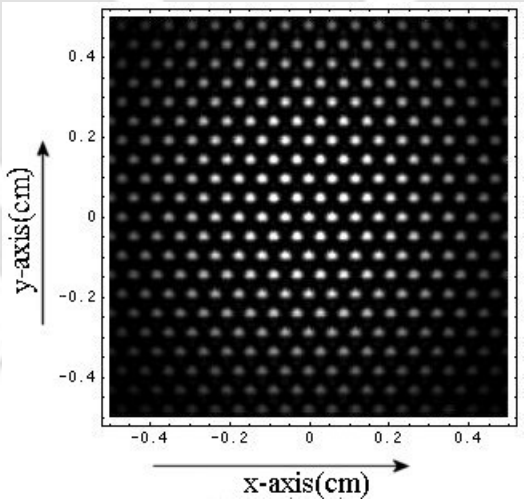

Fig.4.22. Far field computed pattern at a distance of 2.5m for hexagonal arrays.

The recorded compressed pattern using an achromatic lens of focal length 25 cm. is shown in fig. 4.23. The recorded spot density in this pattern is also 900 spots/mm^2. Whenever there was a little mismatch in the frequencies of the individual interference pattern of eight beams, the beating phenomena was observed. One such recorded near

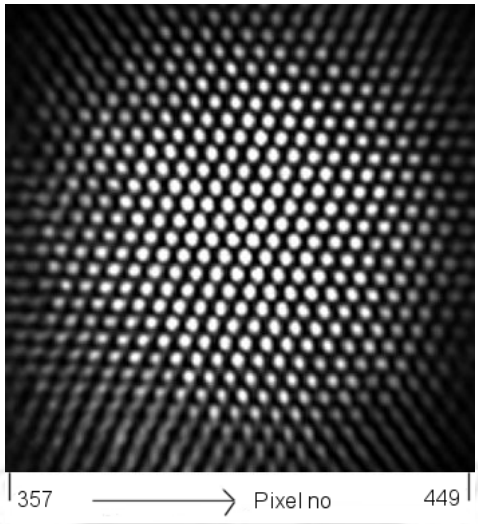

Fig.4.23. Compressed Pattern for hexagonal arrays.

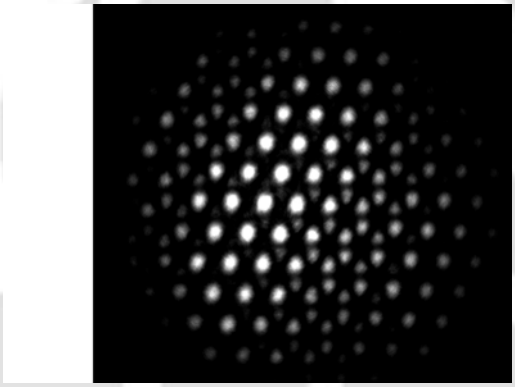

Fig.4.24. Beating phenomenon due to small mismatch in frequencies for individual pattern recorded onto CCD

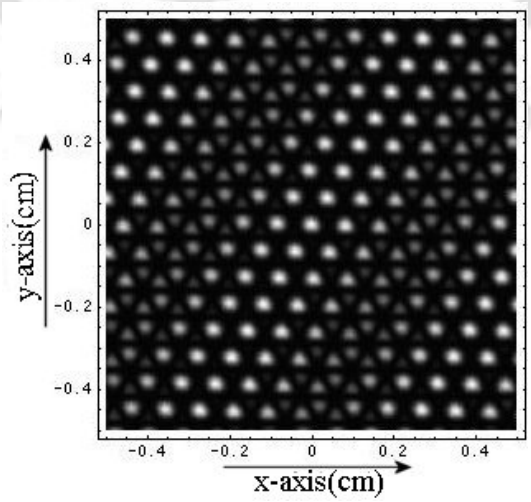

Fig.4.25. **C**omputed beating phenomenon.

field pattern is shown in fig.4.24. The measured values for θ_1, θ_2, θ_3 and ϕ_2, ϕ_3 were 0.98 mrad, 0.98 mrad, 0.85 mrad and 60^0 and 60^0 respectively. The corresponding computed pattern is shown in fig.4.25.

4.4. Light coupling efficiency

For the light coupling efficiency, the input laser power was measured before BS1 of fig.2.3 and 2.4 and the output power was measured before CCD. The ratio of the output power to the input power was 0.217 and 0.087 for four beam and eight beam interference respectively.

4.5. Conclusion

To conclude, we have successfully generated the arrays of large no. of tiny light spots in square, rectangular and hexagonal geometry with high contrast. All the three geometry of the arrays can be also produced in a single experiment setup of fig.2.4. This eight beam interferometric setup can be brought down to a four-beam interference by blocking the mirror M6 (or M5) or by changing the position of detector from the output of BS4 to the output of BS3 and the square arrays can be obtained. The array patterns were observed to be delocalized upto a couple of meters from the output of final stage of the beam splitter. The spot density could be recorded more than 900 spots/mm^2. The perfect matching of the recorded pattern and the computed pattern confirmed the derivation of chapter 3. Therefore with the motorized controlled mirror mounts, one can generate the arrays with predetermined spatial frequencies.

Chapter 5

Results of interference of multiple polarized beams

Due to the poor light efficiency in the randomly polarized beam interferometer, we have developed the interferometers using the polarized beams. The heterodyne interferometers using polarized light have various applications[94-100]. The common method to realize phase shift in an optical beam is by physically changing the optical path either by translating mirrors or optical surfaces in the beam with a piezo-electric transducer or by introducing a tilted glass plate in the path of the one of the beam[92] in a controlled way. With one or more rotating polarizing components viz; polarizer, quarter wave plate or half wave plate, phase shift can also be observed[93-96]. The change in phase difference between the interfering beams produces the modification in interferogram. This phenomenon is useful in phase shifting interferometry[94], designing of a tunable interferometric filter[97], measurement of the birefringent parameters[98], fabrication of three dimensional periodic microstructures[99] and photonic crystals[100]. However, systematic studies on the interference pattern of mutually orthogonal polarized light as a function of azimuth of quarter wave plate (QWP) and polarizer used in such interferometers is not reported. The formation of two-dimensional arrays using polarized setup was reported theoretically[80] in 1997. The experimental demonstrations as well as theoretical analyses were reported by us for the first time[101]. Apart from

improving the light efficiency of the interferometer, the polarized setups were also shown high sensitivity towards the orientations of the various components. The interference pattern of the two pairs of orthogonally polarized beams (four polarized beams) results in fringe free pattern. The pattern can be observed with a polarizer placed in the output plane of the interferometer as it introduces an additional relative phase shift between the two orthogonal polarized light[91].

In this chapter, results of the two orthogonally polarized light and two pair of orthogonally polarized light using setup of fig.2.5 and 2.6 respectively are discussed. The effect of relative ellipticity of the beams on to the quality of the fringes is also studied and compared with the theoretical derivations of chapter 3.

5.1. Two beam interferometers

The experimental set up used to study of interference of two polarized beam is shown in fig.2.5. The interference pattern of the two interfering polarized beams at the output plane is completely dependent on the orientation of the polarizing components. The intensity distribution of the pattern changes due to the change of orientations of polarizers and QWPs. The interferograms were recorded and the fringe quality was studied as a function of orientations of Q_2, Q_3 and phase shift was studied for different orientation of P_2. The orientation of the P_2 introduces the relative phase shift in the two orthogonal polarized beams after Q_3. The orientation of Q_2 finally results into the changes in the intensity of the beam coming out from that particular arm of the interferometer. The orientation of Q_3 controls the relative ellipticity of the two beams.

5.1.1. Phase shift due to change of azimuth of analyzer

To realize the phase shift due to change of azimuth of analyzer at the output plane the

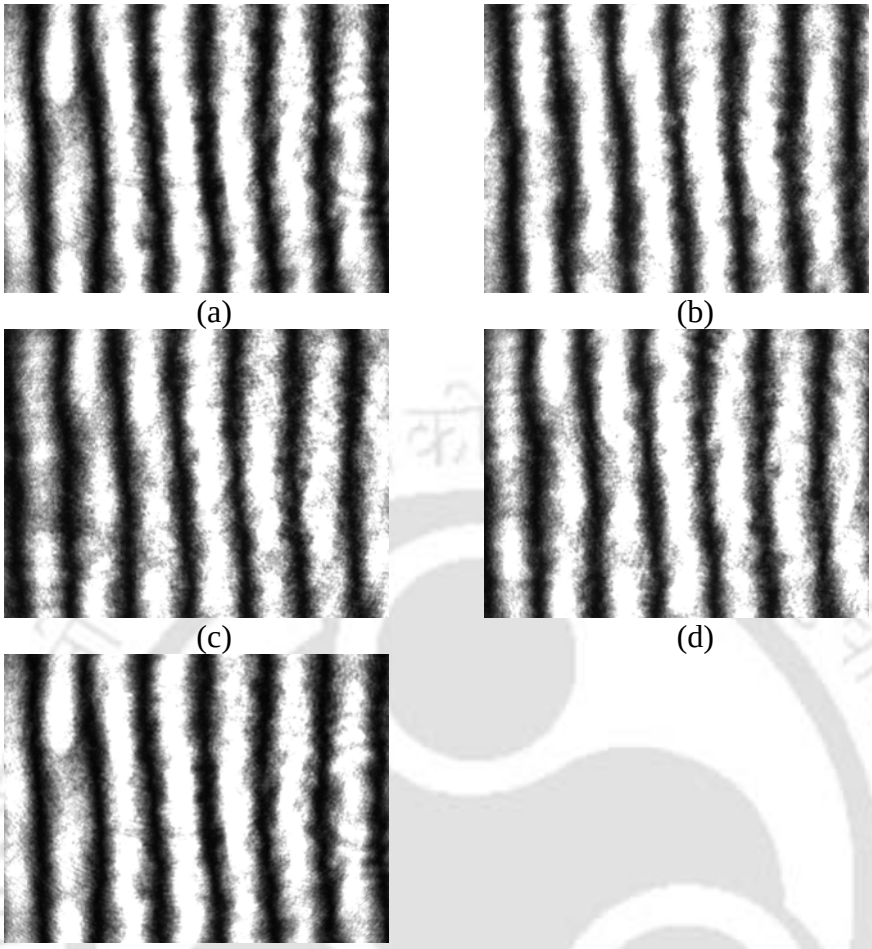

Fig.5.1. Interference pattern recorded onto CCD for θ = a) 0^0, b) 45^0, c) 90^0, d)135^0, e)180^0

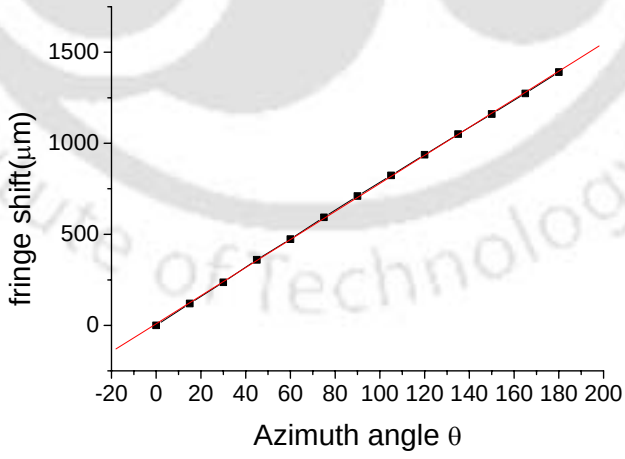

Fig.5.2. Fringe shift due to the change of azimuth of analyzer

QWP Q_2 and Q_3 were aligned at 45^0 with respect to polarization plane of the incident beam on the respective QWP and the analyzer (P_2) was rotated (θ). The interference pattern recorded for $\theta = 0^0, 45^0, 90^0, 135^0, 180^0$ onto CCD is shown in the fig.5.1. (a), (b), (c), (d), (e) respectively. From fig.5.1 it is clearly observed that 180^0 rotation of the analyzer gives one fringe shift confirming an additional phase difference of 2π developed between the two interfering orthogonal beams. The plot of measured fringe shift versus the azimuth of analyzer (θ) is shown in fig.5.2 confirming the linearity of phase shift θ (Eq. 20 in chapter 3).

5.1.2. Fringe visibility due to the change of orientation of Q_2.

To study the fringe visibility due to the relative change of intensity of the interfering beams, Q_3 and P_2 were aligned at 45^0 and Q_2 was rotated and the interference pattern were recorded for ρ_1 at 0^0, 15^0, 30^0, 45^0, 60^0 and 75^0 onto CCD. The recorded CCD patterns are shown in fig.5.3 (a), (b), (c), (d), (e) and (f) respectively. The intensity distribution of the patterns was scanned and the fringe visibility was measured as a function of ρ_1. The fringe visibility was also computed from the expressions of intensity (from Eq. 21, 22). The experimental and theoretical fringe visibility curves as a function of ρ_1 are shown in fig.5.4. The general behaviour of the fringe visibility for the experimental and theoretical results matches. The little mismatch can be attributed to deviation from normal angle of incidences at various stages.

5.1.3. Fringe visibility due to the relative change in ellipticity of the two beams

To study the fringe visibility due to the change of relative ellipticity of the two beams in the interference pattern, Q_2 and P_2 were aligned at 45^0, Q_3 was oriented and the interference patterns recorded for ρ_2 at 0^0, 15^0, 30^0, 45^0, 60^0 and 75^0 onto CCD are shown in the fig.5.5 (a), (b), (c), (d), (e) and (f) respectively. The fringe visibilities from

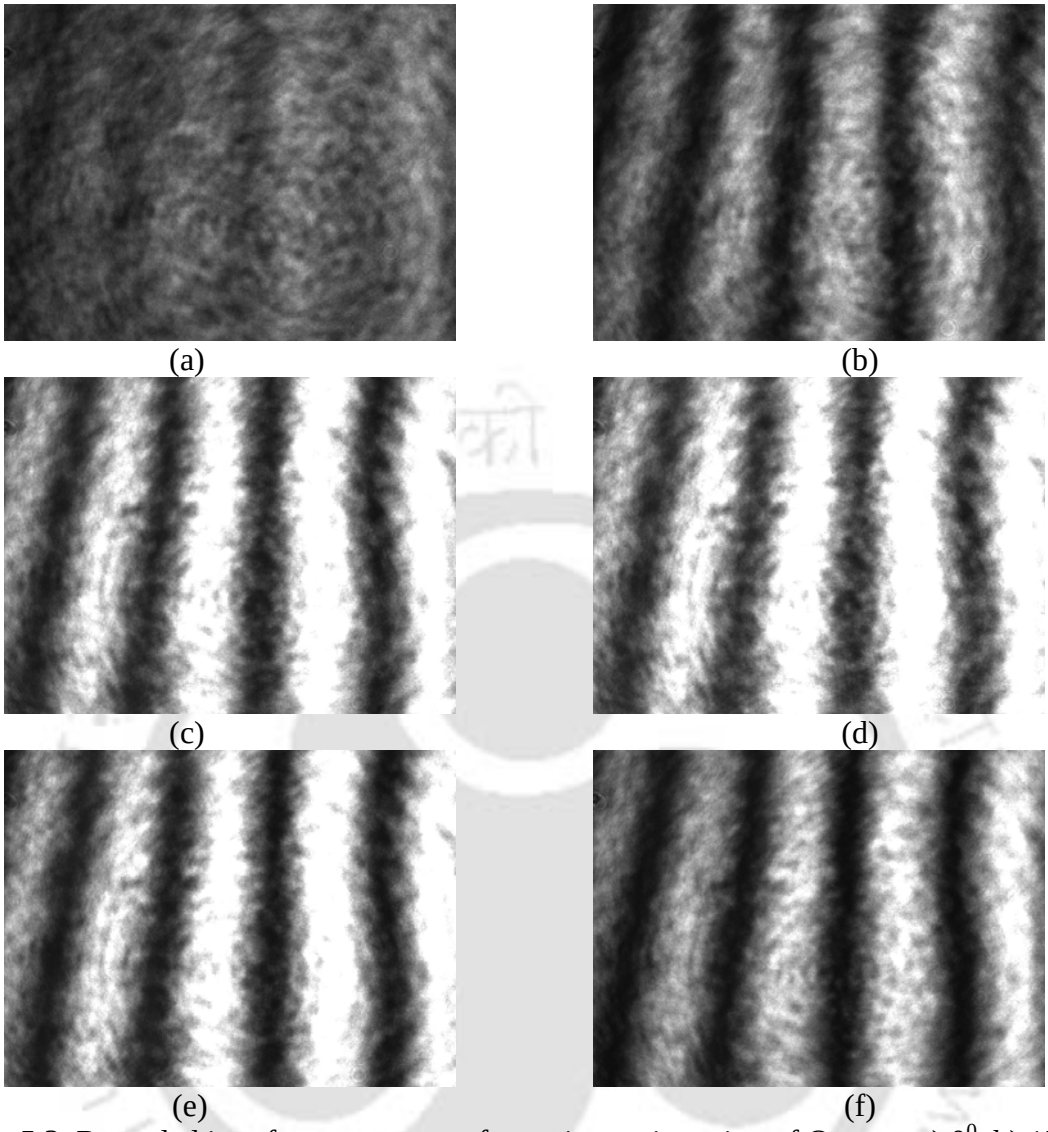

Fig.5.3. Recorded interference patterns for various orientation of Q_2, ρ_1 = a) 0^0, b) 15^0, c) 30^0, d) 45^0, e) 60^0 and f) 75^0

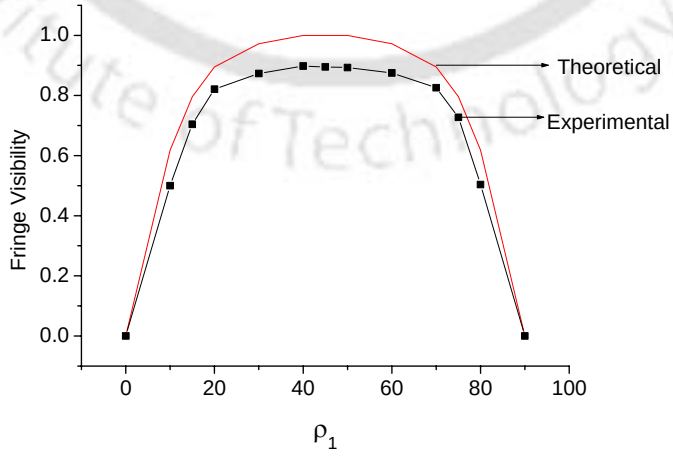

Fig.5.4. Fringe visibility curve

these patterns as a function of ρ_2 is plotted in fig.5.6. The little variation in theoretical and experimental curves of fringe visibility may be attributed to the deviation of the incident beams on the polarized components from the normal incident.

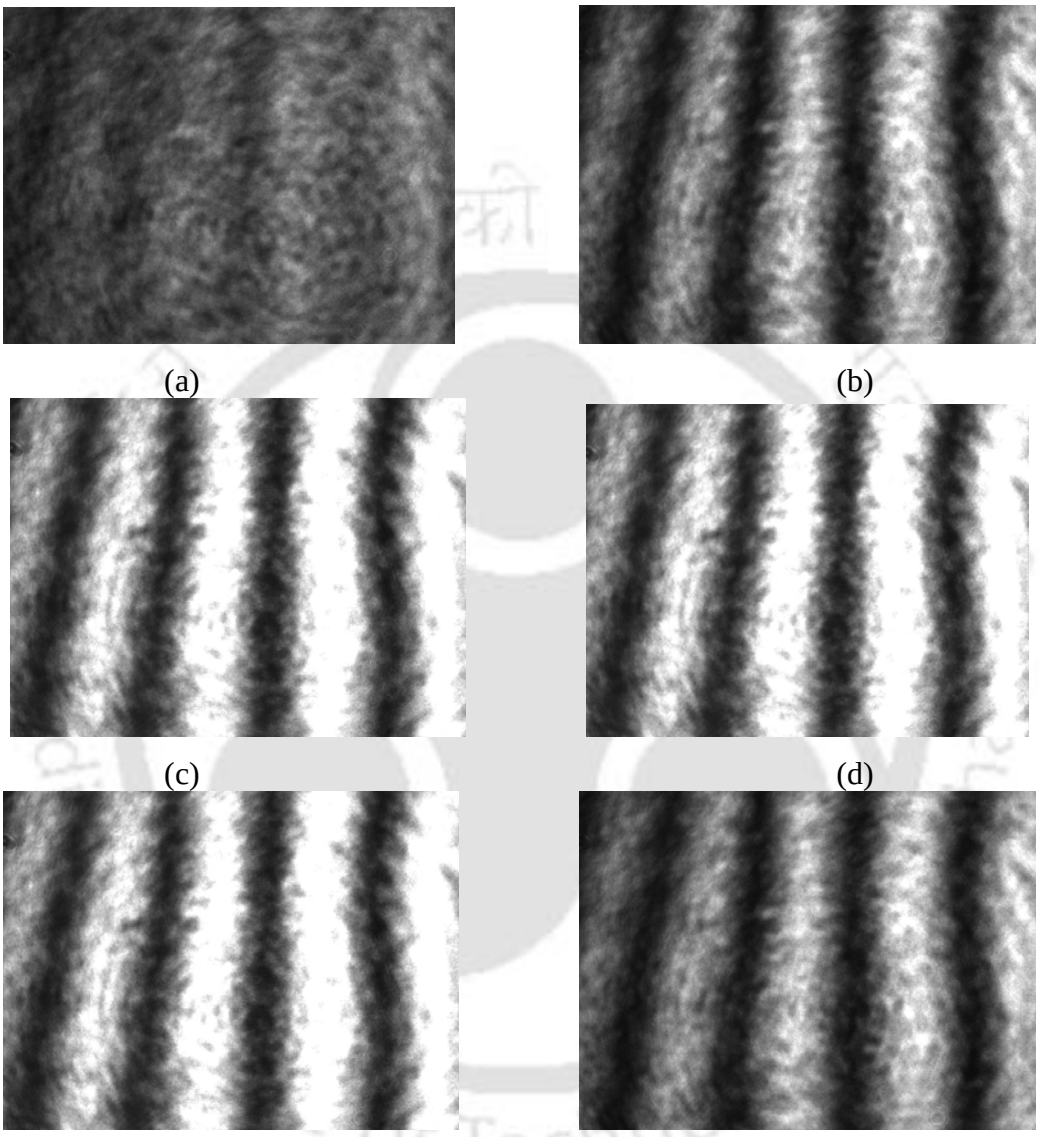

Fig.5.5 Recorded interference patterns for various orientation of Q_3, ρ_2 = a) 0^0, b) 15^0, c) 30^0, d) 45^0, e) 60^0 and f) 75^0

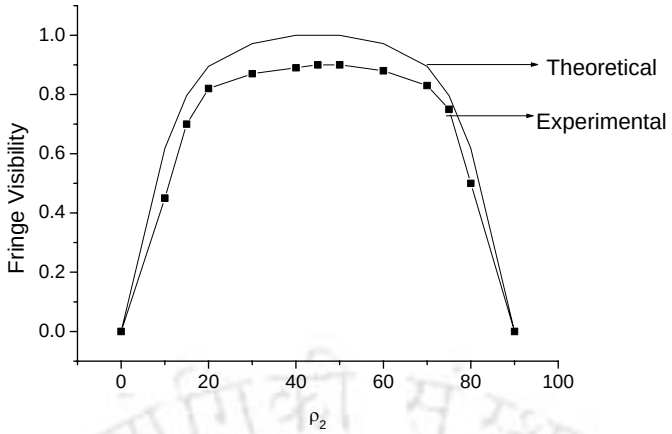

Fig.5.6. Fringe Visibility Curve

5.2. Four polarized beam interferometer

The experimental set up for four polarized beam interferometer is described in fig.2.6. The output of this setup from the PBS2 consists of two pairs of orthogonally polarized light. These polarized lights were converted into two pairs of orthogonally elliptically polarized light and a fringe free pattern was observed. With the polarizer P_2 in the output plane, the interference pattern was observed. The interference pattern of such two pairs of orthogonally polarized beams at the output plane is completely dependent on the orientation of the polarizing components. The intensity distribution of the pattern changes from the first straight parallel line fringes to the square arrays depending on the orientations of polarizers and QWPs. In this set up the interferograms were recorded and studied for the different orientations of Q_2 and Q_3 and P_2 being kept at $\theta = 45°$. As all four beams are at small angular separation and so the patterns is delocalized along the longitudinal direction.

5.2.1. Array generation from the polarized beams

The near field regular square arrays recorded onto CCD is shown in fig.5.7 for $\rho_1 = \rho_2 = 45°$. For these arrays the interferograms from two interferometers were oriented perpendicular to each other and the angular separations were $\theta_1 = \theta_2 = 1.8$ m rad. The

corresponding computed square array pattern (from Eq. 31-34 of chapter 3) is shown in fig.5.8. It matches with the experimental results.

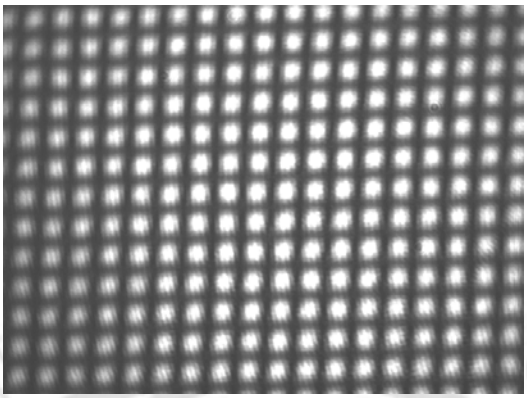

Fig.5.7. Near field square array recorded onto CCD for $\rho_1 = \rho_2 = 45°$.

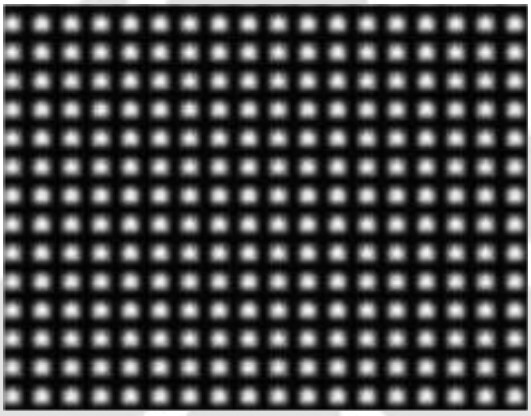

Fig.5.8. Computed pattern with the experimental data.

As the beams were propagating at small angular separation so the interference pattern can be observed for large longitudinal distances. For a beam having beam radius 2w the pattern can be observed up to a longitudinal distance of $2w/\tan\theta_i$. Beyond that gradually the overlap region among the beams will start reducing and hence the size of the pattern and finally all the beams will go apart without any overlap. The arrays were scanned to a distance of 2.5 meter without observing any significant distortion and loss of contrast. Array pattern recorded at a distance of 2.5m is shown in fig.5.9. Far field pattern

computed using Eqs. (31-34) by incorporating the Gaussian distribution is shown in fig.5.10.

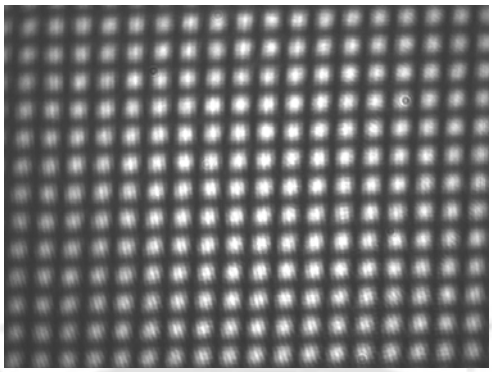

Fig.5.9. Recorded far field pattern for $\rho_1 = \rho_2 = 45°$.

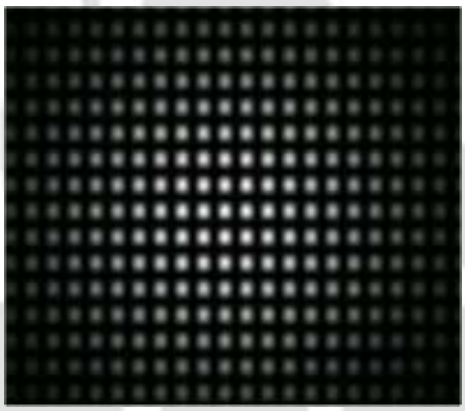

Fig.5.10. Far field computed pattern

5.2.2. Fringe visibility of arrays due to the change of orientation of Q_5

The orientation of Q_5 from 45° results into the unequal intensities of two pairs of the beam and the fringe contrast will be modified. The array patterns recorded for different ρ_1 (directly onto the CCD) is shown in fig.5.11 for ρ_1 = 0°, 15°, 30°, 45°, 60° and 75°. From the CCD images I_{max} and I_{min} were measured and fringe visibility was calculated. The variation of fringe visibility as a function of ρ_1 is shown in fig.5.12.

5.2.3. Fringe visibility due to the change of orientation of Q_6

The orientations of Q_6 (ρ_2) introduces the relative changes in the ellipticity of the two pairs of beams. The recorded array patterns for different ρ_2 are shown in fig.5.13. The

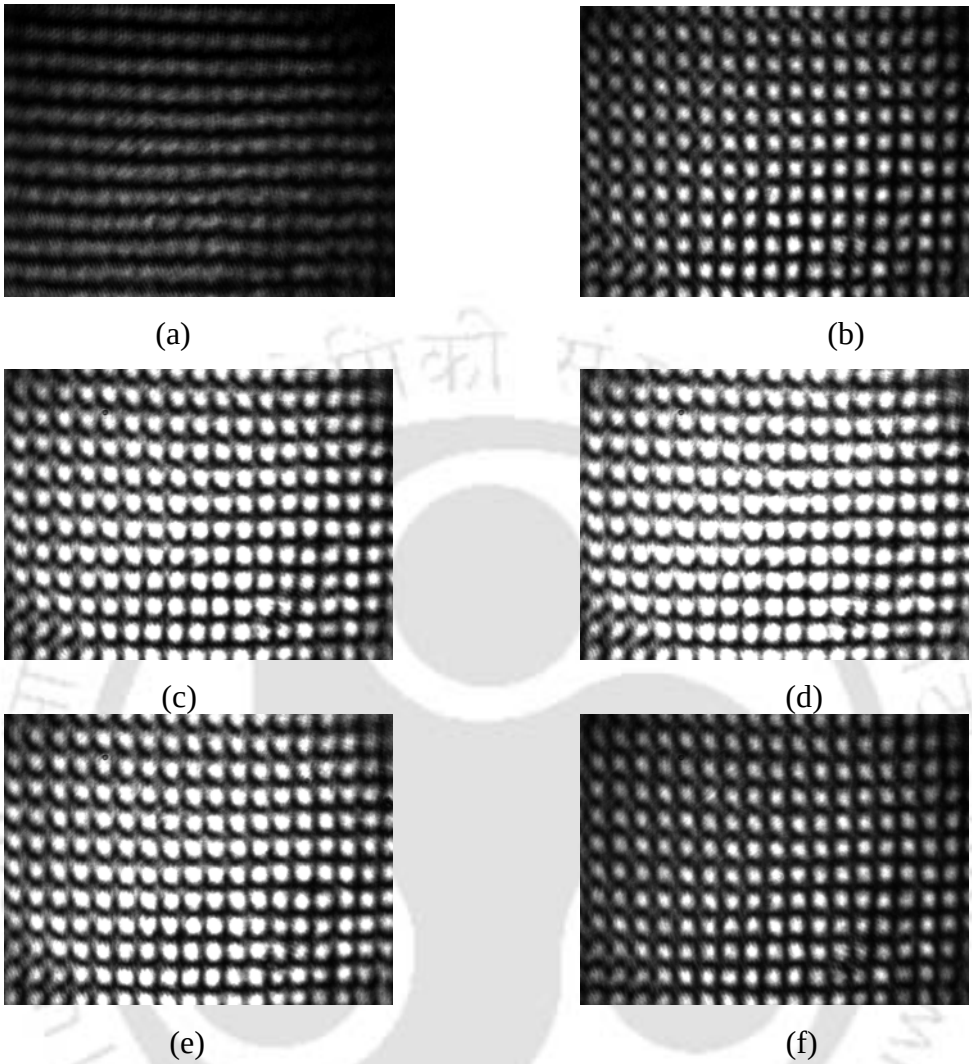

Fig.5.11. Recorded array patterns for the various orientation of Q_5 ($\rho_2 = 45°$), a) $\rho_1 = 0°$ b)$\rho_1 = 15°$ c)$\rho_1 = 30°$ d)$\rho_1 = 45°$ e)$\rho_1 = 60°$ f)$\rho_1 = 75°$.

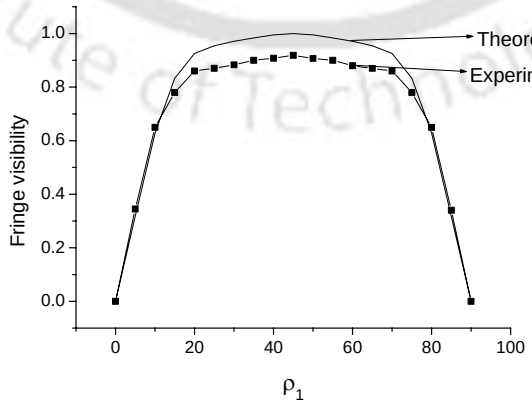

Fig.5.12. Fringe visibility curve as a function of ρ_1 for $\rho_2 = 45°$.

variations of fringe visibility for both theoretically and experimentally as a function of ρ_2 are shown in fig.5.14. The experimental and theoretical behaviours are in good agreement. The small differences in the magnitude of the theoretical and experimentally measured values of fringe visibility could be because of little deviation from the normal incidences on the QWP's and polarizer.

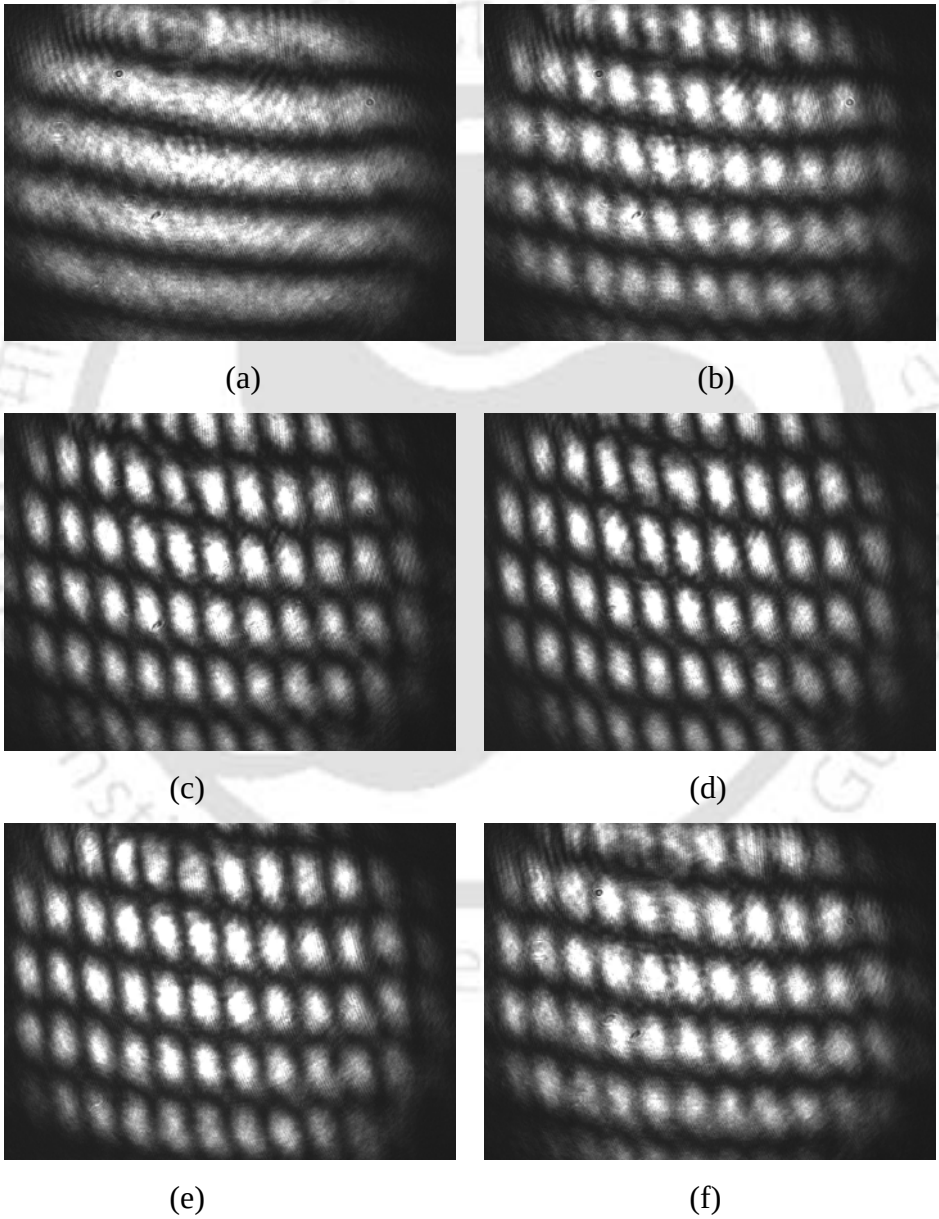

Fig.5.13. Recorded array patterns for the various orientation of Q_6 ($\rho_1 = 45°$), a) $\rho_2 = 0°$ b) $\rho_2 = 15°$ c) $\rho_2 = 30°$ d) $\rho_2 = 45°$ e) $\rho_2 = 60°$ f) $\rho_2 = 75°$.

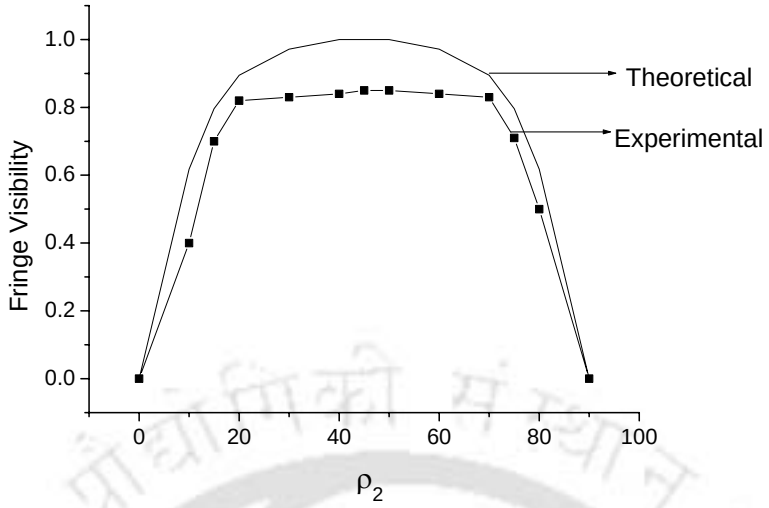

Fig.5.14. Fringe visibility curve as a function of ρ_2 for $\rho_1 = 45°$.

5.3. Light coupling efficiency of arrays from polarized setup

For the light coupling efficiency, the input laser power to the interferometer was measured after collimator and the output power was measured after P_2. The ratio of the output power to the input power was 0.443. In comparison with the four beam interferometers of randomly polarized setup the efficiency of polarized setup is ~ 2 times more.

5.4. Conclusions

Non observable fringes of two polarized beams are observed with the help of a polarizer placed in the output of an interferometer similar to Michelson interferometer with polarized beam splitter, mirrors and QWPs. We have experimentally observed the phase shift between the two orthogonal interfering beams as a function of azimuth of polarizer at the output plane. The interference pattern and the fringe visibility have been studied as a function of relative state of polarization of the two interfering beams using same setup. The square arrays were generated with polarizing components using two pairs of polarized beams. The quality of the fringes was observed to be dependent as the

relative intensity as well as relative ellipticity of the two pairs of polarized light (four polarized beams). The interference pattern was observed without any significant loss of quality up to large longitudinal distances confirming the formation of delocalized polarized arrays. The computed pattern shows a good agreement with experimental results. Experimentally measured fringe visibility as a function of orientation of QWP in the output of the interferometer shows good agreement with the theoretically computed values.

Chapter 6

Applications of interferometric arrays

After successfully developing and analyzing the various interferometric configurations for array illuminator, the setup was tested for their applications towards a) lithography for the formation of the periodic structures via selective laser ablation and b) diagnostic for pulsed plasma system. In addition to this, some several possible applications of these interferometric arrays are proposed in this chapter.

6.1. Lithography Techniques

a. Laser beam writing lithography

A continuous surface relief grating for the two dimensional array generation has been realized by laser beam lithography[102, 103]. In this scheme, the resist coated substrate is mounted on the precession translation stage and scanned under modulated focused laser beam. The development of the resist results in the micro relief of the desired structure.

b. Electron beam lithography

Electron beam lithography (EBL) is being used for creating extremely fine patterns (sub micron patterns, 0.1μ m and below) for integrated circuits. This technique consists of scanning a beam of electrons across a surface covered with a resist film sensitive to the electrons falling on it, thus depositing energy in the desired pattern in the resist film[104]. Ekberg et al.[105] have reported two dimensional multilevel grating array generators.

c. Atom Lithography using dipole force

Atom lithography using dipole force[24, 25] is another upcoming scheme to generate the periodic structure of the order of tens of nanometer. In this scheme, atoms undergoes a dipole force which originates from the interaction of the induced dipole moment with near resonant, non-uniform light field. With the proper choice of the parameters, the trajectories of atoms under this force can be modified to focus the atomic beam at nanometer scale.

d. Selective ablation via high power laser interferometer

We have developed a new single step lithography technique using multiple beam interferometers, without any mask. This technique is based on modifying the surface morphology to the order of tens of nanometer sizes by selective ablation of material using laser. This may find application in the fabrication of optocoupler[88], laser arrays[106] and other optoelectronic devices[107, 108]. The technique is very general and is applicable to any kind of material. In this technique, thin films of metals, semiconductors, polymers or any other complex compound can be ablated selectively by illuminating it with interference pattern formed by high power laser. This results in the ablation of materials in the region of maximum intensity (bright fringe) leaving the area of minimum intensity (dark fringe) unaffected. The periodicity of the grating so formed will depend on the spatial frequency of the interference pattern. The width of the lines depends on the laser intensity and damage threshold of the material of the thin film. This can be explained with the help of fig.6.1 and fig.6.2. Fig.6.1 is a typical interferogram from a Michelson interferometer recorded onto a CCD camera. The intensity distribution of this interference pattern is shown in fig.6.2 with the line marked for the damage threshold. From the figure it is clear that the thin film exposed

to the intensities above the damage threshold will be ablated leaving behind the rest of the material unaffected and thus by changing the intensity of the laser the writing width can be controlled. Using this technique one can write the periodic structures as grating or two dimensional arrays of tiny spots in a single step with the advantage of having online control on the configuration of micro-nano structures simply by modifying the interference pattern.

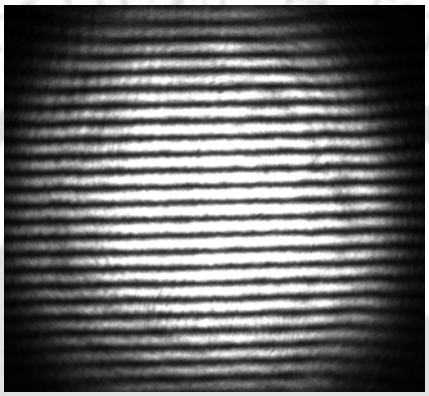

Fig.6.1. Interference pattern from Michelson interferometer

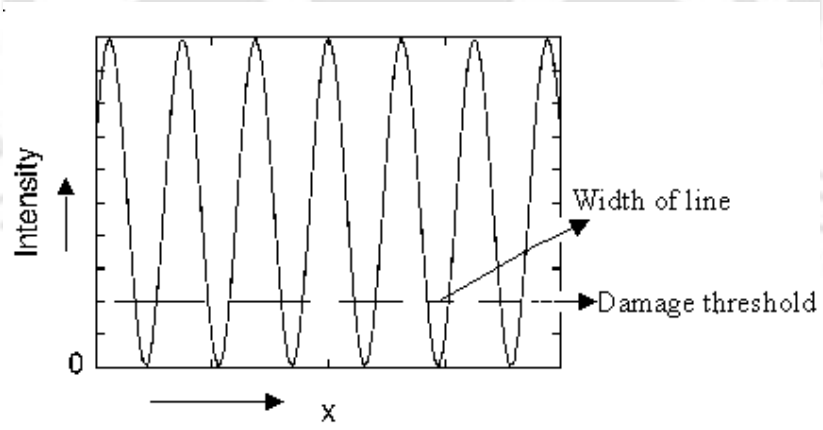

Fig.6.2 Intensity distribution in the interference pattern

6.2. Results of selective laser ablation

For the selective laser ablation, two beam and four beam interferometers were assembled using the 2nd harmonic of Q switched Nd:YAG laser (HYL101-Quanta System) as shown in fig.2.7 and fig.2.8 respectively. The thin films were illuminated by

the interference patterns in air. Thin films of Indium were deposited on the glass substrate using thermal evaporation coating unit. The region of the thin film receiving the bright spots was ablated leaving behind the region of dark fringe unaffected.

6.2.1. Two beam interferometer for 1-D grating

The experimental setup used to write lines on the Indium thin films is shown in fig.2.7. The selectively ablated region of this film was scanned with the micrograph. The micrograph shown in fig.6.3 confirms the writing of large no. of lines of Indium of periodicity 1 μm in a single shot.

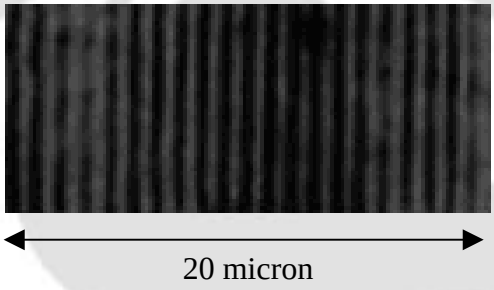

Fig.6.3. Micrograph of selectively ablated indium thin film for grating

6.2.2. Four beam interferometers for two dimensional arrays

The experimental setup was used for two dimensional arrays on the Indium thin film is shown in fig.2.8. A large number of holes in a square matrix were punctured using this technique. The micrograph of these holes is shown in fig.6.4 confirms the formation of matrix of holes in square geometry having periodicity ~ 20μm, and hole diameter ~ 10μm. As the Nd:YAG laser was not delivering perfect TEM_{00} mode, therefore there is some non-uniformity observed in the formation of grating as well as in holes.

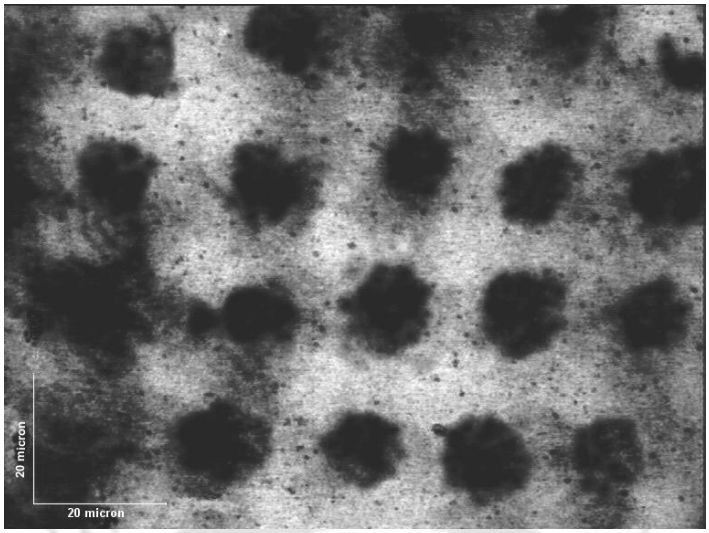

Fig.6.4. Micrograph of the ablated matrix of holes

6.3. Measurement of electron density

We have developed the two beam interferometric setup for the measurement of electron density profile in a spark gap. The circuit used for the air breakdown in the spark gap is shown in fig.2.9. The current through spark gap was measured by measuring the voltage drop across a low resistance of 0.324 Ω. Fig.6.5a. shows the voltage drop across the low resistance corresponding to a peak current of 2.7kA and the pulse duration of 32μs. The high voltage applied between the two electrodes was measured through a high voltage probe. The voltage pulse from DSO is shown in fig.6.5b. The measured peak applied voltage (fig.6.5b) is around 12 KV. The recorded photodiode signal from the beam deflection set-up of fig.2.12 is shown in fig.6.5c. This corresponds to plasma duration (the dip in the photodiode signal) of ~ 4.3ms.

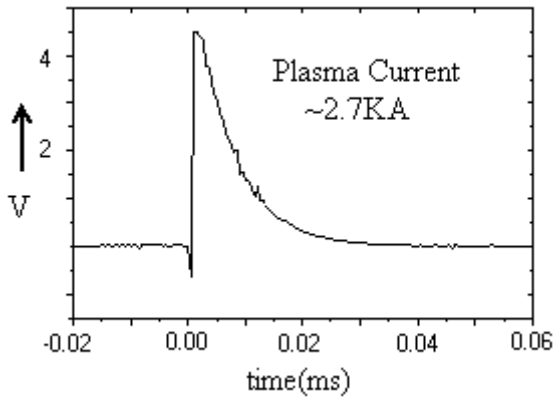

a.

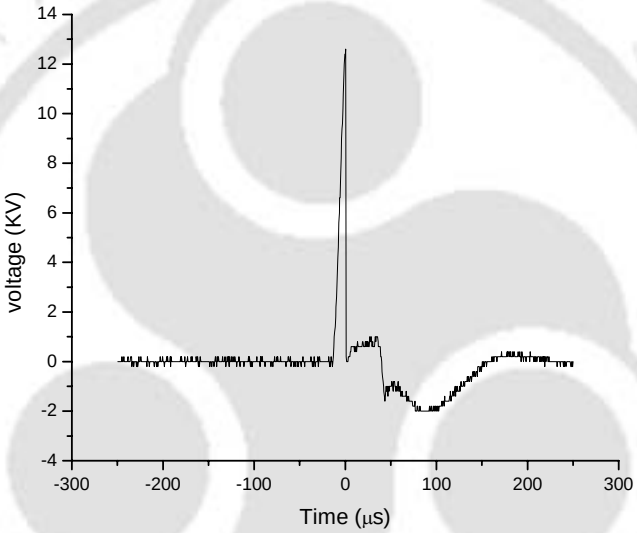

(b)

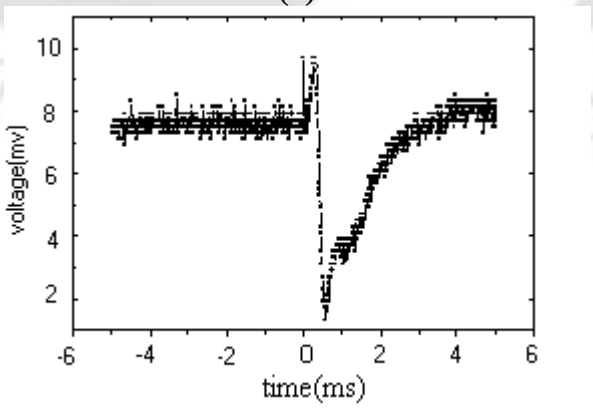

c.

Fig.6.5.a. The voltage drop across 50 ohm terminator corresponding to the Plasma current pulse (peak current ~2.7KA), b.voltage pulse through high voltage probe, c. Signal from beam deflection set-up,

Interferogram recorded in presence of plasma for vertical fringes (fringes perpendicular to the electrodes axis) and horizontal fringes (fringes parallel to the electrodes axis) are shown in fig.6.6a and 6.6b respectively. Distortion into the fringes in the region of the plasma is very obvious in both the interferograms. Wherever the electron density is maximum the deviation of the fringes are also maximum. The line integrated electron density profile is estimated by measuring the deviation of the fringes (Eq. 47-49).

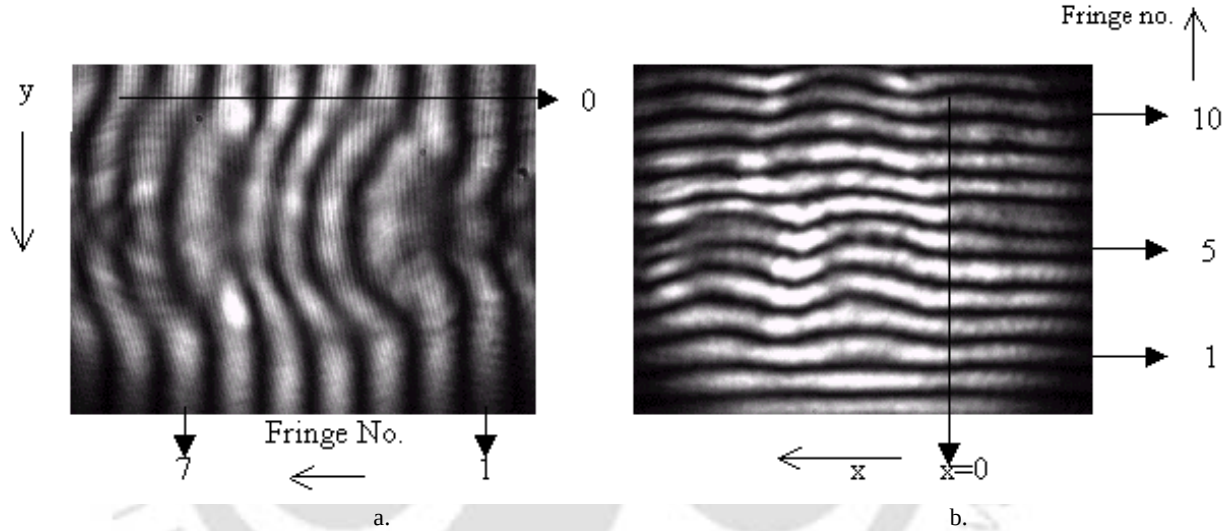

Fig.6.6. Interferograms (a) vertical fringes, (b) horizontal fringes

The line integrated electron density profiles perpendicular to (Y-axis)as well as parallel to (X-axis) the electrode axis are shown in fig.6.7 and fig.6.8 respectively, corresponding to the interferogram of fig.6.6a and 6.6b respectively. The axis and the origin of plot of fig.6.7 and fig.6.8 are labeled clearly in respective interferograms (axis are shown in fig.2.11.). The electron density measured in the spark gap of the present set-up is in the range of around 10^{17} cm^{-3}. Fig.6.7. shows the electron density profile perpendicular to the axis of electrodes as analyzed from the interferogram of fig.6.6a. Electron density is maximum in the region of the line joining the two electrodes.

Fig.6.8. shows the horizontal electron density profile (along x-axis, the electrodes axis) measured from the interferogram of fig.6.6b. It clearly reflects the formation of two high-density lobs well separated around the location of the electrodes and in the middle of the electrodes the density is minimum. This is not a surprising result as around the electrodes the electric fields are higher and so the electron density[116] is large. This is also well reflected in both the interferograms of fig.6.6.

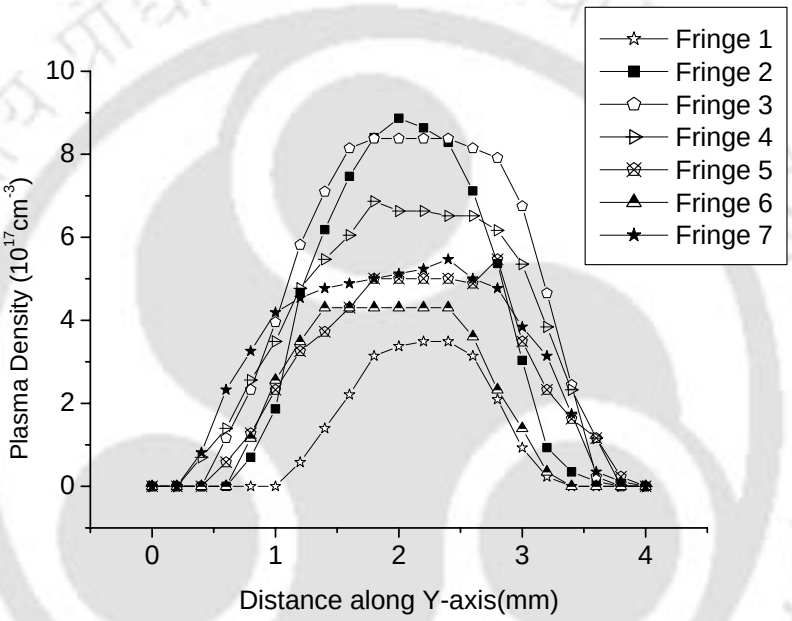

Fig.6.7. Vertical Plasma Density profile.

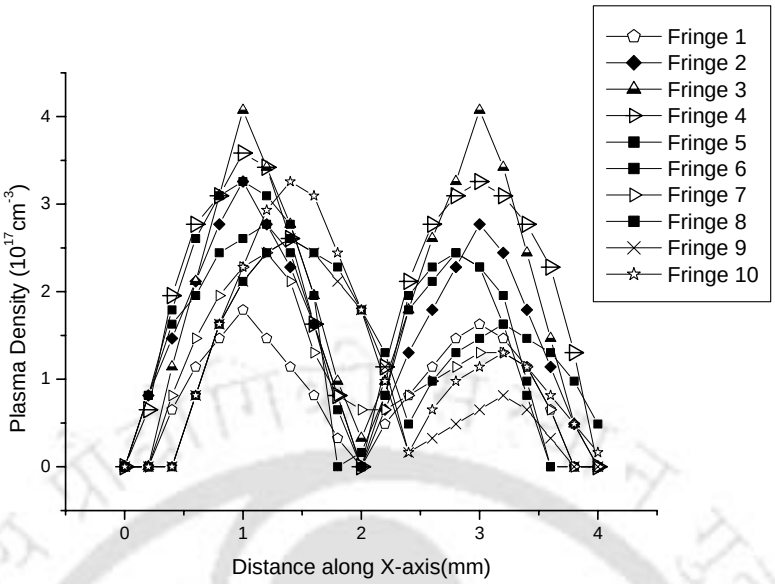

Fig.6.8. Horizontal Plasma density profile.

6.4. Several possible applications

Some of the possible applications of the interferometric arrays generated and studied in the present thesis are proposed below for future applications.

Along the longitudinal direction the interferometric arrays propagates in the form of optical channels. If a nonlinear medium with an intensity dependent non-linear refractive index is placed in the path of the arrays, an array of light channels will be established in the medium. The intensity variation at any transverse plane is given by Eq. (14) and these optical channels in the medium will behave like a light induced graded-index polarization dependent optical planar waveguide. The state of polarization within the spots of arrays can be changed from linearly polarized light to circularly polarized light. Hence this set up may be applied in polarization optical switching.

These interferometric array illuminators offer non uniform periodic light intensity distribution, whose spot densities and width can be varied in real time that gives some

possible application in modifying the trajectories of the atoms. If an atom is placed in such non uniform optical field, it experiences two kinds of forces[109]. The radiation pressure force results from absorption, followed by random spontaneous emission of photons. This dissipative spontaneous force is responsible for laser cooling[110]. The field will also induce a dipole moment into the atom placed into it. Due to interaction of this induced dipole moment with non uniform light distribution the dipole force is generated[109]. The magnitude of this force depends on the intensity gradient and the amount of detuning from the atomic resonance frequency. This dipole force can modify the trajectories of atoms and with the careful choice of the parameters it can lead to focused spots of atoms of the order of tens of nanometers[111] having periodicity down to $\lambda/8$.[112] the interference fringes[113] have been used for the alignment and manipulation with optical tweezers of low-index spheres.

The interference of the polarized beams can also be used to generate the periodic microstructures. Thus AIL can be used to write down in a single shot the three dimensional photonic crystal[114]. By controlling the relative polarization of four interfering beams and their angular separations, the periodicity and the line width can be controlled. Therefore the band gap of such engineered materials can be controlled. By changing the geometry and spatial frequencies of AIL periodic multiple structures can also be generated which provides the further fine tuning on to the band gap. These photonic band gap materials have promising application in fabricating optical waveguide, high capacity data storage devices and other related areas. The fringe visibility curve can be used in online optical testing.

6.5. Conclusions

We have developed a single step single shot lithographic technique using multiple beams interferometers, without any mask. With two beam interferometer large numbers of parallel thin lines of indium were formed. We could able to write the indium lines of periodicity 1 μm. In order to maintain the uniformity of the lines and to reduce the line width the laser power and angles between the interferometric beams have to be controlled. With the four-beam interferometer large number of holes of the order of 10 μm in the square matrix format was imprinted on the thin film.

The line integrated electron density profile of pulsed plasma was measured with the help of interferometric technique. Several possible applications of interferometric array illuminators; in light induced graded index optical channel, atomic beam channel, polarization switching, optical tweezers and photonic band gap crystals are proposed.

Chapter 7

Conclusions

We have developed two and three interferometers in tandem for the generation of square, rectangular and hexagonal arrays of tiny light spots with good contrast. Two interferometers in tandem were assembled for the generation of square and rectangular arrays of tiny light spots. The setup was illuminated with a collimated randomly polarized He-Ne laser beam. This setup results into the four nearly collinear beams. Square arrays were observed when the x and y spatial frequencies were equal ($\mu = \nu$) and rectangular arrays were resulted for the unequal spatial frequencies. The hexagonal arrays were produced using interference of eight beams. Eight coherent beams were generated using one Mach-Zehnder and two Michelson interferometers in tandem. Whenever the magnitude of spatial frequencies of each interferogram from the individual stages were exactly the same and individual patterns were oriented at 60^0 with respect to each other, the resultant interference pattern was of regular hexagonal geometry. The beating phenomenon was observed due to little mismatch in spatial frequencies of the individual interferograms in eight beam interference pattern. The geometry and size of these arrays can be controlled by the mirror's tilt. The square, rectangular, hexagonal arrays and beating phenomenon were recorded onto CCD. From the recorded CCD patterns, the intensity distributions of all the arrays were scanned. The fringe visibility was measured from the intensity curve. It is confirmed from the

fringe visibility curve that large number of spots can be generated with good contrast in square, rectangular and hexagonal geometry. We could obtain more than 2500 tiny spots of light with high contrast. The array patterns were compressed with the help of a lens and maximum spot density around 1000 spots/mm^2 was recorded onto CCD. The light coupling efficiency observed was 0.217 and 0.087 for four beam and eight beam interferometers respectively.

Only limitation of the above setup with randomly polarized light is its low light efficiency. To improve upon the light efficiency, we have proposed and developed the heterodyne interferometer for two and four beams using polarized light. The Experimental setup for two polarized beam was assembled using polarizing components with an arrangement similar to a Michelson interferometer. A collimated beam was passed through polarizer and launched into the interferometer, which consists of one polarizing beam splitter, two quarter wave plates, one in each arm and two mirrors. The output of this interferometer results into two orthogonally polarized beams. These beams were passed through one quarter wave plate to convert into circularly or elliptically polarized light. The interference patterns of these beams are non observable. The fringes were recorded with the help of polarizer. In the above configurations, an additional phase difference can be introduced between the two orthogonally polarized beams as a function of azimuth angle of polarizer in the output plane, without effecting the arms of interferometer. This additional phase shift modifies the interferogram in terms of fringe shift and is recorded onto CCD. Fringe shift goes linearly with the azimuth of the analyzer.

The Experimental set up for four beam interference with the help of polarizing components was also developed to produce polarized two-dimensional arrays. This

setup consists of two interferometers similar to two beam polarized setup in tandem that results into two sets of orthogonally polarized beams at the output plane. The ellipticity of the interfering beams from the polarized interferometric setup can be controlled with the orientation of the quarter wave plate in the output plane as well as in one of the arm of the interferometer. Accordingly the fringe contrast will also undergo changes. The interference patterns were recorded by changing the azimuth of the quarter wave plate in the output plane as well as in one of the arm of the interferometer for both, two beams and four beams polarized interferometric setup onto CCD. The fringe visibilities were measured for all the patterns as a function of azimuth angle of the quarter wave plates from the recorded interferograms. Light coupling efficiency for this setup was measured to be 0.443, which is almost double compare to the randomly polarized four beam interferometer for the generation of square/ rectangular arrays.

The interference patterns from all the interferometric configurations were scanned to a distance of ~3.0 meter without observing any significant distortion and loss of contrast along the longitudinal direction of beams confirming delocalization of the patterns along the axial direction. Hence the arrays can be transported to a large distances and can be compressed without distortion with a lens to achieve large spot areal density. The expressions for the resultant intensity distribution in the output plane for all the interferometric configurations developed were worked out in terms of various controlling parameters of the optical components used in the experimental setup. The expressions for the resultant intensity distribution for all the interferometric configurations were computed for the array patterns and for the fringe visibilities. The computed results show good agreement with the experimental data. Therefore, a

computer controlled motorized mounts can be used to generate the two-dimensional arrays of equal illuminating tiny light spots in a programmable manner.

The observations of beating phenomenon in hexagonal array pattern from eight beam interference may prove to be a sensitive tool for analyzes of wavefront distortion in addition to a technique for producing arrays of tiny light spots in complex geometry. For this, sample can be placed in one of the arms of any interferometric stage. It will affect the wave front of four beams of the setup and hence give the beating phenomenon. From the measurement of beating frequency the wave front distribution can be measured.

After successfully developing and analyzing the various interferometric configurations for array illuminator, the setup was tested for their applications towards a) lithography for the formation of periodic structures via selective laser ablation and b) diagnostic for pulsed plasma system. For the selective laser ablation, two beam and four beam interferometers were assembled using the 2^{nd} harmonic of Q switched, high power Nd:YAG laser. The thin films of Indium were illuminated by the interference patterns. The region of the thin film receiving the bright fringe was ablated leaving behind the region of dark fringe unaffected. With the two beams large numbers of parallel thin lines of Indium were formed and with the four beams large number of holes in the square matrix format could be drilled in the thin film. The periodicity of the grating thus formed was controlled by a focusing lens placed in the output of the interferometer before the thin film. The selectively ablated regions of the Indium thin film were scanned with micrograph and confirmed the formation of ordered arrays of periodicity down to 1 micron in a single step without using any mask. This also

confirms that array pattern generated in our setup can be compressed down to periodicity of order of wavelength.

Line integrated electron density profile of pulsed plasma is measured using two beam interferometric setup, illuminated by randomly polarized He-Ne laser. For this a spark gap was inserted in one arm of a Michelson interferometer. A high voltage pulse (~10kv) was applied across the spark gap to produce the air breakdown. In presence of plasma due to air breakdown in the spark gap the interference pattern undergoes modification. The modified interferogram was recorded. From the recorded interferogram, space resolved refractive index and hence line integrated electron density profile of a pulsed air breakdown was measured to be 10^{17} cm^{-3}.

Some of the possible applications of the interferometric arrays developed in the present thesis for photonic band gap materials, periodic microstructures and atom lithography are also proposed.

References

1. N. Streibl and M.E.Prise, “Digital Optics Architecture and Systems requirements,” Phys. Stat. solidi (b), **150**, 447-454(1988).

2. B.Hill, J.-P. Krumme, G.Much, R.Pepperl, J. Schmidt, K.P. Schmidt, K. Witter, and H. Heitmann, “Polycube optical memory: a $6.5X10^7$ bit read-write and random access optical store,” Applied Optics, **14**(11), 2607- 2612(1975).

3. Don A.Gregory and H.K.Liu, “Large memory real-time multichannel multiplexed pattern recognition,” Applied Optics **23**(24), 4560-4570(1986).

4. A.C. Walker, “Application of bistable optical logic gate arrays to all-optical digital parallel processing,” Applied Optics **25**(10), 1578-1585(1986).

5. Karl-Heinz Brenner, Alan Huang, and N. Streibl, “Digital optical computing with symbolic substitution,” Applied Optics **25**(18), 3054-3060(1986).

6. Karl-Heinz Brenner, “Programmable optical processor based on symbolic substitution”, Applied Optics **27**(9), 1687-1691(1988).

7. Toyohiko Yatagai, “Cellular logic architectures for optical computers,” Applied Optics **25**(10), 1571-1577(1986).

8. Jean Taboury, J.M. Wang, Pierre Chavel, F. Devos, And Patrick Garda, “Optical cellular processor architecture. 1: Principles,” Applied Optics **27**(9), 1643-1650(1988).

9. Toyohiko Yatagai, “Optical space-variant logic-gate array based on spatial encoding technique,” Optics Letters **11**(4), 260-262(1986).

10. Miles J. Murdocca, Alan Huang, Jurgen Jahns, and Norbert Streibl, “Optical design of programmable logic arrays,” Applied Optics **27**(9), 1651-1660(1988).

11. O. Guyot and H. Hamam, “Logic operations based on the fractional Talbot effect,” Optics Communications **127**, 96-106 (1996).

12. K.S.Urquhart, Philippe Marchand, Yeshaiahu Fainman, and Sing H. Lee, “Diffractive optics applied to free-space optical interconnects,” Applied Optics **33**(17), 3670-3682(1994).

13. D. Huang, J.F. Snowdon and A. J. Waddie, “Free space optical technology and neural network applications,” paper presented at Appl. Opt. Div. conf., reading, 16-19 September 1996.

14. T.D. Liao and Stephen Sheard, “Integrated-optic array illuminator: a new design for guided-wave optical interconnections.” Applied optics, **37(**13), 2729-2734(1998).

15. R. L. Morrison, S. L. Walker and T. J. Cloonan, “Beam array generation and holographic interconnections in a free-space optical switching network,” Applied optics, **32**(14), 2512-2518(1993).

16. F. B. Mcormick et al., “Five stage free-space optical switching network with field-effect transistor self-electro-optic-device smart-pixel arrays,” Applied Optics **33**(8), 1601-1618(1994).

17. C.P. Barrett et al., “Components for the implementation of free-space optical crossbars,” Applied Optics **35**(35), 6934-6944(1996).

18. L. Liu, X. Liu, and B. Cui, “Optical programmable cellular logic array for image processing,” Applied optics, **30**(8), 943-949(1991).

19. Francis T. S. Yu and Suganda Jutamulia, “Optical Signal Processing, Computing and Neural Network”, John Wiley and Sons, 1992.

20. M. Agu, A. Akiba and S. Kamemaru, “A Parallel–Processing Optical-Digital Recognition System as a Model of Biological Visual Perception,” Opt. Comm., **66**(2,3), 69-78(1988).

21. David B. Mortimore and J. W. Arkwright, “Monolithic wavelength-flattend 1X7 single-mode fused fiber couplers: theory, fabrication, and analysis,” Applied Optics **30**(6), 650-659(1991).

22. Nicholas Madamopoulos and Nabeel A. Riza, “Demonstration of an all-digital 7-bit 33-channel photonic delay line for phased array radars,” Applied Optics, **39(**23), 4168-4181(2000).

23. J. Yang, M.R. Wang, “Uniformizing field distribution along optical axis for volume holographic data storage,” Optics Communications **192**, 19-26(2001).

24. V. Sandoghdar, U. Drodofsky, Th. Schulze, B. Brezger, M. Drewsen, T.Pfau and J. Mlynek, “Lithography using nano lens arrays made of light,” J. of Modern Optics **44**(10), 1883-1898(1997).

25. J.E. Bjorkholm, R.R. Freeman, A. Ashkin, and D.B. Pearson, “Observation of focusing of neutral atoms by the dipole forces of resonance-radiation pressure,” Phy. Rev. Lett., **41**(20), 1361-1364(1978).

26. I.B. Diviliansky et al., “Fabrication of two-dimensional photonic crystals using interference lithography and electrodeposition of CdSe,” Appl. Phy. Lett. **79**(21), 3392-3394(2001).

27. C.Siegel, F. Loewenthal, J.E.Balmer, and H. P. Weber, “Talbot array illuminator for single-shot measurements of laser-induced-damage thresholds of thin film coatings,” Applied Optics, **39(**10), 1493-1499(2000).

28. Chandra Shakher and A.J.Pramila Daniel, “Talbot interferometer with circular gratings for the measurements of temperature in axisymmetric gaseous flames,” Applied Optics, **33**(25), 6068-6072(1994).

29. N. Streibl, U. Nolsher, J. Jahns and S. Walker, “Array generation with lenslet arrays” Applied Optics, **30**(19), 2739-2742(1991).

30. A.W.Lohmann and F. Sauer, “Holographic telescope arrays,” Applied Optics **27**(14), 3003-3007(1988).

31. O. Bryngdahl, “Image formation using self-imaging techniques,” JOSA **63**(4), 416-419(1973).

32. A.W.Lohmann, J. Schwider, N. Streibl, and J. Thomas, “Array illuminator based on phase contrast” Applied Optics **27**(14), 2915-2921(1988).

33. Peng Xi, C. Zhou, S. Zhao, Liren Liu, “Phase-contrast hexagonal array illumination,” Optics Communications **192**, 193-197(2001).

34. N. F. Borrelli, D. L. Morse, R.H. Bellmann, and W. L. Morgan, “Photolytic technique for producing microlenses in photosensitive glass,” Applied Optics **24**(16), 2520-2525(1985).

35. Z. D. Popovic, R.A. Sprague, and G.A. Neville Connel, “Technique for monolithic fabrication of microlens arrays,” Applied Optics **27**(7), 1281-1284(1988).

36. J. Jahns and S. Walker, “Two-dimensional array of diffractive microlenses fabricated by thim film deposition,” Applied Optics **29**(7), 931-936(1990).

37. A. Kolodziejczyk, “Lensless multiple image formation by using a sampling filter,” Optics Communications, **59**(2), 97-102(1986).

38. A.W.Lohmann “An array illuminator based on Talbot effect,” Optik, **79**(1), 41-45 (1988).

39. O. Bryngdahl, “Optical map transformation,” Optics Communications, **10**(2), 164-168(1974).

40. O. Bryngdahl, “Geometrical transformations in optics,” JOSA **64**(8), 1092-1099(1974).

41. W. J. Hossack, P. McOwan and R. E. Burge, “Computer generated optical fan-out element,” Optics Communications, **68**(2), 97-102(1988).

42. W.H.F. Talbot, “Facts Relating to Optical Sciences, No IV,” Philos. Mag. **9**, 401-407(1836).

43. A.W.Lohmann and J.A. Thomas, “Making an array illuminator based on Talbot effect, Applied Optics **29**(29) 4337-4340(1990).

44. Xiao-Yi Da, “Talbot effect and array illuminators that are based on it,” Applied Optics **31**(16), 2983-2986 (1992).

45. J.R.Leger and G.J.Swanson, “Efficient array illuminator using binary-optics phase plates at fractional-Talbot planes,” Optics Letters **15**(5), 288-290(1990).

46. Victor Arrizon and J. Ojeda-Castaneda, “Talbot array illuminators with binary phase gratings,” Optics Letters **18**(1), 1-3(1993).

47. Victor Arrizon and E. Lopez-Olazagasti, “Binary phase gratings for array generators at 1/16 of Talbot length,” JOSA comm. **12**(4) 801-804(1995).

48. C. Zhou, L.Liu, “Zernike array illuminator,” Optik **102**(2), 75-78(1996).

49. Changhe Zhou, L. Wang, T. Tschudi, “Solutions and analyses of fractional Talbot array illuminators,” opt. comm. **147**, 224-228(1998).

50. Piotr Szwaykowski and Victor Arrizon, “Talbot array illuminator with multilevel phase gratings,” Applied Optics **32**(7), 1109-1114(1993).

51. Victor Arrizon and J. Ojeda-castaneda, “Multilevel phase gratings for array illuminators,” Applied Optics **33**(25), 5925-5931(1994).

52. H. Hamam, “Design of Talbot array illuminators,” Optics Communications **131**,359-370 (1996).

53. H. Hamam, “Talbot array illuminators: general approach,” Applied Optics **36**(11), 2319-2327(1997).

54. H. Hamam, “Design of array illuminators operating under spherical illumination,” Applied Optics **37**(8), 1393-1399(1998).

55. Phillip A. Newman, Vincent E. Rible, “Pinhole array camera for integrated circuits,” Applied Optics, **5** (7), 1225 (1966)

56. R.G. Olsson, “Generation of micro circuit pattern arrays by diffraction imaging,” presented at the conference on the use of optics in microelectronics, OSA, January 1971, Las Vegas, Nevada

57. G. Groh, “Multiple imaging by means of holograms of correlated objects,” Applied Optics, **8** (5), 967 (1969).

58. H. J. Gerritsen, W. J. Hannan, E. G. Ramberg, “Elimination of speckle noise in holograms with redundancy,” Applied Optics, Vol. 7 Issue 11 Page 2301 (November 1968).

59. Robert A. Bartolini, W. Hannan, D. Karlsons, M. Lurie, “Embossed hologram motion pictures for television playback,” Applied Optics, Vol. 9 Issue 10 Page 2283 (October 1970).

60. G. Groh, “Optical multiplex system for pattern recognition utilizing point holograms,” Optics Communications **1**(9) 454-456(1970)

61. L.P.Bolivin, “Multiple imaging using various types of simple phase gratings,” Applied Optics **11**(8), 1782-1792(1972).

62. A. Kalestynski, “Multiplying lensless Fourier holograms recorded using a multibeam reference light field,” Applied Optics **15**(4) 853-855(1976).

63. B.J. Thompson, “Multiple imaging by diffraction technique,” Applied Optics **15**(2) 312(1976).

64. A. Kalestynski and B. Smolinska, “Spatial frequency sampling by phase modulation as a method of generating multiple images,” Applied Optics **16**(8) 2261-2263(1977).

65. A. Kalestynski, “Enhancement of multiple images by sampling spatial filtering using additional auxiliary sampling,” JOSA **65**(12), 1443-1447(1975).

66. P. Matthijsse, “Multiple imaging with thin phase filters: A signal processing approach,” JOSA **68**(6), 733-739(1978).

67. Wai-Hon Lee, “High efficiency multiple beam gratings,” Applied Optics **18**(13), 2152-2158(1979).

68. H. Dammann and K. Gortler, “High efficiency in-line multiple imaging by means of multiple phase holograms,” Optics Communications **3**(5), 312-315(1971).

69. H. Dammann and E. Klotz, “Coherent optical generation and inspection of two-dimensional periodic structure,” Optica Acta **24(4)**, 505-515(1977).

70. U. Killat, G.Rabe, and W.Rave, “Binary phase grating for star couples with a high splitting ratio,” Fiber Integrat. Opt. 4, 159-167(1982).

71. U. Krackhardt and N. Streibl, “Design of Dammann-Gratings for array generation,” Optics Communications, **74**(1,2), 31-36(1989).

72. J. N. Mait, “Design of Dammann Gratings for two dimensional, non-seperable, noncentrosymmetric responses, Optics Letters **14**(4), 196-198(1989).

73. J. Turunen, A. Vasara, J. Westerholm and Arto Salin, “Stripe geometry two dimensional Dammann gratings,” Optics Communications, **74**(3,4), 245-252(1989).

74. J. N. Mait, “Design of binary-phase and multiphase Fourier gratings for array generation,” JOSA A **7**(8), 1514-1528(1990).

75. Rick L. Morisson, “Symmetries that simplify the design of spot array phase gratings,” JOSA A **9**(3), 464-471(1992).

76. P. Senthilkumaran, K.V. Sriram, M.P. Kothiyal and R.S. Sirohi, “Array generation using double wedge plate interferometer,” J of Modern Optics, **41**(3), 481-484(1994).

77. P. Senthilkumaran and R.S. Sirohi, “Michelson interferometer in tandem for array generation,” Optics Communications, **105**(3,4), 158-160(1989).

78. Shanti Bhattacharya, P. Senthilkumaran, J.S. Darlin, M.P. Kothiyal and R.S. Sirohi, “Holographic array illuminator using tandem Michelson interferometers: fabrication and analysis,” J of Modern Optics **42** (11), 2275-2283 (1995).

79. J.S. Darlin, P. Senthilkumaran, S. Bhattacharya, M.P. Kothiyal and R.S. Sirohi, “Fabrication of an array illuminator using tandem Michelson interferometers,” Optics Communications **123**(1-3)1-4 (1996).

80. P. Senthilkumaran, “An interferometric array generator with polarizing elements,” Optics and laser engineering, **28**, 457-461(1997).

81. J. Primot, “Three-wave lateral shearing interferometer,” Applied Optics 32(31), 6242-6249(1993).

82. J. Primot, L. Songo, B.Fracasso and K. Heggarty, “Wavefront sensor protype for industrial applications based on a three-level phase grating,” Optical engineering, **36**(3), 901-904(1997).

83. Jan Masajada and Boguslawa Dubik, “Optical ortex generation by three plane wave interference,” Optics Communications, **198**, 21-27(2001).

84. J. Canning and M.Aslund, “Holographic construction of 2-D arrays of UV intensity using additive source interference from multiple slab reflections,” Optics Communications, **202**, 271-275(2002).

85. L.Z.Cai, X.L. Yang and Y.R.Wang, “Formation of a microfiber bundle by interference of three noncoplanar beams,” Optics Letters **26**(23), 1858-1860(2001).

86. X.L. Yang and L.Z.Cai, “Wave design of the interference of three noncoplanar beams for the microfiber fabrication,” Optics Communications, **208**, 293-297(2002).

87. H. Machida, J. Nitta, Atsuya Seko, and H. Kobayashi, “High-efficiency fiber grating for producing multiple beams of uniform intensity,” Applied Optics, **23**(2), 330-332(1984).

88. T. Kubota and M. Takeda, “Array illuminator using grating couplers” Optics Letters **14**(12), 651-652(1989).

89. S. Nemoto and Jun Kida, “Retroreflector using gradient-index rods,” Applied Optics, **30**(7), 815-822(1991).

90. Max Born and Emil Wolf, *Principles of Optics*, Pergamon press, sixth Ed.

91. Davis S. Kliger, J.W.Lewis and C.E. Randall, *Polarized Light in Optics and Spectroscopy*, Academic Press Inc.

92. Malacaara D. Optical Shop Testing, New York: John Wiley and Sons, 1992.

93. Hariharan P., Roy M., “Achromatic phase-shifting for two-wavelength phase-stepping interferometry,” Optics communications, **126**, 220-222 (1996).

94. Asundi A., Liu T., and Boay C. G., “Phase-shifting method with a normal polariscope,” Applied Optics, **38** (28), 5931-5935 (1999).

95. Kothiyal M.P. and Delisle C., “Polarization Component phase shifters in phase shifting interferometry: error analysis,” Optica Acta, **33** (6), 787-793(1986).

96. Chyba T.H., Wang L.J., Mandel L., and Simon R., “Measurement of the Pancharatnam phase for a light beam,” Optics Letters, **13** (7), 562-564 (1998).

97. Frins E. M. and Dultz W., “Polarization-based tunable interferometric filter,” Applied Optics, **37**(22), 5234-5238 (1998).

98. Teng H., Chou C., Chang H., “Polarization-shifting interferometry on two-dimensional linear birefringent parameters measurement,” Opt. Comm., **224**, 197-204 (2003).

99. Cai L.Z. and Yang X.L., “Interference of circularly polarized light: contrast and application in fabrication of three dimensional periodic microstructures,” Optics and Laser Tech., **34**, 671-674(2002).

100. Cai L.Z., Yang X.L. and Liu Q., “General representation of interference contrast formed by arbitrarily polarized waves and its application in wave design for holographic fabrication of photonic crystals,” Optics and Laser Tech.. **36**, 453-457(2004).

101. A. S. Patra and Alika khare, “Interferometric Array Illuminator Using Polarized Beams,” Proceedings of Photonics 2004, Kochi, India.

102. P. Ehbets, H.P Herzig and D.Prongue and M.T.Gale, “High efficiency continuous surface-relief gratings for two dimensional array generation” Optics Letters, **17**(13), 908-910(1992).

103. M. Gale , M. Rossi, J. Pedersen, H. Schutzh, “Fabrication of continuous-relief micro-optical elements by direct laser writing in photoresists,” Optical Engineering, **33**(11) 3556-3566(1994).

104. Rai-Choudhury, P. "*Handbook of Microlithography, and Microfabrication”*, Spie Optical Engineering Press, 1994.

105. M. Ekberg, M. Larsson, S. Hard, J. Turunen, M. R. Taghizadeh, J. Westerholm and A. Vasara, “Multilevel grating array illuminators manufactured by electron beam lithography,” Optics Communications, **88**, 37-41(1992).

106. Qu. Y. et al., “940nm low beam divergence tapered window laser arrays,” Optics and Laser Technology, **34**, 675-677 (2002).

107. M. Korn et. al., “First order distributed feedback grating (92.5–10.5 nm period) for GaInP/AlGaInP lasers emitting in the visible range,” J. Vac. Sci. Tech., **B8**, 1404-1407 (1990).

108. Krauss et. al., “Photonics microstructures as laser mirrors,” Optical Engineering, **37** (4), 1143 -1148 (1998).

109. C. Cohen-tannoudji, J. Dupont-Roc, G. Grynberg, *Atom-Photon Interaction*, Wiley, New York, (1992).

110. J. Dalibard, J.M. Raimond, J. Zinn-Justin, *Fundamental systems in Quantum Optics*. North Holland, Amsterdam (1992).

111. R. Gupta, J.J. McCelland, Z.J. Jabbour and R.J. Celotta, "Nanofabrication of two dimensional array using focused atomic deposition," Appl. Phys. Lett., **67** (10), 1378 (1995).

112. B.Brezer, T. Schulze, P.O.Schmidt, R.Merteno, T.Pfau and J.Mlynek, "Polarization gradient light masks in atom lithography," Europhysics Letters, **46** (2), 148 (1999).

113. M.P. MacDonald, L.Paterson, W.Sibbett, K.Dholakia and P.E.Bryant, "Trapping and manipulation of low-index particles in a two-dimensional interferometric optical trap," Optics Letters **26,** 863-865 (2001).

114. M.Campbell, D.N.Sharp, M.T.Harrison, R.G.Denning and A.J.Turberfield, "Fabricationof Photonic crystals for the visible spectrum by holographic lithography," Nature **404,** 53 (2000).

115. Rambo P., Schwarz J., Diels J-C., "Interferometry with two-dimensional spatial and high temporal resolution," *Optics Communications*, **197**, 145-149 (2001).

116. Yuri P.Raizer, *Gas Discharge Physics*. Moscow: Springer-Verlag, 1987, ch. 6, 7 and 8.

List of publications

Paper in journals:

1. **A.S.Patra** and Alika Khare, "Interferometric Array Generation," J. of Optics and Laser Technology, **38**, 37-45 (2006).
2. **A.S.Patra** and Alika Khare, "Generation and fringe visibility studies of non-observable array illuminator using polarized beams" J. of Optics A: Pure and Applied Optics, **7**, 535-539 (2005).
3. **A.S.Patra**, Tina Dhekial Phukan and Alika Khare, "Measurement of Two Dimensional Electron Density Profile in a Low Current Spark Using Interferometry," IEEE Transactions on Plasma science, **33** (5), 1725-1728 (2005).
4. **A.S.Patra** and Alika Khare, "Study of two beam heterodyne interferometry," Journal of Optical Technology, **72** (12), 25-28 (2005).
5. Alika Khare, Kamlesh Alti, Susanta Das, **Ardhendu Sekhar Patra** and Monisha Sharma, "Application of laser matter interaction for generation of small sized materials," J. of Radiation Physics and Chemistry, **70**, 553-558, (2004).
6. Kamlesh Alti, **A.S.Patra** and Alika Khare, "Two dimensional periodic potentials via multiple beam interferometry for atom lithography," J. of Microlithography, Microfabrication, and Microsystems, **5**(2) (April, 2006, In Press).
7. **A.S.Patra** and Alika Khare, "Classroom experiment on realization of phase shift via polarizer in a two-beam polarized interferometer," Euro. J. of Physics (Submitted)
8. **A.S.Patra** and Alika Khare, "Generation and fringe visibility studies of array illuminator using randomly polarized and polarized beams" (under preparation).

Paper published in international/national conference:

1. **A.S.Patra** and Alika Khare, “Phase shift via polarizer in a heterodyne interferometer”, ETOP 2005, Marseille, France.
2. Gautam Sarma, Kamlesh Alti, **Ardhendu Sekhar Patra**, Sidananda Sarma and Alika Khare, “Synthesis of Cu2O nano particles via laser liquid interaction” Proc. ICOL -2005.
3. Kamlesh Alti, **Ardhendu Sekhar Patra** and Alika Khare, “A novel technique of direct patterning via high power laser interferometry” Proc. ICOL -2005.
4. **A.S.Patra** and Alika Khare, “Fringe contrast of array illuminator as a function of relative state of polarization of the interfering beams,” Proc. of National Conference on Laser and their applications in Basic and Applied Sciences (NCLBAS), Visva-Bharati, Santiniketan, 2005.
5. **A.S.Patra** and Alika Khare, “Fringe visibility of interferogram from two orthogonal elliptically polarized light,” Proc. of National Laser Symposium-04 BARC, Mumbai, 2004.
6. **A.S.Patra** and Alika Khare, “Interferometric array illuminator using polarized beams,” Proc. of Photonics 2004, Kochi, India.
7. Kamlesh Alti, **A.S.Patra** and Alika Khare, “Simulated lithographic patterns from a single atomic beam in two dimensional periodic potential generated via interference of four optical beams,” Proc. of Photonics 2004, Kochi, India.
8. **A.S.Patra** and Alika Khare, “Two-Dimensional Spatial and Temporal Plasma Density Profile,” Proc. of DAE-BRNS Workshop on Plasma Surface Engineering, BARC, Mumbai, 2004.

9. **A.S.Patra** and Alika Khare, “Delocalized Hexagonal Arrays using Multiple Beam Interferometry,” Proceedings of International conference on laser application and optical metrology, Page no-389, 2003.
10. **A.S.Patra**, Tina Dhekial Phukan and Alika Khare, “Measurement of Two Dimensional Electron Density Profile in a Low Current Spark Using Interferometry”, Proceedings of International conference on laser application and optical metrology, Page no-392, 2003.
11. Susanta Das, Monisha Sharma, **Ardhendu Shekhar Patra** and Alika Khare, “Selective ablation of thin films using nanosecond laser”, Proceedings of International conference on laser application and optical metrology, Page no-370, 2003.
12. **A.S.Patra**, P. Senthilkumaran and Alika Khare “Phase shifting through polarization components”, Proceedings of DAE-BRNS National Laser Symposium, Dec 2003.
13. **A.S.Patra** and Alika Khare “Optical Array Generator Using Interferometry”, Proceedings of DAE-BRNS National Laser Symposium, Page no- 239, 2001.